McMASTER UNIVERSITY

HAMILTON, ONTARIO, CANADA

DEPARTMENT OF METALLURGY

AND MATERIALS SCIENCE

METALLURGICAL ASPECTS OF MACHINABILITY IN MEDIUM CARBON STEELS

FINAL REPORT

April 1, 1985 - March 31, 1987

D.A.R. Kay (Principal Investigator)
S.V. Subramanian
R. Sowerby
N. Chandrasekaran

Work in this project was conducted under the auspices of
Physical Metallurgy Research Laboratories
Canada Centre for Mineral and Energy Technology
Energy, Mines and Resources, Canada

DSS FILE NUMBER	:	20ST-23440-5-9055
DSS CONTRACT SERIAL NUMBER	:	OST85-00201
CANMET PROJECT NUMBER	:	430761
CANMET SCIENTIFIC AUTHORITY	:	Dr. J.D. Boyd

October 1987
This report should be cited by D.S.S.
File No. 20ST-23440-5-9055

MICROMEDIA

DARK-47a

CONTENTS

		Page
Executive Summary		i-iii
Résumé Exécutif		iv-vi
Section 1.	Design of Clean Steel for High Strain Rate Machining (S.V. Subramanian)	
1.1	Introduction	1
1.2	Damage Accumulation and Chip Formation	3
1.2.1	Macroscopic Flow Analysis	4
1.2.2	Damage Observation on Chips	4
1.3	The Influence of Cutting Speed on Damage Rates	6
1.4	High Strain Rate Deformation Behaviour of Metals	7
1.5	Steel Design for High Strain Rate Machining	8
1.6	Fracture Criterion Based on Material Property	8
1.7	Design Criteria for Steels for High Strain Rate Machining	9
1.8	Design of Microalloyed Steel with Improved Machinability	10
Section 2.	Chip Formation Mechanics and Development of Continuum Models for Analyzing the Machining Operation (R. Sowerby, N. Chandrasekaran and S.V. Subramanian)	
2.1	Mechanism of Chip Formation	11
2.1.1	Cutting Tests Using Plasticine as Model Material	11
2.1.2	Discontinuous Chip Model Based on a Single Shear Plane	12
2.2	Cutting Tests on Steels	13
2.2.1	Quick-Stop Experiments on Spheroidized Steels	13
2.2.2	Machining Tests on AISI 4340 Steel	15
2.3	Development of Continuum Models for Analysing Machining Operations	16
2.3.1	The Slip Line Field Proposed by Roth and Oxley [4]	17
2.3.2	A Proposed Slip Line Field	19
2.3.3	Damage Accumulation Based on Hole Growth	21
2.4	Estimating Critical Accumulated Damage	22
2.4.1	Computation of Critical Accumulated Damage Employing a Collar Test	23

CONTENTS (continued)

Section 3. Tool Wear in Metal Cutting
(N. Chandrasekaran and R. Sowerby)

3.1 Introduction 25

3.2 Wear Mechanisms 25
3.2.1 Tool Wear by Solution 27
3.2.2 Wear due to Adhesion 27
3.2.3 Deformation Dominated Delamination Wear 28
3.2.4 Wear due to Abrasion 28
3.2.5 Oxidation and Melt Wear 28

3.3 Plane-Strain Elastic Finite Element (F.E.) Analysis 29

3.4 Cutting Tool Grades 30

3.5 Wear Mechanism Models 31
3.5.1 Flank Wear 32
3.5.2 Rake Face Wear (Cratering) 32
3.5.3 Grooving Wear 32

3.6 Wear Mechanism Maps 33

Section 4. Inclusions and Tool Wear
(D.A.R. Kay and Junpu Jiang)

4.1 Introduction 34

4.2 The $CaO-Al_2O_3$ System 35

4.3 The $MnO-SiO_2-Al_2O_3$ and $CaO-SiO_2-Al_2O_3$ Systems 37

Section 5. Discussion and Conclusions 39

Acknowledgements 41

References 42

Tables 45

Figures 50

Appendix I

Appendix II

Appendix III

EXECUTIVE SUMMARY

This Final Report describes the research being carried out at McMaster University by Drs. Sowerby and Chandrasekaran in the Department of Mechanical Engineering, and Drs. Subramanian and Kay in the Department of Materials Science and Engineering. This work is focussed on the chip formation and tool wear aspects of the machining process and is aimed at the development of current and future machining technologies in Canada.

Detailed SEM studies of chips and quick-stop samples have been undertaken by Dr. Subramanian in order to map the damage associated with the type, size, volume fraction and local dispersion of second phase particles. The basic concept here is that the critical accumulated damage to fracture is a material property, which is related to microstructural parameters. Factors which decrease the critical accumulated damage to fracture, such as a high volume fraction of second phase particles, large particle size and decreased interparticle spacing, will facilitate the chip fracture process. Free machining additives are used to decrease the accumulated damage to fracture in steels machined at low and moderate cutting speeds ($V < 100$ m/min).

Phenomenological observations of chips generated at high cutting velocities ($V > 200$ m/min) show extensive void growth in comparison with chips generated at low cutting velocities. These increased damage rates are attributed to the increase in the material flow stress brought about by the high strain rates. In a material with a characteristic critical accumulated damage to fracture, an increase in the rate of accumulation of damage will facilitate the chip fracture process. The increase in flow stress in high strain rate machining ($\varepsilon > 10^3 - 10^4$/s) results in an increased rate of damage accumulation and strain localization. Under these circumstances, the use of free machining additives, which decreases the critical accumulated damage to fracture at low/moderate cutting speeds, resulting in good chip formation, may no longer be necessary. Dr. Subramanian has proposed the concept of clean steel design for high strain rate machining whereby good chip formation may be achieved in a calcium deoxidized clean steel, strengthened by microalloying. High

strain rate machining imposes high normal stress at the tool tip and modern ceramic tools are capable of performing well even under this stringent condition.

The mechanics of the machining operation have been analyzed by Drs. Sowerby and Chandrasekaran using slip line field models. This work has extended the slip line field solutions, developed for a strain hardening material by Oxley and his co-workers over the last two decades, taking into account temperature and strain rate effects. These models have enabled the stress distribution, expressed in terms of the ratio of the local hydrostatic pressure to the local flow stress of the material, the p/k ratio, to be determined through the deformation zone. A hole growth model developed by the authors allows the damage accumulation to be evaluated for a volume element as it moves along the typical stream line. Under conditions where $p/k < 1$, one of the principal stresses is tensile, which contributes to a positive damage rate. Microcracking will occur if the damage accumulated exceeds a critical value, characteristic of a given material. One of the results of fundamental importance is that the p/k ratio decreases with increasing cutting speed resulting in increased damage rate thus providing the rationale behind the choice of steels for high productivity machining.

The ductility of AISI 4340 steel was varied by heat treatment. The critical accumulated damage is shown to decrease with the ductility of the steel. From machining tests, it was established that discontinuous chips could be promoted in the steels with low critical accumulated damage at low cutting velocities.

Drs. Chandrasekaran and Sowerby have also reviewed the literature on tool wear in metal cutting in order to provide the basis for future research on tool wear processes.

Dr. Kay and Mr. Junpu Jiang have completed thermodynamic models which relate the compositions of inclusions in the $CaO\text{-}Al_2O_3$, $MnO\text{-}SiO_2\text{-}Al_2O_3$ and $CaO\text{-}SiO_2\text{-}Al_2O_3$ systems with the corresponding steel composition, as a function of soluble oxygen content at a given temperature. Preliminary comparison of the predictions of these models with the results of industrial steelmaking practice using measured soluble oxygen contents and temperatures indicate that they can be used to facilitate the 'inclusion engineering' required

in the production of steels of improved machinability.

RÉSUMÉ EXÉCUTIF

Ce rapport final décrit la recherche menée a l'Université McMaster par Dr. Sowerby et Dr. Chandrasekaran du département de Génie mécanique, et Dr. Subramanian et Dr. Kay du Département de Génie et Science des Matériaux. Cette recherche concerne principalement les aspects 'génération d'éclats' et 'usure des outiles' de l'opération d'usinage, et se veut contribuer au dévelopement des technologies d'usinage actualles et futures du Canada.

Dr. Subramanian a étudié en détail des éclats et des éprouvettes (brusquement ôtées de la machine, en cours d'usinage) à l'aide du Microscope Electronique à Balayage afin de corrèler le dommage au type, à la taille, à la fraction volumique, et à la dispersion locale des particules de seconde phase. L'idée sous-jacente, ici, est de considérer le dommage de fracture accumulé comme une propriété du matériau, liée aux paramètres microstructuraux. Les fracteurs qui diminuent le dommage de fracture accumulé critique, tels qu'une fraction voluminique de particules de seconde phase élevée, une grande taille des particule et une petite distance entre les particules, facilitent le processus de brisure des éclats. Des composants facilitant l'usinage sont inclus pour dimineur le dommage de fracture accumulé dans des aciers usingés sous vitesse de coupe lente ou moderée ($v < 100$ m/min).

Des observations phénoménologiques ont permis de démontrer une relativement forte croissance de vides au sein d'éclats générés sous vitesse de coupe rapide ($v > 200$ m/min), en comparison avec les éclats générés sous vitesse de coupe lente. Ces taux d'endommagement accrus sont attribués à l'augmentation de la contrainte de fluage du materiau, causés par les taux élevés de deformation. Dans un matériau ayant un dommage de fracture accumulé critique déterminé, une augmentation du taux d'accumulation du dommage facilite le processus de brisure des éclats. L'augmentation de la contrainte du fluage au cours d'usinages à taux élevé de déformation ($\Sigma > 10^3 - 10^4$/s) produit une augmentation du taux d'accumulation du dommage et de déformation localisée. Dans ces conditions, l'utilisation de composants acilitant l'usinage qui permet de diminuer le dommage de fracture accumulé critique et d'améliorer la génération d'éclats sous vitesse de coupe lente/modérée n'est plus necessaire.

Dr. Subramanian a proposé l'idée d'une conception d'aciers n'incluant pas ces composants pour l'usinage à taux élevé de déformation selon laquelle une bonne génération d'éclats pourrait être obtenue dans un tel acier, désoxidé en calcium, renforcé par microalliage. L'usinage à taux élevé de déformation crée une forte contrainte normale à l'extrémité de l'outil et les outiles en céramique moderne sont capables d'usiner de facon satisfaisante, même dans ces conditions rigoureuses.

L'aspect mécanique de l'opération d'usinage est analysé par Dr. Sowerby et Dr. Chandrasekaran au moyen d'un modèle de champs de lignes de glissement. Leur travail a permis d'accroitre les solutions du champ de lignes de glissement dévelopées par Oxley et ses associés au cours des deux dernières décennies pour le cas d'un matériau dont la contrainte de fracture croit en cours de déformation, en considérant les effets de la température et des taux de déformation. Ces modèles ont permis de déterminer la distribution des contraintes dans la zone de déformation, exprimée en fonction du rapport de la pression hydrostatique locale à la contrainte de fluage locale du materiau, p/k. Une modélisation de la croissance des trous, dévelopée par les auteurs, permet d'évaluer la variation du dommage accumulé par un élément de volume dont la position varie le long d'une ligne de fluage type. Si $p/k < 1$, l'une des contraintes principales agit en tension, ce qui contribue a causer un taux d'endommagement positif. Au delà d'une valeur critique de dommage accumulé caractéristique d'un matériau donné, de la microfracture commence à se developper. L'un des résultats d'une importance capitale est le fait que le rapport p/k décroit avec l'augmentation de la vitesse de coupe, causant une augmentation du taux d'endommagement, offrant ainsi un critère rationel de choix des aciers destinés à un usinage à forte productivité.

Des aciers AISI 4340 de ductilité variée furent obtenus par traitement thermique. Le dommage accumulé critique décroit en même temps que la ductilité de l'acier. A partir de tests d'usinage, nous avons démontré que des éclats discontinus pouvaient être générés dans les aciers dont le dommage accumulé critique est peu élevé, sous vitesse de coupe lente.

Dr. Chandrasekaran et Dr. Sowerby ont aussi analysé et résumé l'état actuel de la recherche sur l'usure des outiles et la coupe des métaux afin de fournir une référence à la recherche à venir sur les processus d'usure.

Dr. Kay et Mr. Junpu Jiang ont créé des modèles thermodynamiques qui permettent de corréler la composition des inclusions dans les systmèmes $CaO-Al_2O_3$, $MnO-SiO_2-Al_2O_3$ et $CaO-SiO_2-Al_2O_3$ avec la composition des aciers correspondants. Des comparaisons préliminaires entre les prédictions de ces modèles et le résultat de la pratique de l'industrie sidérurgique en utilisant les compositions en oxygène soluble et les températures indiquent que ces modèles peuvent être utilisés afin de faciliter le "contrôle des inclusions" nécessaire pour produire des aciers plus faciles à usiner.

SECTION 1

DESIGN OF CLEAN STEEL FOR HIGH STRAIN RATE MACHINING

S.V. Subramanian

1.1 Introduction

Tool wear and chip formation are two distinct aspects that have to be considered in the metallurgical design of steels of improved machinability. Abrasion of the tool by second phase particles in the workpiece that are 'harder' than the tool contributes significantly to tool flank wear. Alumina inclusions which result from conventional aluminum steel deoxidation practice are particularly harmful and their elimination or modification in steel processing is one of the features in the reduction of tool wear by abrasion. Standard deoxidation practices are modified by calcium treatment to give either 'soft' anorthitic ($CaO.2SiO_2.Al_2O_3$) or gehlenitic ($2CaO.Al_2O_3.SiO_2$) inclusions in the case of silicon/-manganese deoxidized steels and duplex calcium aluminate/calcium sulphide inclusions in the case of aluminum deoxidized steels [1,2]. In the latter case the abrasive alumina inclusions are modified to calcium aluminates on which 'soft' calcium sulphide can precipitate. However, solid deoxidation products in the molten steel are undesirable as their precipitation contributes to the nozzle clogging problem in continuous billet casting. In the absence of adequate residual aluminum for grain size control, it is necessary to combine microalloying additions such as Nb, Ti or V with calcium treatment.

Tool wear can also be decreased by increasing the hardness of the tool surface relative to the hard second phase particles in the workpiece. This is achieved by coating the tool surface with 'hard' coatings such as titanium carbide or titanium nitride, by using PVD (Physical Vapour Deposition) or CVD (Chemical Vapour Deposition) techniques. Significant progress has also been made in recent years in the development of sintered carbide and fibre reinforced ceramic tool inserts. This new development of tool materials has made it possible to attain higher rates of metal removal, with cutting speeds of up to 600 m/min.

Chips formed during the machining of low and medium carbon steels over a wide range of cutting speeds exhibit microstructural features characteristic of ductile fracture [1,2]. The primary role of free-machining additives in steel is the production of controlled dispersions of second phase particles which promote ductile fracture during machining and

facilitate the chip formation process through void nucleation, growth and coalescence. 'Soft' manganese sulphide inclusions have been traditionally used for this purpose. Recent developments in primary and secondary steelmaking processes such as powder injection, wire feeding and argon stirring technologies, coupled with uniform temperature control using ladle reheat furnaces, permit the consistent production of steels of improved cleanliness. Thus calcium-treated, microalloyed steels can be produced with a very low volume fraction of globular inclusions. Such steels will exhibit superior strength properties and enhanced through thickness ductility and toughness.

In order to facilitate the fracture process in chip formation at moderate cutting speeds, the traditional approach has been to introduce free cutting additives such as lead and sulphur. The role of the free cutting additives is to lower the critical accumulated damage to fracture. Thus, the free cutting additions will lower the strength and ductility of the steel. At moderate cutting speeds, the problem is to define the optimum quantity of free cutting addition for a given speed of cutting. However, with the higher speeds of cutting achievable with modern tools, damage rates are found to increase dramatically and under high velocity cutting conditions, it is necessary to re-examine the need for free cutting additives. One approach is to identify the conditions under which free cutting additions can be minimised, and where the strength and ductility properties and fatigue performance of the cleaner steel need not be unnecessarily compromised.

The concept of critical accumulated damage is used in this report to rationalize the fracture behaviour of low and medium carbon steels in metal cutting. Both phenomenological observation and theoretical analysis suggest that at the high strain rates characteristic of high cutting speeds, chip formation is facilitated by an increased damage rate and strain localization. It is concluded that at high strain rates, it may not be necessary to promote ductile fracture by decreasing the distance between the voids and inclusions through the use of free cutting additives. This suggests the possibility of strengthening the steel through

microalloying additions and improving the cleanliness of the steel through calcium deoxidation, while still achieving good chip formation in high strain rate machining[3].

1.2 Damage Accumulation and Chip Formation

A basic understanding of fracture processes associated with chip formation in metal cutting is essential in order to improve the machinability of a given grade of steel for a given rate of metal removal. The deformation process associated with chip formation is a heterogeneous one, involving high strain rates ($10^4 - 10^6$/sec) and large strains (>1) in a highly localized zone, a few microns thick in the workpiece, extending from the tool/workpiece interface. Figure 1 shows an SEM montage of a quick-stop section of a low carbon, resulphurized steel, at a cutting speed of 70 m/min. Void nucleation is associated with the fragmentation of cementite plates and there is also evidence of decohesion around MnS inclusions. Even at higher cutting speeds, ductile rupture regions are clearly seen. Figures 2(a) and 2(b) are SEM pictures of a chip obtained from a medium carbon (0.45 wt.%C) steel, at a cutting speed of 2000 m/min. The coalescence of voids into cracks has culminated in fracture processes leading to chip segmentation.

The various stages leading to total failure due to ductile fracture may be summarized as follows:

(i) As the material is progressively worked, second phase particles and interphase interfaces start acting as centres for the formation of voids. Void initiation occurs because of the inherent deformation incompatibilities which exist between the second phase particles and the surrounding matrix. In the case of oxides which are harder than the matrix, void nucleation starts by particle cracking, and in the case of sulphides which have a lower interfacial energy between the inclusion and the matrix, decohesion occurs at the inclusion/matrix interface, even at low strains.

(ii) Increasing plastic strain promotes void growth.

(iii) With continuing deformation, damage accumulates to a critical value at which microstructural instability occurs, resulting in void coalescence and microcrack formation.

Thus the fracture process in chip formation is analysed in terms of damage accumulation to ductile fracture. The damage, in turn, can be assessed from the areal fraction of voids measured on SEM micrographs. The metal cutting conditions define the macroscopic strain distribution in the primary and secondary shear zones. The geometry of the metal cutting operation and the cutting velocity are the key variables of the metal cutting process. The microstructure, and in particular, the second phase particle dispersion, determines the strain localization and consequently the microscopic flow of the material. Thus, both macroscopic and microscopic flow influence the damage process.

1.2.1 Macroscopic Flow Analysis

A model based on a modified Slip Line Field [4] has been developed in the course of this study by Chandrasekaran and Sowerby [5], to predict the macroscopic stress distribution in the deformation zone for a given set of cutting conditions. The objective is to develop hydrostatic pressure and strain distribution maps for the deformation zone and use these to predict accumulated damage. The development of this work is given in Section 2 of this report.

1.2.2 Damage Observation on Chips

The microscopic criteria for chip fracture involving second phase particles have been studied using the phenomenological approach. Detailed SEM studies of chips and quickstop samples, generated at various cutting speeds, were undertaken for different steels with the objective of mapping the damage associated with the type, size, amount and local dispersion of second phase particles. The salient observation resulting from these SEM studies of chip fracture surfaces are summarized below.

(i) The intensity of damage, as evidenced by extended void growth, is pronounced in the interior region of the chip. There is negligible damage on the free surface of the chip as well

as in the immediate vicinity of the tool tip. However, the damage is most pronounced in the region where the primary shear zone meets with the secondary shear zone. There is also notable damage in the interior region of the secondary shear zone. Figure 3(a) is an SEM picture of a quick-stop sample of a partially spheroidized AISI 1045 grade steel, interrupted during machining at a cutting velocity of 60 m/min. Figure 3(b) shows the damage associated with the carbide particles in the primary shear zone at an interior location approximately one third of the distance from the tool tip to the free surface of the chip, as indicated in Figure 3(a).

(ii) There is strong evidence of severe bending and plastic deformation of the carbide plates in the primary shear zone in the immediate vicinity of the tool tip, and also in the region close to the free surface of the chip. This is indicative of a large hydrostatic (compressive) pressure. Figure 4 shows an SEM picture of the heavily deformed and bent carbides occurring in the vicinity of the free surface of the chip, at a region shown in Figure 3(a).

(iii) A map of damage intensity in a quick-stop sample of an AISI 1045 spheroidized steel, subjected to a moderate cutting velocity, shows that the chip is continuous and that the damage intensity decreases as the free surface of the chip is approached. Figure 5 is an SEM picture of a region at the free surface of the chip, which exhibits no significant damage features.

(iv) An AISI 1045 steel, subjected to a spheroidizing treatment, exhibits void nucleation associated with carbides rather than extended void growth, at moderate cutting velocities (<100 m/min).

(v) Conversely, at higher cutting velocities (>200 m/min), a medium carbon steel (0.45 wt.%C), with a microstructure consisting of carbides and MnS inclusions, exhibited pronounced growth of voids associated with the MnS inclusions and carbide particles, indicating that void growth dominates at higher cutting velocities.

At high cutting speeds, the tendency for segmentation increases with the cutting speed but the degree of segmentation is incomplete until a critical speed is exceeded. Figure 6

shows a typical fully segmented chip, obtained at 2000 m/min, from a medium carbon steel in the quenched and tempered condition with the following typical analysis:

Material	C	Si	Mn	P	S	Cr	Mo
42CrMoS4V	0.42	0.33	0.74	0.0012	0.029	1.04	0.18

A detailed examination of the SEM pictures of the fracture surface shown in Figure 7 shows two distinct regions. The ductile rupture region shows characteristic dimples. Inclusions and carbides in this region are associated with extensive void growth and linkage. The segmented fracture surface is smooth and undeformed. Thus, following the region of ductile rupture there appears to be a region of catastrophic crack propagation. Extensive void growth is the characteristic feature of chip fracture surfaces obtained at high cutting velocities (>200 m/min). Figures 8(a) and 8(b) show extensive damage or void growth associated with MnS inclusions in a chip from the same steel referred to in Figure 6, but generated at a lower cutting velocity of 200 m/min. The segmentation of the chip is incomplete in this case.

1.3. The Influence of Cutting Speed on Damage Rates

The chips generated at high cutting velocities (2000 m/ min) in 42CrMoS4V steels show extensive void growth in comparison with chips generated at low cutting speeds. There is no microstructural evidence of high temperature softening of the structure. The strain measurements carried out on second phase carbide particles yielded values comparable with those in chips generated at moderate and moderately high cutting velocities (60-100 m/min). Thus the increased damage rates can be rationalized by the increase in flow stress brought about by the higher strain rates.

At a constant strain, ε, the flow stress sensitivity to strain rate $(d\sigma/d \log \varepsilon)_\varepsilon$ is dramatically increased above a critical strain rate in a given material. The strain hardening exponent of the material, $d\sigma/d\varepsilon$, is also sensitive to the strain rate, ε, usually increasing with

an increase in strain rate. Thus, pronounced increases in damage rates are predicted because of the steep increase in flow stress with strain rate. This appears to be true in the case of chips generated at 2000 m/min. It is estimated that the strain rate at a cutting speed of 2000 m/min will be approximately 3.3×10^6/s, which probably exceeds the critical strain rate for the transition in the flow stress sensitivity of the material. It should be pointed out that an important consequence of the increase in flow stress of the material, brought about by the strain rate increase, will be to decrease the strain for void nucleation for a given interfacial energy.

1.4. High Strain Rate Deformation Behavior of Metals

In many metals, the strain rate sensitivity of the flow stress is known to increase dramatically when the strain rate is raised above 10^3–10^4/s. Follansbee [6] has reported results of measurements of the flow stress of FCC metals and alloys as a function of strain rate, over a wide range of strain rates. These measurements were carried out at Los Alamos National Laboratories using split Hopkinson pressure bar (SHPB) experimental techniques. Some results from the above work are included below to indicate the high strain rate behaviour of metals.

Stress/strain curves for Nitronic 40 stainless steel, measured over a wide range of strain rates, are shown in Figure 9. The steep increase in flow stress at a strain rate of about 5000/s, corresponding to rather a small strain (<0.01), is noteworthy. At a strain rate of 5000/s and a strain of 0.2, the estimated temperature rise is 62K and the consequent decrease in flow stress for adiabatic deformation is 125 MPa for Nitronic stainless steel. Figure 10 illustrates the experimental results of Campbell and Ferguson [7] which show the effects of strain rate and temperature on the lower yield shear stress of a 0.12% C plain carbon steel. Thus, steels (BCC) exhibit an increase in strain rate sensitivity when the strain rate is increased above 10^3–10^4/s. It should be pointed out that the excellent data of Campbell and Ferguson [7] have been used in the quantitative damage analysis of the chips by Chandrasekaran and Sowerby [5], see Section 2 of this report.

1.5. Steel Design for High Strain Rate Machining

There exists a critical strain rate above which the flow stress sensitivity to strain rate is dramatically increased. This critical strain rate can be realized by increasing the cutting speed. The damage rate can thus be promoted in high speed machining because of the increase in flow stress, k, brought about by high strain rates. Since the damage rates can be increased by increasing the flow stress of the material through higher strain rates characteristic of high speed cutting, it may be unnecessary to lower the microstructural interparticle spacing through free machining additives. The design philosophy of high strain rate machining should therefore be based on cleaner steels.

1.6. Fracture Criterion Based on Material Property

Tierlinck[8] has proposed a fracture criterion based on the concept of critical accumulated damage, which is independent of the stress state. This is based on experimental observations in a variety of spheroidized steels tested in tension under various stress states. It was found that the rate of damage development is decreased by the superimposition of an hydrostatic pressure, and that the number of voids participating in the final coalescence event increased with superimposed pressure while the areal fraction of voids just below the fracture surface was constant, regardless of the superimposed pressure, for a given material. At atmospheric pressure, the linkage of voids was predominantly in the lateral direction, i.e., transverse to the tensile axis, while even at moderate hydrostatic pressures void growth was along the tensile axis. Under the conditions of superimposed hydrostatic pressure where the void growth occurs along the tensile direction, the criterion adopted is that fracture occurs when the void dimension in the principal tensile stress direction reaches a critical value, which is determined by the microstructural distance. Void nucleation depends on the size of the particles, the larger particles cavitating first. Nucleation, therefore, does not occur at a unique strain, but can be considered as a front which travels through the particle size distri-

bution at a rate dependent on the imposed strain and hydrostatic pressure [9]. This has necessitated the consideration of continuous nucleation during deformation in damage analysis. Recent work has shown that void nucleation depends more on the local volume fraction of second phase particles, and is only weakly dependent on the average particle radius [10].

1.7. Design Criteria for Steels for High Strain Rate Machining

The design of microstructure for improved machinability can be analysed in terms of (a) critical accumulated damage at fracture and (b) damage rate as a function of strain rate. At moderate and low cutting speeds, the machinability of steels can be improved by making free cutting additives that essentially lower the critical accumulated damage at fracture. In the past, the speed of cutting has been limited by tool life. At moderate cutting speeds (<100 m/min), the strain rate sensitivity is not significant, and therefore the machinability can be improved by increasing the volume fraction of coarse second phase particles or inclusions, thereby decreasing the critical accumulated damage at fracture. The MnS inclusion population is increased by resulfurizing the steel and with further free cutting additives, such as lead or bismuth, the critical accumulated damage (at fracture) is decreased.

With the recent advances in tool materials, high cutting speeds have become a reality. Sintered carbide tools, ceramic tools, and tools coated by PVD and CVD techniques have vastly improved tool life performance. High strain rate machining imposes high normal stress at the tool tip. Modern tools are capable of performing well under this condition, thus paving the way for high productivity machining. In view of the economic gains in high productivity machining, the technological forecast is the development of high speed machining processes taking full advantage of high performance ceramic tools. Under conditions of high strain rate machining, it is possible to increase the damage rate through the dramatic increase in flow stress brought about by high strain rates. This would imply that free cutting additives are no longer required to lower the critical accumulated damage. Microalloying

additions may then be used to strengthen the steel, as long as they do not adversely affect the strain rate sensitivity of the material.

1.8. Design of Microalloyed Steels with Improved Machinability

There has been significant progress in Europe in the replacement of quenched and tempered grades by microalloyed medium carbon steels [11,12]. There has also been extensive work in France [13,14] on the replacement of medium carbon steels by low carbon microalloyed steels with marginal free cutting additives. Extensive machinability data are furnished to support the contention that the machinability of these steels is not substantially changed in spite of the improvement in strength brought about by microalloying.

SECTION 2

CHIP FORMATION MECHANICS AND DEVELOPMENT OF CONTINUUM MODELS FOR ANALYSING THE MACHINING OPERATION

R. Sowerby

N. Chandrasekaran

and

S.V. Subramanian

2.1 Mechanism of Chip Formation

The formation of serrated (or discontinuous) chips over a wide range of cutting speeds has been observed by many investigators. Some recent articles by Komanduri and his co-workers [15-17] provide a reasonably comprehensive review of the subject. Although much has been written on the topic, the mechanisms which control chip formation have not been clearly elucidated – at least, not in our opinion.

At high cutting speeds* e.g. surface velocities in the order of 2000 m/min for many steels, serrated chip formation is attributed to adiabatic shear mechanisms. However, we could not achieve these machining speeds in our laboratory, and we concentrated on a lower speed range, up to 400 m/min. Serrated chip formation at these surface speeds is not attributed to adiabatic shearing when cutting steels; although, as indicated above, the mechanisms have not been clearly identified.

It was the purpose of the present investigation to establish whether serrated chip formation, at the lower cutting speeds, was an inclusion-controlled ductile fracture mechanism. To test this hypothesis, an attempt was made to produce serrated chips using a model material.

2.1.1 Cutting Tests Using Plasticine as a Model Material

Orthogonal machining tests were conducted using plasticine as a model material, and a mild steel cutting tool with zero rake angle. The block of plasticine was mounted in a perspex container, which prevented transverse flow of the material. The experimental arrangement is shown in Figure 11 .

Initially cutting tests were performed at quasi-static speed on a solid block of plasticine. A continuous chip was formed without any visible serrations. The same experi-

---

* The term high is, of course, relative and depends upon the material being cut. Adiabatic shear mechanisms are reported to occur in titanium alloys at very low cutting speeds [17].

ment was repeated using a split block of plasticine. The block was split in a transverse direction, i.e. two blocks were placed in juxtaposition to make up the width of the perspex container. The experiment was performed to establish whether splitting the block had any influence on the chip formation. It appeared to have no effect, and as before a continuous chip was produced, see Figure 12. This latter figure shows one half of the block of plasticine removed from the perspex container.

The split block of plasticine was made heterogeneous by piercing one half of the block with a stylus to create a series of holes. Figure 13(a) shows the hole configuration in an uncut block, the other half of the plasticine block and a side wall of the perspex container have been removed in order to reveal the holes.

The sequence of photographs, Figures 13(b) - (d), illustrate how a serrated chip develops in the perforated block of plasticine. The experiments do not account for the origins of serrated chip formation when cutting materials. However, they do suggest that heterogeneities such as second phases, inclusions and the like could be possible causes.

In the next series of experiments a slit was cut into the free surface of the split block ahead of the partly formed chip. The technique will be clear from Figure 14. Before recommencing the cutting, a piece of paper was inserted into the slit. As the slit approached the cutting tool, the width of the split contracted and it was impossible to remove the paper. However, it is evident from Figure 14(a)-(e) that inserting slits into the free surface of the uncut blocks give rise to a discontinuous chip, and serves as further evidence of the presence of heterogeneities influencing the chip formation.

2.1.2 Discontinuous Chip Model Based on a Single Shear Plane

Komanduri and Brown [15] produced a micrograph of a serrated chip, shown here as Figure 15 and it can be seen that the flow pattern changes in the chip. On the assumption that a single shear plane hypothesis could be adopted to model the flow pattern illustrated in Figure 15 the shear plane would have to vary continuously between the angles θ_1 and θ_2, as

shown schematically in Figure 16. The smallest shear angle corresponds to the largest shear strain. Hence if micro-cracks or voids are going to coalesce, it seems reasonable to assume that this will occur when the shear strain is largest.

In the simple shear plane model it is proposed here that the crack runs from the free surface at A to some point B, shown chain dotted in Figure 16. A new shear plane forms, at angle θ_2, to join up with the end of the crack at B, as illustrated in Figure 16. The formation of the new shear plane, at angle θ_2 must depend upon some favourable energy dissipation condition; with the creation of the new shear plane the chip thickness is immediately reduced. However, the depth of cut does not remain constant, the crack has created a new free surface, and as the material moves towards the tool the original depth of cut, i.e. d in Figure 16 is approached. As the depth of cut, d, is being continuously restored the shear plane angle is simultaneously reduced from θ_2 to θ_1. The reduction in shear plane angle is associated with an optimum energy criterion. At the depth of cut, d, the minimum energy dissipation occurs when the shear plane is θ_1, at least this is the premise of the current model. Once the original depth of cut, d, and shear angle, θ_1, is reached, cracking again takes place and the whole cycle is repeated.

The foregoing is a phenomenological model and does not explain the actual micro-mechanisms which lead to serrated chip formation. It is included here for the sake of completeness.

2.2 Cutting Tests On Steels

2.2.1 Quick-Stop Experiments on Spheroidized Steels

Bars of AISI 1045, 1070 and 4340 steels were spheroidized in the conventional manner. Photomicrographs of the treated steels verified that the spheroidization had been complete.

The machining tests were performed on either a MASAK or COLCHESTER lathe. The surface cutting speed was varied over the range 50 to 400 m/min, and the rake angle of the tool was set at approximately zero degrees for all the tests.

In cutting tests of this sort an undisputed fact is the general shape of the deformation zone as shown in Figure 17 . The deformed region is generally divided into two zones, referred to as the primary and secondary deformation zones, which are identified in Figure 17 . Equivalent (or representative) strains of between 1.5 and 2.0 have been measured at the exit of the primary zone, while the strain level in the secondary zone is usually regarded as being at least double that of the maximum strain in the primary zone.

Quick stop experiments were performed on each of the three spheroidized steels. In each case the cutting speed was between 50 to 60 m/min, with a depth of cut of 1 mm and a feed of .2 mm/rev. Discontinuous chips were not observed under these cutting conditions. A surprising feature was the plastic deformation experienced by the spheroids, particularly in the 1045 and 1070 steels. The deformed spheroids were measured throughout the deformation zone, and this provided an indication, albeit approximate, of the strain distribution based on the average undeformed spheroid size.

As would be expected the strain increased across the primary zone from entry to exit. At the exit boundary AB, see Figure 17, a representative strain of about 1.75 was reached in the 1045 and 1070 steels. The strain increases in the region BC, see Figure 17, where the primary and secondary zones merged. A representative strain of over 2 was measured for the 1045 and 1070 steels in this region. Note that a natural strain of 2 corresponds to an elongation ratio of about 8 (7.39) i.e. the ratio, final length divided by initial length, equals 8. The deformed spheroids typical of the regions AB and BC are shown in Figure 18 and 19 respectively for the 1070 steel.

The spheroids were much finer in the 4340 steel and it was more difficult to evaluate the strain distribution from the deformation of carbides due to their finer size. With this material the grain boundaries provided an indication of the distribution and level of strain,

which was similar in nature to that observed with the 1045 and 1070 steels, see Figures 20 and 21. The strain showed a rapid increase at the junction of the primary and secondary zones, and continued to increase towards the rake face of the tool. This is evident from Figure 22 for the 4340 steel.

From the quick-stop tests on the spheroidized steels, which produced continuous chips, there was no evidence of either excessive cracking of the spheroids or decohesion from the matrix. Neither was there any evidence of significant void formations and coalescence at specific locations within the deformation zone. At the conflux of the primary and secondary zones the strain gradient is high and voids were observed in this region for each steel. However, the volume fraction of voids was not large enough to influence the chip formation, and voids in the deformed chip were rarely in evidence.

2.2.2 Machining Tests on AISI 4340 Steel

Many investigators have associated ductile fracture with the attainment of a critical amount of damage which is accumulated during a deformation process. Although the machining operation involves a complicated interplay of strain, strain rate, and temperature, it is postulated here that the occurrence of discontinuous chips is due to the accumulation of a critical amount of damage. How the damage is to be evaluated is discussed in the section dealing with Continuum Models.

To assess the damage hypothesis, machining tests were performed on a 4340 steel which had been subjected to different heat treatments.

Bars of a 4340 spheroidized steel and 4340 "as received" hot-rolled steel were cut in a Colchester lathe at surface speeds of 400 m/min. Discontinous chips could not be formed at this cutting speed with either material.

The "as-received" bar stock was hardened to 52 Rockwell C, and discontinuous chips were formed at a cutting speed of 136 m/min. Subsequent tempering of the same material reduced the hardness to 47 Rockwell C, and discontinuous chips were formed at a cutting

speed of 234 m/min. The metal cutting tests were carried out on a Colchester lathe, which did not have an infinitely variable speed drive. Hence, only discrete cutting speeds could be obtained and the exact speed at which the mode of chip formation changed over to discontinuous type could not be detected. However, a decrease in the material hardness did increase the critical cutting velocity at which the discontinuous chip formation occurred. Discontinuous chips obtained from the two tests referred to above are illustrated in Figures 23(a) and (b).

It is believed that the various heat treatments have produced steels which possess a different value of critical accumulated damage. This hypothesis can be verified by performing upsetting tests on cylindrical test pieces made from each steel.

It is not easy to quantify the influence of cutting speed on damage accumulation. Varying the cutting speed will affect the strain rate in the deformation zone, and also produce minor changes in the shape of the zone. Consequently the stress distribution within the zone will alter, and in turn this will influence the calculated damage accumulation.

2.3 Development of Continuum Models for Analyzing Machining Operations

No completely satisfactory analytical solution has yet been found which explains in full the mechanics of the machining operation. The principal analytical techniques which have been applied to study the problem are finite element methods (F.E.M.) and slip line field (S.L.F.) models. The main criticism levelled against the latter technique is that is is too idealized and does not account for the complicated interplay of friction, temperature, strain hardening and strain rate effects. The same could be said about finite element methods, since the present authors are not aware of any solutions which account for all of the above-mentioned parameters simultaneously. The most celebrated slip line field solutions are those developed by Palmer and Oxley [18] and Roth and Oxley [4]. The latter field is a refinement of the first, and a brief account of the principal features is given in the following section.

2.3.1 The Slip Line Field Proposed by Roth and Oxley [4]

The slip line was constructed from observations made during the orthogonal machining of a low carbon steel at a very low cutting speed (12.7 mm/min). The field discounts strain rate and temperature effects, but does allow for work hardening. Consequently the classical Hencky equations for a non-hardening solid have to be modified. The modified equations, as first proposed by Christopherson et al. [19], are

$$\begin{aligned} p - 2k\psi + \int \frac{\partial k}{\partial s_2} ds_1 &= \text{CONSTANT} \quad (\text{I or } \alpha - \text{line}) \\ p + 2k\psi + \int \frac{\partial k}{\partial s_1} ds_2 &= \text{CONSTANT} \quad (\text{II or } \beta - \text{line}) \end{aligned} \tag{1}$$

In the above equations p is considered positive when tensile and negative when compressive. The hydrostatic pressure being defined as:

$$p = \frac{1}{2}(\sigma_1 + \sigma_2), \tag{2}$$

where σ_1 and σ_2 are the principal stresses in the plane of deformation and considered positive when tensile.

The slip line field proposed by Roth and Oxley [4] is shown in Figure 24. The slip lines a1, a2, . . . ; b1, b1, . . . etc. are II(β) slip lines. Roth and Oxley, op cit, assumed that:

(a) The II (β) lines were lines of constant k, and therefore when working along the I(α) slip lines, a2, b2, . . . etc., the term $\partial k/\partial s_2$ could be taken as zero.

(b) All strain hardening had ceased by the time the exit slip line e2, e3 . . . had been reached, and along this slip line $\partial k/\partial s_1$ was zero.

(c) In view of the assumption (b), the slip line field adjacent to the tool face obeyed the Hencky equations for a non-hardening solid i.e. the work hardening having been saturated.

(d) When calculating the $2k\psi$ term along the I(α) slip lines, k was taken as the average value over the step considered.

A major finding of the Roth and Oxley analysis (which was also predicted in the earlier paper by Palmer and Oxley [18]) is that when moving along the entry slip line i.e. the a1, a2, . . . etc., from the free surface to the tool, the hydrostatic stress became progressively more tensile. In fact it becomes tensile at about point 4, see Figure 24.

Although the general shape of the field proposed by Roth and Oxley is not in question, there is some doubt about the predicted stresses, since the field itself is not entirely accurate. The exit slip line e2, e3, . . .etc., must bend to meet the free surface at $\pm 45°$, providing the free surface is continuous. The point e2 is almost contiguous with the free surface, and yet the inclination of the slip line there appears to be at right angles rather than $\pi/4$. The consequence of this is that at point e2 the hydrostatic pressure will be less than that at the free surface. This is not a carping criticism, but rather it is essential that all boundary conditions are satisfied. If this is violated then the field cannot satisfy compatibility of the stresses, i.e. the hydrostatic pressure at point e7 must balance when working from either the free surface along the exit slip line or from a1 to a7 through a7 to e7.

The slip line field of Figure 24 was constructed from observations made when cutting at very low speeds, in which case temperature and strain rate effects could perhaps be neglected. Over the past decade or so Oxley and his co-workers have published numerous papers dealing with the effect of strain hardening, strain rate, and temperature during metal cutting. However, a truly quantitative account of the role of these parameters has not been provided, nor have further statements been made as to the appropriateness of the field of Figure 24 or whether this field should be modified for higher cutting speeds. Furthermore, as already mentioned, strain hardening only was considered in the Oxley models [4,18] while in general the shear stress will vary with strain, strain rate and temperature and hence,

$$\frac{\partial k}{\partial s_{1,2}} = \frac{\partial k}{\partial \gamma}\frac{\partial \gamma}{\partial s_{1,2}} + \frac{\partial k}{\partial \dot{\gamma}}\frac{\partial \dot{\gamma}}{\partial s_{1,2}} + \frac{\partial k}{\partial T}\frac{\partial T}{\partial s_{1,2}} \qquad (3)$$

In the above expression the shear strain, γ, and the shear strain rate, $\dot{\gamma}$ have been employed.

The manner in which the above quantities vary along the slip lines will depend upon the forming process, but some statement can be made about the variation in the shear stress. For a strain hardening material (which is the norm for common engineering metals) $\partial k/\partial \gamma$ is positive but will decrease at higher strains. The quantity $\partial k/\partial \gamma$ can be positive or negative, depending upon the strain rate sensitivity of the material. The variation $\partial k/\partial T$ is undoubtedly negative, and thus for all common engineering metals the terms $\partial k/\partial \gamma$ and $\partial k/\partial T$ will be of opposite sign. The magnitude of these various quantities is of some concern since their exclusion could seriously affect the predicted stress distribution in the deformation zone using the modified Hencky equations.

2.3.2 A Proposed Slip Line Field

A proposed field is shown in Figure 25 for a tool with zero rake angle. The field has the same features as that proposed by Roth and Oxley [4], and shown in Figure 24, but the present field satisfies the boundary condition at the free surface and provides a consistent value for the hydrostatic pressure at a specified point when working around the slip line field mesh in either a clockwise or counterclockwise direction.

From published data, particularly the results of Oxley and his co-workers [20-22], estimates for some of the quantities on the right hand side of the equation (2) could be obtained. The strain and strain rate distribution in the deformation zone [20], was based on experiments performed at realistic cutting speeds, and although the temperature distributions [22] were determined from a F.E. analysis, the input data were obtained from experiments performed on plain carbon steels at realistic cutting speeds. Campbell and Ferguson [7] have shown the influence of strain, strain-rate and temperature on the flow stress of a 0.12%C plain carbon steel, and the present authors have used this information in their analysis of the machining operation.

The slip line field of Figure 25 in conjunction with published data in [7, 20-22], permits the stress distribution to be obtained through the deformation zone. In turn, the hole

growth model developed by Sowerby and Chandrasakaran [23,24] allows the damage accumulation to be evaluated for a volume element as it moves along a typical stream line, see section 2.3.3.

At the free surface, where no damage occurs, the p/k ratio is unity. In the interior region of the deformation zone, the local hydrostatic pressure decreases to less than the local flow stress of the material. Under the conditions where $p/k < 1$, one of the principal stresses will be tensile, which contributes to a positive damage rate. It is proposed that when moving along a stream line, microcracking will occur if the damage accumulated exceeds a critical value, which is characteristic of a given material. Since void growth dominates the damage process, the interparticle spacing and the particle size are important microstructural parameters.

Figure 26 shows the calculated variation in the p/k ratio when moving along the β-line cf, see Figure 25, for two cutting velocities. The p/k ratio is decreased when the cutting speed is increased, thereby increasing the damage rate.

Figure 25 shows ten stream lines (numbered 1 to 10) superimposed on the slip line field. The damage accumulation along each stream line was calculated for two cutting velocities (50 and 200 m/min) and the results are presented in Table 1. The variation in damage rate along streamline number 5 is shown in Figure 27 for the two cutting velocities. The results confirm that the damage rate increases with cutting velocity.

The authors consider the results to be of fundamental importance in the rationale behind the choice of steels for high productivity machining.

The calculations to determine the stress distribution in the deformation zone were based on slip line field analysis, an alternative approach would have been to have used a F.E. technique. However, it is considered that the same influence of the cutting speed on damage rate would have been revealed. The finite element method would be more appropriate if the cutting operation had to be modelled from the stage when the tool was about to enter the workpiece, the process is unsteady until the deformation zone and chip thickness is fully

developed. Quite apart from the material constitutive equation, a condition for separation (fracture) of the workpiece, i.e. the formation of the chip, will have to be invoked. A study of this type may prove informative about the uniqueness of the cutting process.

2.3.3 Damage Accumulation Based on Hole Growth

McClintock [25] analyzed the expansion of long cylindrical cavities under a triaxial stress system of fixed orientation. He derived a closed form expression for the damage rate, viz,

$$d(\ln F_{ca}) = \left\{ \frac{\sqrt{3}}{2(1-n)} \sinh\left[\frac{\sqrt{3}(1-n)}{2} \frac{\sigma_a + \sigma_b}{\bar{\sigma}} \right] + \frac{3}{4} \frac{\sigma_a - \sigma_b}{\bar{\sigma}} \right\} d\bar{\varepsilon} \tag{4}$$

The above expression represents holes growing in the a-transverse direction, σ_a and σ_b are the transverse stresses and c depicts the axial direction. Upon permutation of the symbols a, b and c (and allowing the axis of the cylinder to lie in any one of the three principal directions), analogous expressions can be obtained for the damage rate on the transverse directions.

Under plane-strain conditions which prevail during orthogonal metal cutting conditions, it can easily be shown that:

$$\sigma_c = (\sigma_a + \sigma_b)/2 \tag{5}$$

$$p = \sigma_c \tag{6}$$

and

$$\bar{\sigma} = 2k = \sigma_a - \sigma_b \tag{7}$$

Substituting eqns. (4) to (6) into eqn. (3), we get

$$d(\ln F_{ca}) = \left\{ \frac{\sqrt{3}}{2(1-n)} \sinh\left[\sqrt{3}(1-n) \frac{p}{2k} \right] + \frac{3}{4} \right\} d\bar{\varepsilon} \tag{8}$$

It is clear from equations (5) and (6) that the hydrostatic pressure p will be negative if both σ_a and σ_b are compressive. Furthermore, for the damage rate in (8) to be positive it is necessary that

$$\left| \frac{2}{\sqrt{3}(1-n)} \sinh\left[\sqrt{3}(1-n) \frac{p}{2k} \right] \right| < 1 \tag{9}$$

where p is compressive i.e. negative. The ratio of p/k to satisfy this condition will depend upon the value of n. For example, for n = 0.18, the value of p/k is −0.93.

The hydrostatic pressure distribution in the primary and secondary deformation zones can be established from the slip-line field solution. Hence the term in brackets in Eqn. (8) is known and can be evaluated as a function of $\bar{\varepsilon}$. Let

$$F(\bar{\varepsilon}) = \frac{\sqrt{3}}{2(1-n)} \sinh\left(\frac{\sqrt{3}(1-n)}{2} \frac{p}{k}\right) + \frac{3}{4}, \tag{10}$$

then the damage accumulated along the streamline can be determined from

$$A_{ca} = \int_0^{\bar{\varepsilon}} F(\bar{\varepsilon})\, d\bar{\varepsilon}. \tag{11}$$

It is proposed that when this value exceeds a critical value of accumulated damage, which is a characteristic of a particular material, then discontinuous chip formation will begin.

2.4. Estimating Critical Accumulated Damage

Deformation incompatibilities which exist between the matrix and second phase particles/inclusions normally result in local (microscopic) radial stresses at the particle/matrix interface, giving rise to void nucleation by decohesion; alternatively the second phase particles could crack resulting in void formation. The growth of these voids in the matrix, when subjected to a triaxial stress system in the gauge length set up between the adjacent voids, determines the damage process. The dispersion of second phase particles in a given material determines the critical gauge length, through a material parameter ln(λ/d) where λ is the initial void spacing and d the initial void dimension along the chosen orientation. The void growth under a triaxial stress system is complicated by the matrix deformation behaviour, which is a function of strain, strain rate and temperature. Sowerby and Chandrasekaran [24] have developed an upsetting test using a collar specimen to obtain a well defined strain path. The test allows the determination of critical accumulated damage by integrating damage along the strain path and at fracture, according to McClintock's model for void growth [25].

2.4.1 Computation of Critical Accumulated Damage Employing a Collar Test

Of the three different types of upsetting tests, viz., cylindrical compression, punch and collar tests, materials subjected to the collar test exhibit smallest fracture strain. Furthermore, the collar test obviates the need for a grid of lines at the equatorial free surface of the specimens, from which the surface strains can be determined; the hoop, ε_θ, and axial, ε_z, strains are obtained by measuring the diameter and thickness of the collar, respectively.

It was found to be an expedient to express ε_θ as an analytical function of ε_z, and for this purpose a cubic spline function approach was adopted. From the cubic spline interpolating function, the first derivative gives the strain ratio at any desired value of axial strain. As described in Ref. [24], the damage and accumulated damage in the void growth model employed are derived from the stress state at a point in a deforming solid. Assuming then that the material is isotropic and obeys von Mises yield criterion and associated flow rule, the stress history can be evaluated.

The hoop stress is tensile throughout the process, and hence the holes will increase in size in this direction. The rate at which this occurs will depend on the other two stress components, i.e. the axial and the radial stresses. The latter is always zero at the free surface. Hence, when applying eqn. (4), the 'a' transverse direction will correspond to the circumferential direction, while the second transverse stress corresponds to either axial or radial direction. The stress component selected was that which maximized the damage rate.

It follows that the damage accumulated in the deformation process can be evaluated by integrating eqn. (4). Irrespective of the type of the tests carried out, this integral should be a constant at fracture for a particular material. This value at fracture is defined as the critical accumulated damage (CAD).

Upsetting tests using the collar sample were performed on AISI 4340 steel test pieces which had been subjected to different heat treatments. The critical accumulated damage

factor (CADF) was evaluated for each heat treatment and the results are summarized in Table 2.

Machining tests were also performed on the same steels and it was established that discontinuous chips could be promoted in the steels with a low CADF. The maximum surface cutting speed that could be achieved with the available lathe and bar stock was 400 m/min., at this speed it was not possible to form discontinuous chips with either the "as received" or "spheroidized" material. The results of the cutting tests are also shown in Table 2.

SECTION 3

TOOL WEAR IN METAL CUTTING

N. Chandrasekaran

and

R. Sowerby

3.1. Introduction

Wear of cutting tools has been one of the most extensively researched fields of study in manufacturing engineering. The literature abounds with results obtained from experimental investigations on the effects of different metal cutting parameters on tool wear and tool life characteristics. In contrast, relatively few serious attempts have been made to establish reliable analytical models to facilitate the prediction of tool wear or life. Undoubtedly, a more thorough understanding of the wear and (brittle) fracture mechanisms will assist in the development of more reliable predictive models. However, until such models emerge, reliance is placed on empirical relationships to describe tool wear and the deployment of rather arbitrary fracture criteria. In what follows a selective review of tool wear is presented.

Modern cutting tools are usually brittle and while they may be less susceptible to abrasive wear they are often more prone to failure by edge chipping and fatigue failures, both of which are enhanced by intermittent cutting. It is pertinent to note that a simple elastic F.E.M. analysis [26] has shown that at two locations, one near the tool tip and the other on the rake face where the chip curls away, the highest tensile stresses can be generated. It follows that, at these locations the tool is more likely to experience brittle fracture.

In addition to tool breakage, it is also generally accepted that several mechanisms such as abrasive, adhesive, diffusive and corrosive wear can operate simultaneously.

3.2. Wear Mechanisms

The contact between two rough surfaces can be schematically represented as shown in Figure 28(a) [27]. Three contact junctions are illustrated and Figure 28(b) depicts a close-up view of one junction. The latter figure represents the tool-workpiece interface during the cutting process, and P_n is the normal force acting at the tool rake face whose magnitude will vary depending upon the location of the junction.

The variation of the normal compressive stress component is often assumed to decay exponentially, with the peak stress, $\sigma_{n\,max}$, occurring at the tool tip [28], see Figure 29. The

variation in shear stress, τ, is also illustrated in Figure 29, a plateau is reached near the tool tip and this is the yield shear stress τ_y.

The relative velocity between the chip and the tool, V, will vary depending upon the location. Figure 30, taken from from Reference [29], shows that the motion is tangential to the tool face in the region where sticking (or full) friction occurs, but once a normal component of velocity develops the chip curls away from the rake face. At the present time, neither the location of the point where the transition from sticking to sliding friction takes place nor the contact length, can be accurately predicted. Experimental SEM studies [30,31], which have examined the tool marks left on the underside of chips (quick-stop samples), have provided some insight into the size of these zones. The importance of the nature of the tool/chip interface cannot be overstated since a knowledge of the stresses in this zone is central to the prediction of tool forces and hence wear and/or fracture of the tool.

It has been suggested [29], that indirect evidence can help define the location of the transition zones on the rake face. For instance, the temperature distributions in the chip during metal cutting, obtained from finite element modelling of the process, is shown in Figure 31 [31]. Arbitrary units have been allocated to the constant temperature contours and the multiplication factors (linear or non-linear) will be determined from the cutting conditions and workpiece-tool material properties. Heat is generated at the interface due to friction between the tool and the sliding chip. Temperature gradients are established both along and across the interface. The nature of the gradients, as seen in the locus, are such that temperature drop occurs across the interface up to the transition point, depicted by the thick arrow in the figure. Beyond that point the curvature of the locus reverses, and this suggests that the frictional conditions change from sticking to sliding at that point. It is also reasonable to expect that the maximum deceleration of the chip material will occur in this region where the transition from sliding to sticking occurs. It is believed [29], that this will result in the greatest bulk velocity perpendicular to this interface.

3.2.1 Tool Wear by Solution

According to Kramer and Suh [29], this particular wear mechanism is activated by the solution of the tool material in the material being cut. They argue that the wear rate will have two components; the first one will depend upon the diffusivity of the diffusing tool constituent atom and also upon the tool-concentration gradient in the material being cut.

The second component is a function of the bulk velocity of the chip material at the tool-chip interface perpendicular to the interface. The normal velocity component, which acts away from the interface is likely to induce tensile stresses at locations in the tool which are directly beneath. This can result in an increase in the wear rate by promoting conditions which are more conducive to fracture by delamination. The important point to note is that a connection between the various mechanisms is a distinct possibility.

It is also suggested, op cit, that for carbide tool materials like, WC, NbC, TaC, ZrC, TiC, HfC, etc., wear by solution, will be the dominant mechanism. Hence, the potential for further improvement in the wear resistance of the carbides is very limited. However, oxide tool materials like, ZrO_2, Al_2O_3, Ti_2O_3, etc. are not as prone to wear by solution. Further improvements in mechanical properties of the oxides may lead to a substantial improvement in the wear resistance.

3.2.2 Wear Due to Adhesion

When metal surfaces are placed in contact, the real area over which they touch is usually small, see Figure 28(a). Under cutting conditions, the asperities can get sheared and the particles from the work material get pulled out. These particles can adhere to the tool at the interface thus altering the frictional conditions. This mechanism usually results in the loss of material from the workpiece rather than the tool, with material being built up on the tool.

3.2.3 Deformation Dominated Delamination Wear

The effect of interfacial force is to deform the metal surface, shearing it in the sliding direction. It is suggested in Reference [32] that in conjunction with the normal force, the uni-directional shearing of the metal surface, see Figure 32, can promote nucleation of subsurface voids. The voids can grow and link to produce a crack length parallel to the surface. When the crack length is large enough it breaks out to give a flake-like wear particle. The local stress conditions coupled with the deformation characteristics of the matrix will dictate the crack orientation and crack opening displacement. Of all the wear mechanisms this is the most amenable to analysis.

3.2.4 Wear Due to Abrasion

The traditional approach has been to introduce free cutting additives to the steel, such as sulphur and lead, to promote chip formation. The presence of abrasive particles in the workpiece, such as alumina for instance, can substantially increase the wear rate by abrading the tool surface. Although, one normally chooses a tool material which is harder than the material being cut, under certain heat treatment conditions, e.g., precipitation hardening, harder submicroscopic particles can appear in the work material which can dramatically increase the tool wear rate.

3.2.5 Oxidation and Melt Wear

Higher cutting velocities can generate interfacial temperatures sufficient to cause surface oxidation or even melting. In some cases, the wear rate may actually decrease if the increase in temperature results in the formation of a viscous oxide film at the interface. On the other hand when melting causes material loss the wear rate will increase.

3.3 Plane-Strain Elastic Finite Element (F.E.) Analysis

To determine the principal stresses σ_1 and σ_3 acting on a cutting tool, Sampath et al. [26], have carried out a simple elastic Finite Element (F.E.) analysis. The authors made the assumption that the variation of the normal (σ_n) and shear (τ) stresses on the rake face of the cutting tool was linear to keep the analysis manageable. The assumed characteristics are shown in Figure 33 and the mechanical properties employed corresponded to turning AISI 4340 steel at 61 m/min using a 6 weight percent cobalt-tungsten carbide tool. It should be noted that the yield stress of the work material was 1917 MPa.

Figures 34(a) and (b) show the contours of principal (elastic) stresses obtained from the computations. If σ_1 and σ_3 correspond to the algebraically greatest and smallest stresses respectively, then according to a simple relationship provided by Takagi and Shaw [38], the intensified local tensile stress, σ_i is given by

$$\sigma_i = 3\sigma_1 - \sigma_3 \tag{12}$$

Since σ_1 and σ_3 are known from the numerical calculations, the values of σ_i for different locations within the tool can be evaluated using Eqn. (12).

Figure 35 depicts the contours of σ_i, and it can be inferred from the figure that at two locations, one near the tool tip and the other on the rake face where the chip curls away, the highest tensile stresses are generated. One of the disadvantages of this type of elastic analysis is that the computed local tensile stress maxima, which for this particular cutting condition is 3103 MPa, can exceed the yield stress of the tool material. For example, if the power cutting force component, F_P, is doubled then the maximum stress value (6897 MPa) is more than doubled, refer to Figure 36(b). Altering the feed force cutting component, F_Q, does not affect the stresses to the same extent, see Figure 36(a).

Figures 36(a) and (b) are of paramount importance, since they depict the influence of either the change in the properties of the work material or the cutting conditions, like, feed rate, depth of cut, etc. on the development of local tensile stresses, which are responsible for

the fracture behaviour of the tool. An increase in the intensity of the local tensile stress will enhance the chance of tool fracture and increase tool wear.

3.4. Cutting Tool Grades

Schintlmeister et al. [33], have chronicled the development of materials used for cutting tools. Each new material has resulted in a dramatic increase in tool life and permitted the attainment of greater cutting speeds and feeds.

The first TiC coated cemented carbide tool tips were introduced in 1968. The TiC layer was 2 to 3 μm thick and an adjacent carbide zone, 3 to 5 μm thick, was decarburized to form an η-phase. Stjernberg [34] contends that during the deposition of the coating at about 1000°C, some carbon from the cemented carbide substrate diffuses into the coating resulting in a carbon deficiency in the substrate close to the subsurface. The inference is that it is not by design that the η-phase exists in coated tool tips. In recent years, TiN and HfN coatings have tended to replace TiC.

In 1973, multilayer coated tool tips based on TiC, Ti(C,N) (titanium carbonitride) and TiN, appeared on the market. The TiN coating formed the top layer, with underlayers of titanium carbonitride. The η-phase which is adjacent to the base material consisted of a TiC layer.

Five years later, Al_2O_3 coated (up to 10 μm thick) cemented carbide inserts were introduced. In addition to the homogeneous Al_2O_3 layer, the grade is characterized by an enrichment of mixed carbides (W-Ti-Ta mixed carbides).

Brandt [35] cites the relatively low transverse strength and toughness and their susceptibility to thermal cracking as the major obstacles to the acceptance of ceramic cutting tools. However, ZrO_2 additions have increased the toughness and TiN-TiC additions, have promoted an increase in the thermal-shock-resistance, thus paving the way for greater acceptance of ceramics as metal cutting tools.

3.5. Wear Mechanism Models

In the preceding sections, certain fundamental wear mechanisms and developments in tool materials have been discussed. It has been suggested [33] that, the contribution to tool wear by the various individual mechanisms can be hypothetically represented by the wear characteristics A to E, as shown in Figure 37. In the same figure, the curve F represents the total wear which is the sum of the individual mechanisms A to E.

It is possible to reduce diffusion wear by coating tool tips with layers of oxides, nitrides, etc. which reduce the diffusivity of the tool material. This is achieved as follows. Recall that tool wear by solution depends upon the diffusivity of the slowest diffusing tool constituent atoms in the work material. Since the chemical composition of the layers are different for different layers of the multilayer coated tool, the diffusivity will become a variable (parameter). The layers which have constituent materials with greater diffusivity will wear out quicker and expose layers which do not. In addition if the abrasive wear can also be reduced, then delamination wear becomes the dominant wear mechanism and this mechanism is more amenable to analysis.

The four principal areas of wear are identified as A to D in Figure 38 [30]. Honing of the cutting edge is performed to reduce edge chipping. A crater forms in the region A on the rake face, flank wear develops below the cutting edge in region B while grooves form at the extremities of the depth of cut at locations C and D. Based on extensive metallographic observations carried out on quick-stop specimens obtained while cutting AISI 1045 and 4340 steels, and from tool temperature estimates, Dearnley and Trent [30], have devised models to explain the phenomenon of tool wear in these four areas. The authors used cemented carbide inserts, both uncoated and coated with single as well as multilayers of TiC, TiN or Al_2O_3 as cutting tool materials.

3.5.1 Flank Wear

Honed cutting edges usually have a small radius in the order of 25 to 50 µm. Figure 39 (a) shows a section through the cutting edge of a coated insert before use and illustrates that the coating thickness is much smaller than the honed radius of the edge. The developing flank wear is shown schematically in Figure 39(b) and (c). The coating is first removed at approximately 40 µm below the level of the rake face, due to the edge radius, and further cutting extends the wear into the substrate.

3.5.2 Rake-face Wear (Cratering)

Dearnley and Trent [30] did not observe any wear on the rake face directly adjacent to the side cutting edge, except at the extremities of the depth of cut, i.e. regions C and D in Figure 38. These zones are characteristic of a delamination wear. The rake face suffers two types of wear; one a uniform wear of the top surface which can be attributed to chip movement. This is identified as a maximum wear area in Figure 40(a). Corresponding to this area, the authors detected the chip movement induced plastic deformation as evidenced by the formation of ridges and furrows on the tool face. The second type pertained to non-uniform deformation with the nucleation of a cavity. Fragments breaking away from point B in Figure 40(b) and (c) are responsible for the nucleation and growth of the cavity to form a crater. The propagation of submicroscopic cracks under the influence of tensile stresses can be the cause of the fragmentation. Interestingly, the authors observed that after the initial breakthrough the rate of cratering was impeded, especially once it pierced the coating. This can be explained by the fact that the coating is more brittle than the substrate,and hence the delamination type of fracture will be reduced quite considerably in the more ductile substrate.

3.5.3 Grooving Wear

Dearnley and Trent [30] observed that the wear rate at the extremities of the depth of cut, i.e. regions C and D in Figure 38, was greatly influenced by the atmosphere. When

cutting in a jet of oxygen the rate of wear was accelerated. It was surmised, op cit, that oxygen interacted with the surface of the tool, oxidizing it and making the surface easier to remove.

3.6. Wear-Mechanism Maps

Lim and Ashby [32] have queried the lack of an overall frame-work into which the various wear mechanisms can be fitted. They conclude, op cit, that a broader picture can emerge if wear-mechanism maps can be constructed, their objective was to show how the various mechanisms interface and to identify the dominant mechanisms under a set of operating conditions. From the literature they gathered extensive experimental data and coupled these with various numerical models and constructed the map shown in Fig. 41. The experimental results were obtained mostly from pin-on-disk configurations. This type of test employs one of the tool materials as the cylindrical sliding pin and the work material as the rotating disk. To study the detailed microstructural changes and to estimate the wear rate, cross sections of the wear track are cut perpendicular and parallel to the sliding direction [36] and examined under a scanning electron microscope. In Figure 41, the regimes where the different wear mechanisms dominate can be identified. Contours of constant normalized wear rates are mapped over each regime and in the figure discontinuities are evident at the boundaries between the different regimes. The map shown relates to the unlubricated wear of steel on steel, but in principle similar maps could be constructed for contacting dissimilar materials.

SECTION 4

INCLUSIONS AND TOOL WEAR

D.A.R. Kay

and

Jiang Junpu

4.1 Introduction

As discussed in previous sections of this report, one of the roles of free-machining additives in steel is the production of controlled dispersions of second phase particles which promote ductile fracture during machining and facilitate the chip formation process through void nucleation, growth and coalescence. Traditionally, 'soft' manganese sulphide inclusions have been used for this purpose, since dispersions of 'hard' second phase particles, particularly oxides, can also interact with the tool itself, accelerating tool wear processes. An essential feature of the metallurgical design of steels of improved machinability is therefore the elimination or modification of `hard' oxide inclusions, such as alumina, that promote abrasive tool wear.

The composition domains of 'soft', silicate inclusions, as defined by Bernard et al.[39], in both the $MnO-Al_2O_3-SiO_2$ and $CaO-Al_2O_3-SiO_2$ oxide systems are shown in Figures 42 and 43, respectively. The shaded areas at high silica contents give the compositions of 'hard' supercooled silicate liquid(s) while the shaded areas at lower silica contents represent the compositions of 'hard' inclusions which have either partially or totally recrystallized when subjected to the specific thermal history of the study.

In the production of steels of improved machinability, steelmaking deoxidation and ladle treatment practices must be designed to produce inclusions of controlled composition, volume fraction, morphology and distribution (inclusion engineering). For inclusion compositions in the $MnO-Al_2O_3-SiO_2$ system, for example, deoxidation practices can be controlled to produce spessartite ($3MnO-Al_2O_3-3SiO_2$) inclusions. For inclusions in the $CaO-Al_2O_3-SiO_2$ system, standard deoxidation practices are modified by calcium ladle treatments to give either anorthitic/gehlenitic inclusions in silicon/manganese deoxidized grades, or duplex calcium aluminate/calcium sulphide inclusions in aluminum deoxidized grades. In the latter case the abrasive alumina inclusions are modified to calcium aluminates on which 'soft' calcium sulphide can precipitate. Where the soluble aluminum content is too low ($<0.01\%$)

for conventional aluminum grain refinement, use is made of established microalloying technology.

It can be seen that the control of deoxidation and ladle treatment practices is essential to the production of modern free machining steels involving inclusion engineering. In order to facilitate this control, one of the objectives of this project was the development of thermodynamic models relating specific inclusion compositions to corresponding liquid steel compositions. Comparison of the thermodynamic predictions with the results of industrial practice is then to be used to determine the significance of kinetic effects during liquid steel treatment and the extent of reoxidation during transfer processes.

The ultimate objective of this cooperative work with industry, is to develop the industrial steelmaking control systems essential to inclusion engineering and the production of modern free-machining steels. Thermodynamic models developed for inclusions in the CaO-Al_2O_3, MnO-SiO_2-Al_2O_3 and CaO-SiO_2-Al_2O_3 are outlined below.

4.2. The CaO-Al_2O_3 System

The detailed thermodynamic treatment of inclusions in the CaO-Al_2O_3 system has been published elsewhere [40].

The relevant portions of the Fe-Ca-Al-O-S phase stability diagram, adapted to steelmaking conditions for an AISI 1045 steel at 1600 and 1550C, are reproduced in Figures 44 and 45 respectively. In both these figures, the series of bivariant (CaO)/CaS(s) equilibria are plotted in terms of log h_O vs. log h_S where h_O and h_S are the Henrian activities of oxygen and sulphur referred to their respective ideal 1 wt.% solutions in iron as standard states. These equilibrium lines represent the deoxidation/desulfurization relationships when the activities of lime and alumina are fixed by the two phase aluminate coexistencies given in the CaO-Al_2O_3 phase diagram, reproduced in Figure 46, and the given Henrian activities of aluminum which are representative of aluminum killed steels.

Referring to Figure 44, the line sequence e-d-c-b-a represents the progressive thermodynamic modification of alumina inclusions by calcium additions to an AISI 1045 steel at 1600C, assuming a constant aluminum activity of 0.015 (0.013 wt.%). The coordinates of the point 'c' indicate that solid CaS will not coprecipitate at 1600C with coexisting $CaO.2Al_2O_3(s)/CaO.Al_2O_3(s)$ inclusions unless the sulphur content is greater than 0.25wt.%. Clearly the thermodynamic prediction is that these duplex exogenous inclusions cannot form under ladle steelmaking conditions at 1600C.

In principle, the modification of $CaO.6Al_2O_3(s)$ inclusions to $CaO.2Al_2O_3(s)$ inclusions cannot take place until all the alumina inclusions have been modified to $CaO.6Al_2O_3(s)$ and the calcium activity of the steel would be fixed accordingly. Under industrial conditions where simultaneous deoxidation and desulfurization are taking place, the soluble calcium content of the steel is likely to be fixed at an oxygen activity which is set dynamically by the rate of oxygen removal by calcium and the rate of reoxidation of the molten steel by its oxidizing environment. A steady state Henrian oxygen activity of $1x10^{-5}$ at 1600C, for example, would result in a soluble calcium content of about 6 ppm. This would correspond to a desulfurization limit of about 60ppm sulphur for CaO(s)/CaS(s) coexistence. A lower steady state oxygen activity would result in a higher soluble calcium content and a lower desulfurization limit. The sulphur coordinate of the point 'b' ($h_S = 0.0045$) in Figure 45, which represents the phase stability diagram for an AISI 1045 steel containing about 0.05wt.% aluminum at 1550C, illustrates the difficulty experienced in the modification of alumina inclusions to 12CaO.7Al2O3 type aluminates unless the sulphur content is considerably reduced.

The effect of cooling prior to solidification is illustrated in Figure 47, where log h_{Ca} is plotted as a function log h_S at temperatures of 1550 and 1600C for an AISI 1045 steel containing 0.013wt.% Al. While the possibility of precipitating calcium sulphide from a steel melt in which two calcium aluminates coexist increases with decreasing temperature, substantial desulfurization can only occur in the presence of a liquid aluminate phase. Hence

the importance attached to the formation of the $12CaO.7Al_2O_3$ type aluminate in industrial calcium treatments.

The shift in the conditions for calcium sulphide precipitation to lower sulphur levels with decreasing temperature also provides an explanation for the presence of $CaO.Al_2O_3$ and $12CaO.7Al_2O_3$ inclusions partially or wholly surrounded by calcium sulphide in calcium treated aluminum killed steels. The predicted low soluble calcium contents indicate that there can be little further calcium modification of inclusions. The presence of separate calcium aluminate/calcium sulphide and unmodified manganese sulphide inclusions in calcium treated medium carbon free-machining steels, substantiates this point.

The continuous billet casting of aluminum-killed steels is subject to nozzle clogging problems associated with the precipitation of solid calcium aluminate and/or calcium sulphide inclusions. The conditions necessary for the formation of liquid calcium aluminate, without the precipitation of solid calcium sulphide are illustrated in Figure 48 for an AISI 1045 steel at 1600C containing 0.013wt.% Al. The Henrian oxygen activity window of $3x10^{-4}$ to $8x10^{-4}$, corresponding to 6-15 ppm by weight, gives the necessary conditions for the prevention of nozzle clogging when the sulphur content is less than 89ppm.

4.3 The MnO-SiO2-AlO3 and CaO-SiO2-Al203 Systems

The calculation of liquid steel compositions in equilibrium with corresponding oxide inclusions of given composition in the $MnO-SiO_2-Al_2O_3$ or $CaO-SiO_2-Al_2O_3$ systems has been carried out using the statistical thermodynamic slag model of Gaye [41]. This model enables the computation of the activities of components in complex slags (inclusions) from given binary parameters. Using deoxidation solubility product data in the literature, the liquid steel composition at a given temperature may be calculated from these calculated component activities for a given soluble oxygen activity. This soluble oxygen activity would be measured in practice using a commercial oxygen probe. The thermodynamic data base used in these computations is given in Tables 3 and 4. Copies of the computer programmes used for

inclusion/steel calculation in the $MnO-SiO_2-Al_2O_3$ are attached in the Appendix to this Section in order to illustrate the modelling techniques.

Typical results in the $MnO-SiO_2-Al_2O_3$ system are shown in Figures 49 and 50 where iso-weight percent curves for silicon and manganese are plotted for an AISI 1016 steel at 1600C. The curves are computed for Henrian oxygen activities of 0.0070 in Figure 49 and 0.0080 in Figure 50.

From the data given in Figure 49, a steel containing 0.6wt.% soluble manganese and 0.17wt.% soluble silicon with a soluble oxygen activity of 0.007 at 1600C would be in equilibrium with an inclusion containing 36%MnO, 31%SiO_2 and 33% Al_2O_3 by weight, i.e., the inclusion composition is given by the intersection of the two iso-weight percent curves. The corresponding inclusion composition of 45%MnO, 37%SiO_2 and 18% Al_2O_3 by weight for a similar steel with a soluble oxygen content of 0.0080 is obtained from the data in Figure 50. These results emphasize the importance of oxygen activity control in the production of steels with inclusions of given composition.

The pronounced effect of temperature and soluble oxygen content on the composition of an AISI 1016 liquid steel in equilibrium with an inclusion containing 30%MnO, 50%SiO_2 and 20%Al_2O_3 is shown in Figures 51 and 52, where the silicon and manganese contents, respectively, are shown as a function of the Henrian activity of oxygen. An inclusion containing 30%MnO, 50%SiO_2 and 20%Al_2O_3 by weight,for example, is in equilibrium with an AISI 1016 steel containing 0.28wt.%Mn and 0.10wt.%Si at 1550C, and 0.42wt.%Mn and 0.30wt.%Si at 1600C for a given Henrian oxygen activity of 0.0070

The results of a preliminary comparison of actual and calculated steel compositions in equilibrium with inclusions in the $CaO-SiO_2-Al_2O_3$ system for two Ca-treated industrial steels, are given in Tables 5 and 6. The important variable is the Henrian activity of oxygen, h_O, and although there is a temperature mismatch between the actual and predicted values, the agreement is sufficiently good to indicate that thermodynamic calculations of the type described above, can be used in the control of industrial inclusion engineering.

5. Discussion and Conclusions

Detailed SEM studies of chips and quick-stop samples were undertaken in order to map the damage associated with the type, size, volume fraction and local dispersion of second phase particles. There is evidence of void nucleation and growth, which lead to ductile fracture, on the fracture surfaces of chips formed during the machining of low and medium carbon steels over a wide range of cutting speeds (30-200 m/min). The fracture behaviour of the workpiece material was therefore analysed in terms of critical accumulated damage, which is defined as a material property that has to be exceeded for the onset of fracture. Factors which decrease the critical accumulated damage to fracture, such as a high volume fraction of second phase particles, large particle size and decreased interparticle spacing, will facilitate the chip fracture process.

The traditional approach to improve the chip fracture process for a given steel at low and moderate cutting speeds ($v < 100$ m/min), is to lower the critical accumulated damage value by the addition of free machining additives which increase the inclusion content and thereby decrease the intervoid distance. Even though 'soft' inclusions are programmed in order to aid fracture without incurring excessive tool wear, the inherent disadvantage of this approach is the loss of through thickness ductility of the steel with the increase in inclusion content.

Phenomenological observations of chips generated at high cutting velocities ($v >$ 200 m/min) show extensive void growth in comparison with chips generated at low cutting velocities. These increased damage rates are attributed to the increase in the material flow stress brought about by the high strain rates. In a material with a high characteristic critical accumulated damage to fracture an increase in the rate of damage accumulation will facilitate the chip fracture process. The increase in flow stress in high strain rate machining ($\dot{\varepsilon} > 10^3 - 10^4$/sec) results in an increased rate of damage accumulation and strain localization. Under these circumstances, the use of free machining additives, which decrease the critical accumulated damage to fracture at low/moderate cutting speeds, resulting in good

chip formation, may no longer be necessary. The concept of clean steel design for high strain rate machining has been proposed, whereby good chip formation can be achieved in a calcium deoxidized steel strengthened by microalloying. Although high strain rate machining imposes a high normal stress at the tool tip, modern ceramic tools are capable of performing well even under this stringent condition.

Complementing the phenomenological observations on chips and quickstop samples, the mechanics of the machining operation have been analysed using slip line field models. This work has extended the slip line field solutions, developed for a strain hardening material by Oxley and his co-workers over the last two decades, taking into account temperature and strain rate effects. These models have enabled the stress distribution, expressed in terms of the ratio of the local hydrostatic pressure to the local flow stress of the material, the p/k ratio, to be determined through the deformation zone. A hole growth model allows the damage accumulation to be evaluated for a volume element as it moves along a typical streamline. Under conditions where $p/k < 1$, one of the principal stresses is tensile, which contributes to a positive damage rate. Microcracking occurs if the damage accumulated exceeds a critical value, characteristic of a given material. One of the results of fundamental importance is that the p/k ratio decreases with increasing cutting-speed resulting in an increased damage rate, thus providing the rationale behind the choice of steel for high productivity machining.

Upsetting tests, using 'collar' testpieces obtained from samples of an AISI 4340 steel which had been subjected to different heat treatments, were carried out and the critical accumulated damage factors (CADF) for each heat treatment evaluated. Machining tests on the same steels at low cutting velocities established that discontinuous chip formation was promoted in steels with low CADF values.

A literature review on tool wear in metal cutting was carried out in order to provide the basis for future research on tool wear processes. The role of inclusions in determining the rate of flank and crater wear has been identified. The effect of inclusion composition and

morphology on these two types of wear at different cutting speeds will be the subject of future research.

As an aid to inclusion engineering in steelmaking, equilibrium models relating steel and inclusion chemistries for given temperatures and soluble oxygen contents have been developed. Models developed for inclusions in the $CaO-Al_2O_3$, $MnO-SiO_2-Al_2O_3$ and $CaO-SiO_2-Al_2O_3$ systems will be tested under industrial conditions and used to control aluminum deoxidation practices and calcium ladle treatment processes.

ACKNOWLEDGEMENTS

The financial support of the Department of Energy, Mines and Resources (CANMET) is gratefully acknowledged as are helpful discussions with Professor J.D. Embury. Special thanks are due to Mrs. Teresa Castillo for her assistance with the SEM work. The provision of steelmaking data by the Lake Ontario Steel Co. Ltd. and the technical support of the Niobium Products Company Inc. is also gratefully acknowledged.

The high speed chips used in this investigation were provided by the research group headed by Professor Tönshoff at IFW, University of Hanover, GFR.

REFERENCES

1. S.V. Subramanian and D.A.R. Kay: 'Development of Non-Leaded Free Machining Steels – Phase IV'. Final Report, DSS File No. 12SV-23440-3-9134,1985.

2. S.V. Subramanian and D.A.R. Kay: 'Microstructural Engineering for Improved Machinability'. CSIRA-ISIJ Japan/Canada Seminar, December 3-4, 1985.

3. S.V. Subramanian: 'Philosophy of Cleaner Steel Design for High Strain Rate Machining'. Interim Progress Report, DSS Contract #OST85-00201,March,1986.

4. R.N. Roth and P.L.B. Oxley: J. Mech. Engg Sci.,vol.14,1972, p.85.

5. R. Sowerby and N. Chandrasekaran: 'Metallurgical Aspects of Machinability in Medium Carbon Steels'. Interim Progress Report, DSS Contract #OST85-00201, March, 1986

6. P.S. Follansbee: 'High Strain Rate Deformation in FCC Metals and Alloys'. Int. Conf. on Metallurgical Applications of Shock Wave and High Strain Rate Phenomena', Portland, Oregon, 1985.

7. J.D. Campbell and W.G. Ferguson: Phil. Mag. vol. 21, 1970, pp. 63-75.

8. D. Tierlinck: 'Influence of Stress States on Various Fracture Modes'. Ph.D Thesis, McMaster University,1983, p. 32.

9. D. Tierlinck, M. Ashby and J.D. Embury: 'Damage Accumulation during Ductile Rupture and the Development of Failure Maps'. Proc. of the 6th. Int. Conf. on Fracture (ICF6), New Delhi, India, 1984.

10. J.D. Embury, McMaster University: Private Communication.

11. S. Engineer and A. von den Steinen, Thyssen Edelst. Tech. Ber. 1980, 6, (2) p. 85.

12. M. Baffigi, S. Corso, A. Giaccone and L. Infante: 'Production and Service Properties of Microalloyed Components for the Motor Industry'. Met. Sci. & Tech., vol. 3(2), 1985, pp. 55-65.

13. L. Backer, P. Charlier and R. Hechelski: 'Microalloyed Steels for Mechanical Engineering – Development and Use'. United Nations Seminar, Turin, Italy, 1982.

14. L. Backer and P. Charlier: 'High Strength Drawn Bars of Microalloyed Steels with Improved Machinability for Mechanical Engineering'. ASM Conf. on 'High Productivity Machining', New Orleans, 1985.

15. R. Komanduri, and R. Brown: "On the Mechanics of Chip Segmentation In Machining", Trans. ASME J. Engg. for Industry, Vol. 103, pp. 33-51, 1981.

16. R. Komanduri: "High-Speed Machining", Mech. Engg., Vol. 107, pp. 64-76, 1985.

17. R. Komanduri, T.A. Schroeder, D.K. Bandhopadhyay, and J. Hazra, "Machining of Titanium and Its Alloys", Advanced Processing Methods for Titanium, Ed: Hasson, D.F. and Hamilton, C.H., TMS Fall Meeting, Louisville, Kentucky, pp. 241-256, 1981.

18. W.B. Palmer, and P.L.B. Oxley, "Mechanics of Orthogonal Machining", Proc. I. Mech. Enggr., Vol. 173, pp. 623-654, (1959).

19. D.G. Christopherson, P.L.B. Oxley, and W.B. Palmer, "Orthogonal Cutting of a Work-hardening Material", Engineering, Vol. 186, pp. 359-381, 1974.

20. P. Mathew, W.F. Hastings and P.L.B. Oxley, "Machining - a Study in High Strain Rate Plasticity", Inst. Phys. Conf. Ser. No. 47, Chapter 4, The Institute of Physics, pp. 360-371, (1979).

21. P.L.B. Oxley and W.F. Hastings, "Predicting the Strain-rate in the Zone of Intense Shear in which the Chip is Formed in Machining from the Dynamic Flow Stress Properties of the Work Material and the Cutting Conditions", Proc. Roy. Soc., Vol. 356 A, pp. 395-410, (1977).

22. A.O. Tay, M.G. Stevenson, G. de Vahl Davis, and P.L.B. Oxley, "A Numerical Method for Calculating Temperature Distributions in Machining, from Force and Shear Angle Measurements", Int. J. Mach. Tool Des. Res., Vol. 16, pp. 335-349, (1976).

23. R. Sowerby, and N. Chandrasekaran, "Application of McClintock's Ductile Fracture Model by the Growth of Holes to the Tensile Straining of Some Spheroidized Steels Under Superimposed Hydrostatic Pressures", Matls. Sc. and Engg., Vol. 79, pp. 15-26, (1986).

24. R. Sowerby, and N. Chandrasekaran, "The Prediction of Damage Accumulation when Upsetting AISI 1045 Steel Specimens, Based on McClintock's Model", Matls. Sc. and Engg., Vol. 79, pp. 27-36, (1986)

25. F.A. McClintock, "A Criterion for Ductile Fracture by the Growth of Holes", Trans. ASME., J. Appl. Mech, Vol. 35, pp. 363-371, 1968.

26. W.S. Sampath, Y.M. Lee, and M.C. Shaw, "Tool Fracture Probability under Steady State Cutting Conditions", ASME J Engg. for Ind., Vol. 106, pp. 161-167, (1984).

27. F. McClintock, and A.S. Argon, "Mechanical Behaviour of Materials", Addison-Wesley Publishing Company, Inc., U.S.A. (1966).

28. E. Usui, T. Shirakashi, and T. Kitagawa, "Analytical Prediction of Cutting Tool Wear", Wear, Vol. 100, pp. 129-151, (1984).

29. B.M. Kramer, and N.P. Suh, "Tool Wear by Solution: A Quantitative Understanding", ASME J Engg. for Ind., Vol. 102, pp. 303-309, (1980).

30. P.A. Dearnley, E.M. and Trent, "Wear Mechanisms of Coated Carbide Tools", Met. Technol., Vol. 9, pp. 60-75, (1982).

31. G. Boothroyd, "Temperatures in Orthogonal Metal Cutting", Proc. IMechE, Vol. 177, pp. 189-195, (1963).

32. S.C. Lim, and M.F Ashby, "Wear-Mechanism Maps", Acta Metall., Vol. 35, pp. 1-24, (1987).

33. W. Schintlmeister, W. Wallgram, J. Kanz, and K. Gigl, "Cutting Tool Materials Coated by Chemical Vapour Deposition", Wear, Vol. 100, pp. 153-169, (1984).

34. K.G. Stjernberg, "Fracture Toughness of TiC-Coated Cemented Carbides", Metal Science, pp. 189-192, (1980).

35. G. Brandt, "Flank and Crater Wear Mechanisms of Alumina-Based Cutting Tools When Machining Steel", Wear, Vol. 112, pp. 39-56, (1986).

36. C. Chiu, J.D. Embury, and T. Castillo, "Metallography of Adhesive Wear in Aluminium Alloys" (To appear in Metallography), (1987).

37. G. Vierregge, Zerspanung der Eisenwekstoffe, Stahleisen, Düsseldorf, Second Edn., pp. 83, (1970).

38. J. Takagi, and M.C. Shaw, "Brittle Fracture Initiation Under Complex Stress States", ASME J Engg. Ind., Vol. 105, pp. 143-149, (1983).

39. G. Bernard, P.V. Riboud and G. Urbain: Rev. Met. CIT, vol. 78 No. 5, 1981, pp. 421-434.

40. D.A.R. Kay, S.V. Subramanian and R.V. Kumar: 'Inclusions in Calcium Treated Steels', Proceedings of the Second International Symposium on the Effects and Control of Inclusions in Steels, 25th Conference of Metallurgists, Toronto,1986.

41. H. Gaye and D. Coulombet: 'Donnees thermochimiques et cinetiques relatives a certains materiaux siderurgiques' IRSID PCM-RE.1064, 1984.

42. C. Gatellier and M. Olette: IRSID PCM-RE.475, 1977.

43. J.F. Elliott: 'Electric Furnace Steelmaking', 1985, p.265. AIME.

44. D. Ghosh and D.A.R. Kay: J. Electrochem. Soc., vol.124, 1977, pp. 1836-1845

45. H. Gaye et al.: 'Slags and Inclusion Control in Secondary Steelmaking', IRSID PCM-RE.1277, 1986.

46. G.K. Sigworth and J.F. Elliott: 'The Thermodynamics of Liquid Dilute Iron Alloys', Metal Science. vol.8, 1974, pp.298-310.

47. Seikohanno Suisho Heikochi, ed. by 19th. Comm. (Steel) of Japan Society for the Promotion of Science, Nikkan Kogyo Shinbunsha, Tokyo, 1969, p.144.

48. M. Kohler, H.-J. Engell and D. Janke: 'Solubility of calcium in Fe-Ca-X_i melts', Steel Research, vol.56, No.8, 1985, p.419.

TABLE 1

Damage Accumulation along each Streamline in Figure 25 for Two Cutting Velocities, 50 m/min and 200 m/min.

Stream Line	Accumulated Damage Cutting Velocity	
	Vc = 50 m/min	Vc = 200 m/min
1	.240	.245
2	.263	.270
3	.282	.290
4	.301	.311
5	.305	.314
6	.292	.298
7	.247	.248
8	.160	.152
9	.010	−.014
10	−.145	−.190

TABLE 2

Results of Machining Tests and CADF Measurements for an AISI 4340 Steel.

Heat Treatment	Hardness	CADF	Discontinuous Chips
OIL QUENCH	56 ROCKWELL "C"	0.172	Yes, at 136 m/min
OIL QUENCH AND TEMPERED	47 ROCKWELL "C"	0.224	Yes, at 234 m/min
AS RECEIVED	298 BHN	0.367	No, at Max Speed 400 m/min
SPHEROIDIZED	224 BHN	0.755	No, at Max Speed 400 m/min

TABLE 3

Thermodynamic Data Base

Reaction [Si]1w/o + 2[O]1w/o = SiO2(s) [41]

$$[Si]1w/o + 2[O]1w/o = SiO_2(s)$$

$$\log K = (31040/T) - 12.0$$

Reaction [Mn]1w/o + [O]1w/o = MnO(s) [42]

$$Mn(l) + 1/2O_2(g) = MnO(s)$$

$$\log K = (15050/T) - 6.70$$

$$Mn(l) = [Mn]1w/o$$

$$\Delta G^o = 976 - 9.12T \text{ cal}$$

$$1/2O_2(g) = [0]1w/o$$

$$\Delta G^o = -28000 - 0.69T \text{ cal}$$

$$[Mn]1w/o + [O]1w/o = MnO(s)$$

$$\log K = (14988/T) - 6.48$$

Reaction 2Al(l) + 3/2O2(g) = Al2O3(s) [44]

$$2Al(l) + 3/2O_2(g) = Al_2O_3(s)$$

$$\Delta G^o = -394680 + 77.8T \text{ cal}$$

Reaction Al(l) = [Al]1w/o [43]

$$Al(l) = [Al]1w/o$$

$$\Delta G^o = -15100 - 6.67T \text{ cal}$$

Reaction 2[Al]1w/o + 3[O]1w/o = Al2O3(s) [43,44]

$$2[Al]1w/o + 3[O]1w/o = Al_2O_3(s)$$

$$\log K = (61304/T) - 20.37$$

These data were used in calculations for the $MnO - SiO_2 - Al_2O_3$ system.

Reaction 2[Al]1w/o + 3[O]1w/o = Al2O3(s) [43]

$$2[Al]1w/o + 3[O]1w/o = Al_2O_3(s)$$

$$\log K = (62680/T) - 20.54$$

These data were used in calculations for the $CaO - SiO_2 - Al_2O_3$ system.

Reaction [Ca]1w/o + [O]1w/o [40]

$$[Ca]1w/o + [O]1w/o = CaO(s)$$

$$\log K = 25655/T - 7.65$$

TABLE 4

Interaction Parameters e_j^i [43,46]

i/j	Al	C	Si	O	Mn	Ca
Al	0.0446[45]	0.043[46]	0.058[46]	−1.17[45]	− − −	−0.054[45]
C	0.091[45]	0.140[46]	0.180[45]	−0.130[45]	−0.070[45]	−0.337[45]
Si	0.056[45]	0.080[46]	−0.107[45]	−0.140[45]	0.060[45]	−0.097[45]
O	−1.98[45]	−0.098[45]	−0.250[45]	−0.174[47]	−0.083[46]	− − −
Mn	−0.003[45]	−0.012[46]	0.033[45]	−0.030[45]	−0.003[45]	−0.010[48]
P	− − −	0.051[46]	0.110[46]	0.070[46]	−0.0035[46]	− − −
S	0.030[45]	0.046[46]	0.056[45]	−0.133[45]	−0.0048[45]	− − −
Ca	−0.049[45]	−0.101[45]	−0.068[45]	− − −	− − −	−0.002[46]

Note: Figures in parentheses refer to the references in the literature.

TABLE 5

Comparison of actual and calculated steel compositions.
Inclusion Composition: 23.3%CaO, 33.4SiO_2, 43.3%Al_2O_3

	hO	C	Si	Mn	Al	Ca	S
Actual 1578C	0.0041	0.153	0.180	0.69	0.004	0.0005	0.022
Calc. 1550C	0.0040	0.160	0.175	0.70	0.001	<0.0001	0.020
Calc. 1580C	0.0055	0.160	0.173	0.70	0.001	<0.0001	0.020

Note: Actual contents are total concentrations in wt.%.
Calculated contents are soluble concentrations in wt.%.

TABLE 6

Comparison of actual and calculated steel compositions.
Inclusion Composition: 23.5%CaO, 39.8SiO_2, 36.7%Al_2O_3

	hO	C	Si	Mn	Al	Ca	S
Actual 1578C	0.0038	0.161	0.210	0.85	0.005	0.0018	0.032
Calc. 1550C	0.0040	0.160	0.210	0.85	0.0007	<0.0001	0.030
Calc. 1580C	0.0055	0.160	0.210	0.85	0.0008	<0.0001	0.030

Note: Actual contents are total concentrations in wt.%.
Calculated contents are soluble concentrations in wt.%.

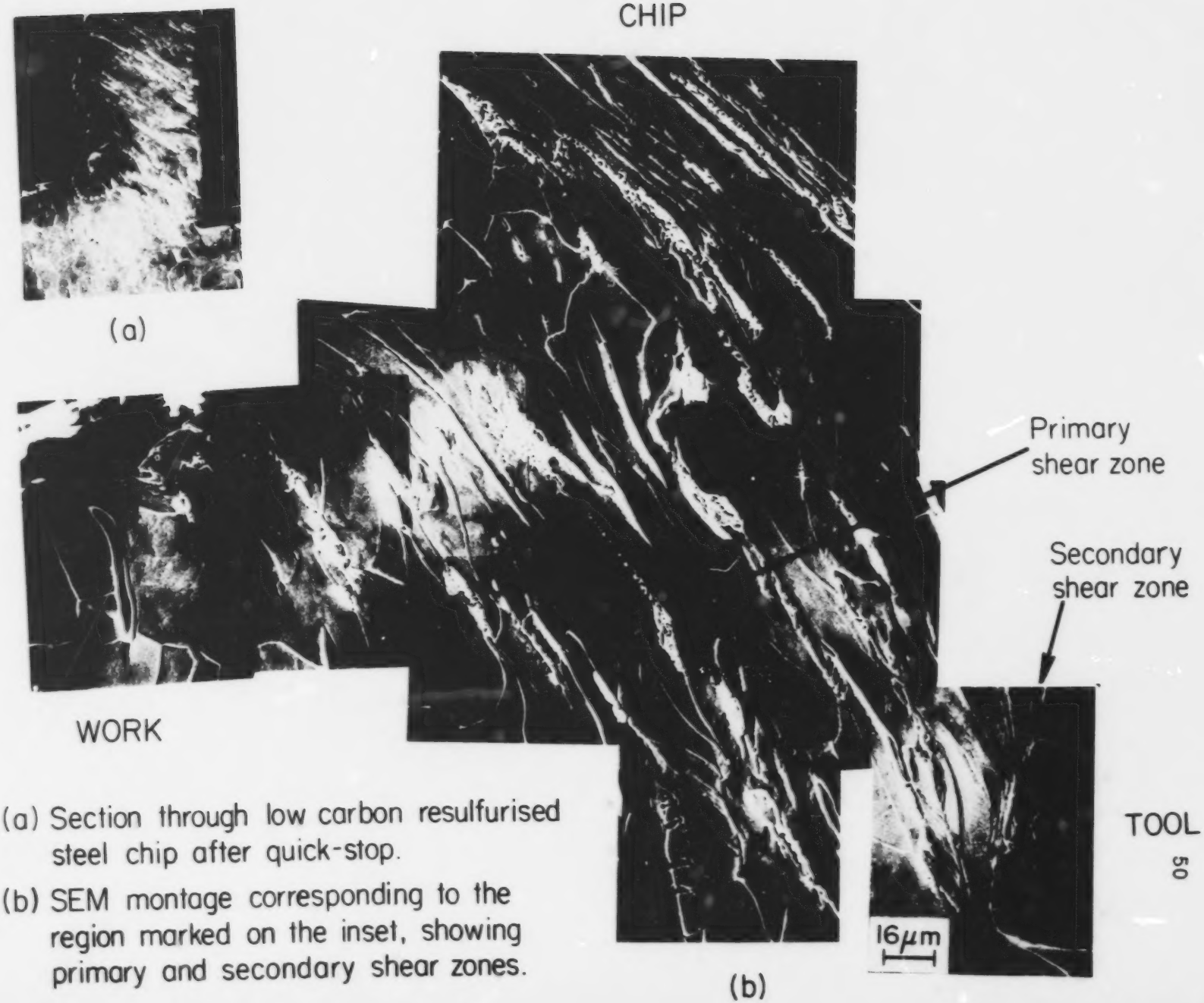

Fig 1 (a) Section through low carbon resulfurised steel chip after quick-stop.

(b) SEM montage corresponding to the region marked on the inset, showing primary and secondary shear zones.

(a)

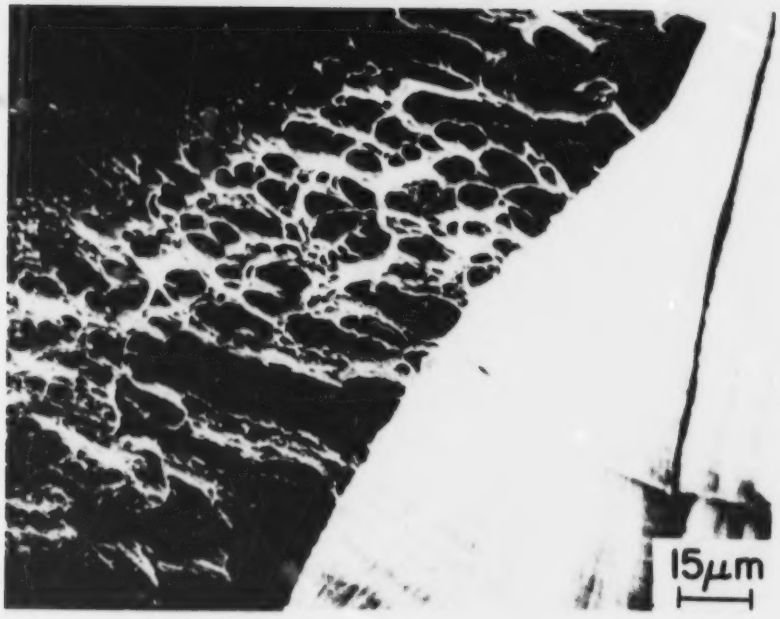

(b)

Figure 2: SEM micrographs of shear localised chips obtained from 42CrMoS4V grade steel machined at a cutting speed of 2000 m/min.
a) the ductile and shear fracture zones, and
b) voids around second phase particles in the ductile rupture zone.

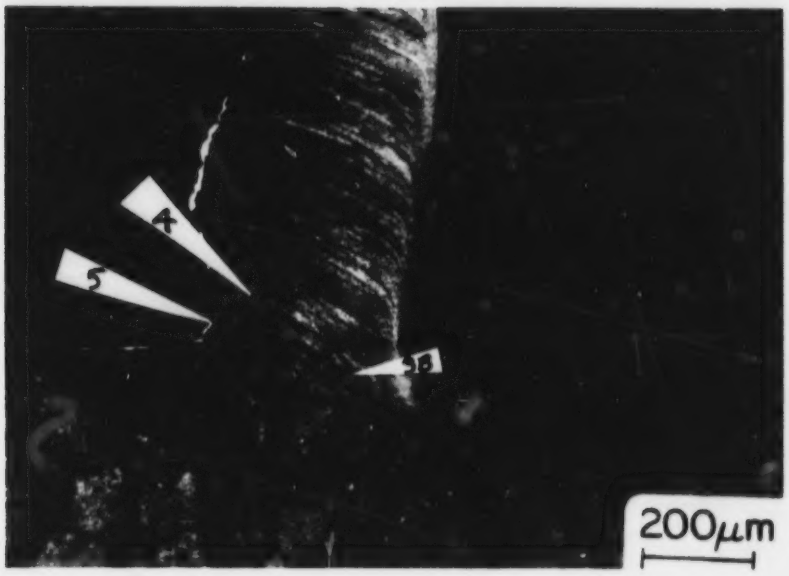

(a)

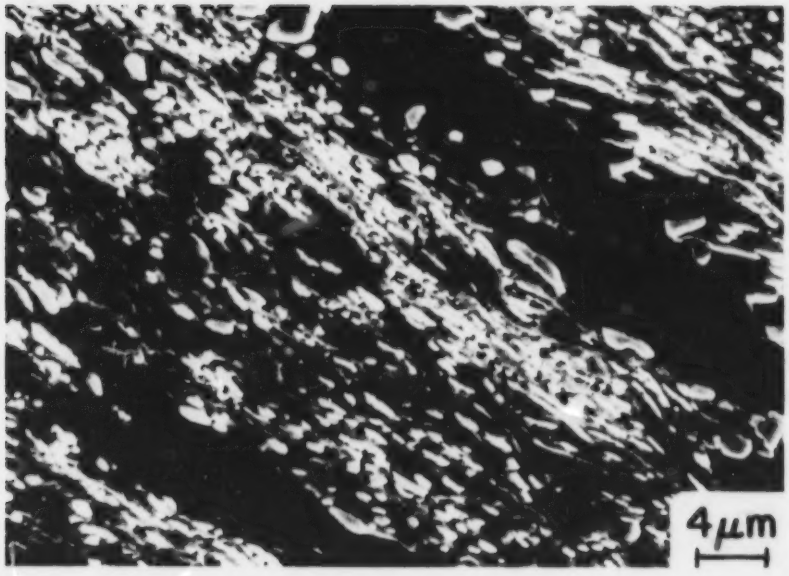

(b)

Figure 3: SEM picture of a quick-stop chip obtained from a partially spheroidised AISI 1045 grade steel at a cutting speed of 60 m/min. The locations of SEM pictures shown in Figs. 3(b), 4 and 5,are indicated in Fig. 3(a). Fig. 3(b) is an SEM picture showing the damage associated with carbides occurring in the primary shear zone.

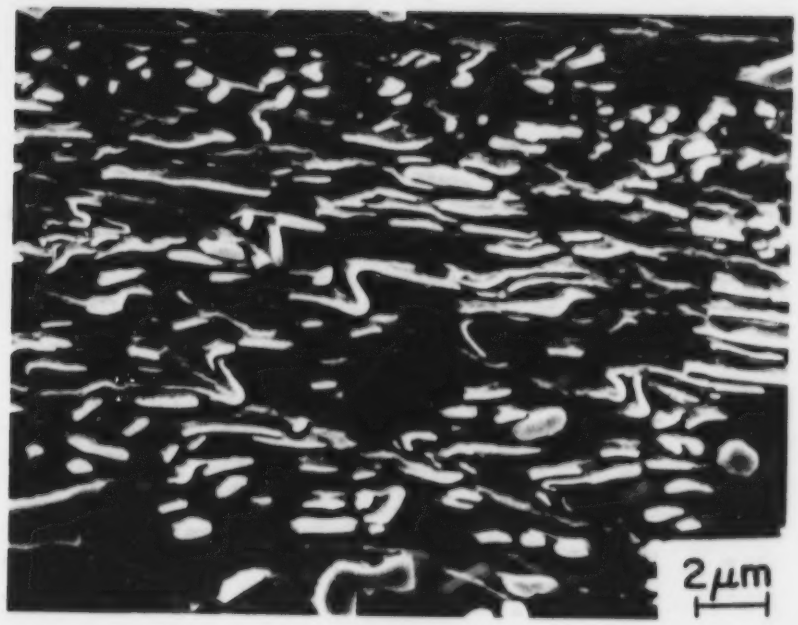

Figure 4: SEM picture of a region close to the free surface of the chip, showing the severely deformed carbides under the influence of the local hydrostatic pressure.

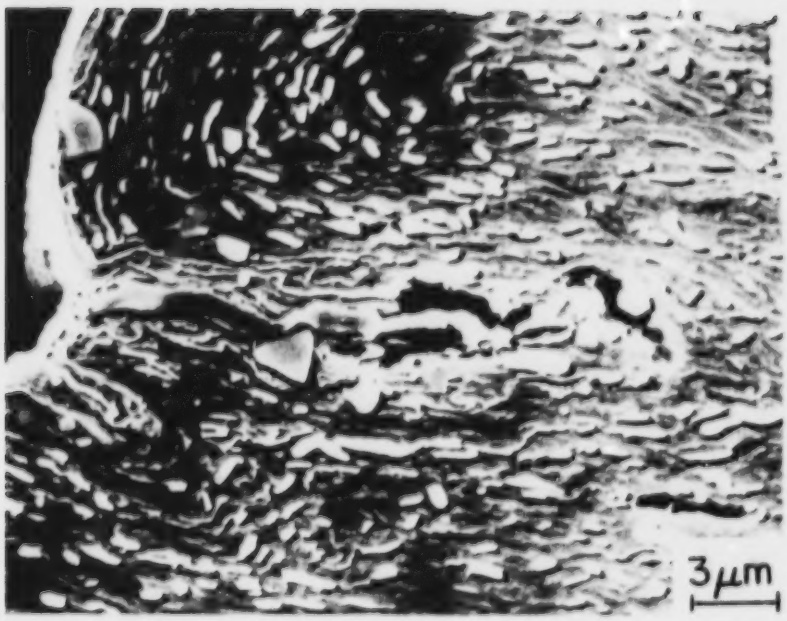

Figure 5: An SEM picture of a region close to the free surface of the chip (see Fig. 3(a) for location), showing negligible damage. Note the severe plastic flow of material.

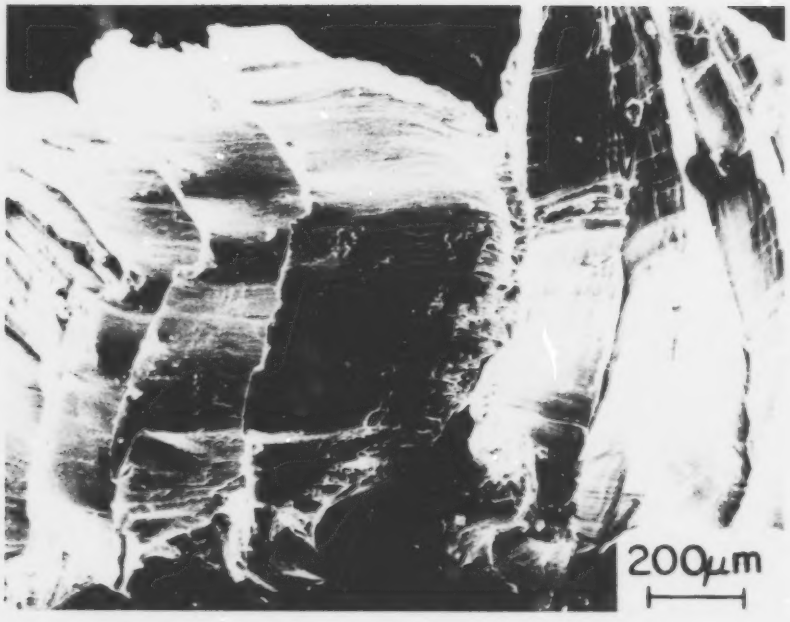

Figure 6: A fully segmented chip showing well-deformed crack initiation and crack propagation regions obtained from a 42 CrMoS4V steel at a cutting speed of 200m/min.

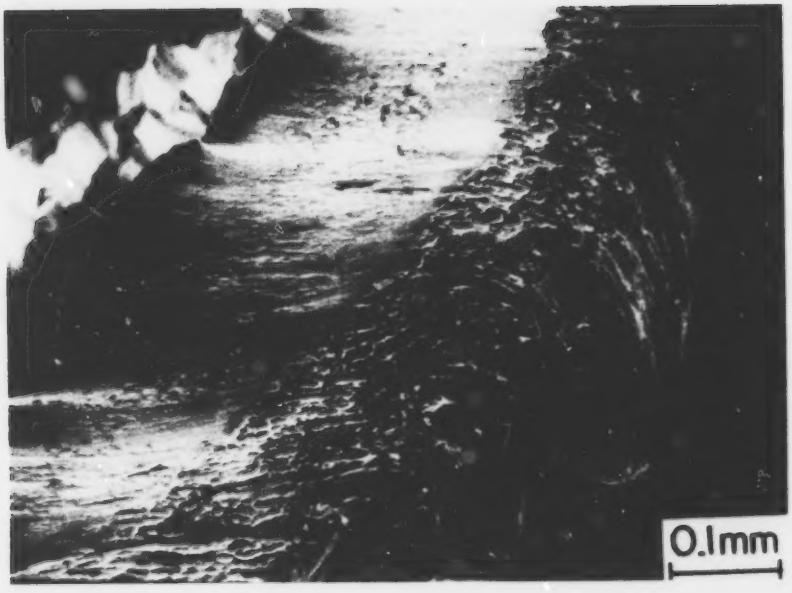

Figure 7: The fracture surface of a fully segmented chip obtained from a 42 CrMoS4V steel at a cutting speed of 2000 m/min, showing that the coalesence of voids is complete in the crack initiation region.

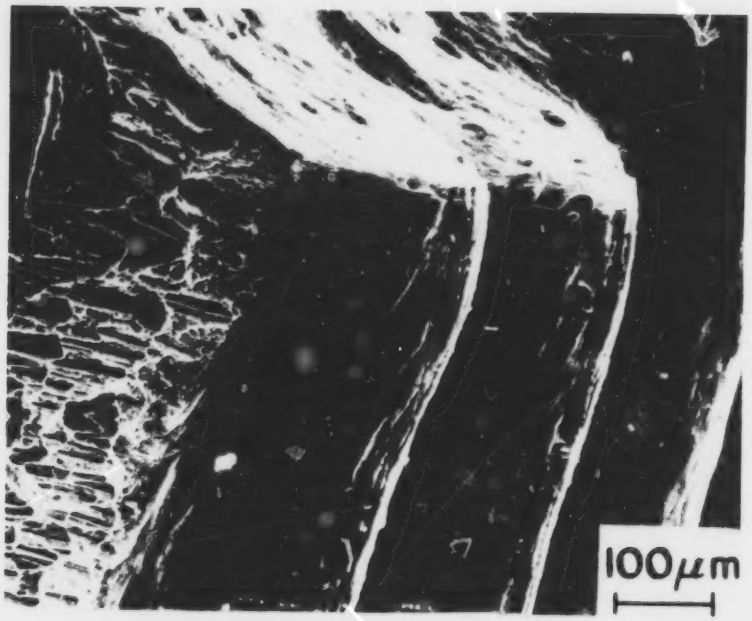

(a)

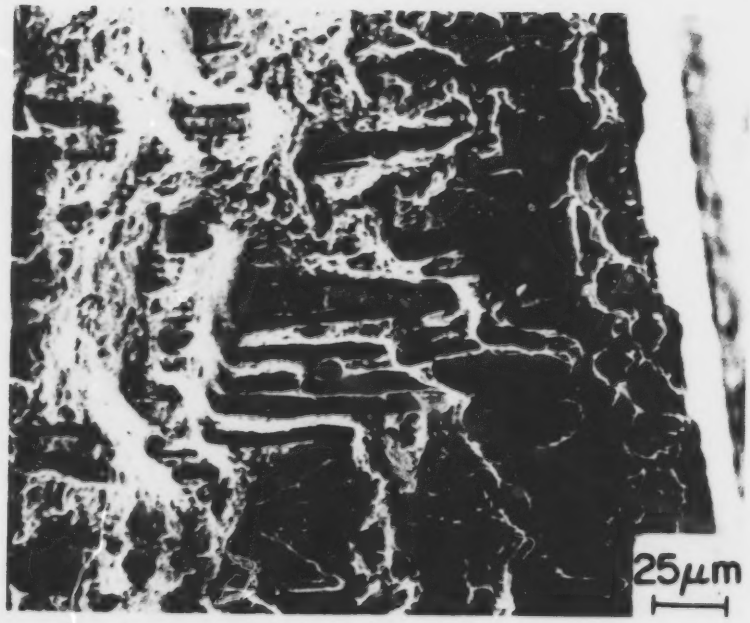

(b)

Figure 8: (a) A SEM picture showing damage in the fracture surface of a partially segmented chip obtained from 42 CrMoS4V steel at a cutting speed of 200 m/min.
(b) An SEM picture showing extensive void growth (damage) associated with MnS inclusions in the chip from Figure 8(a).

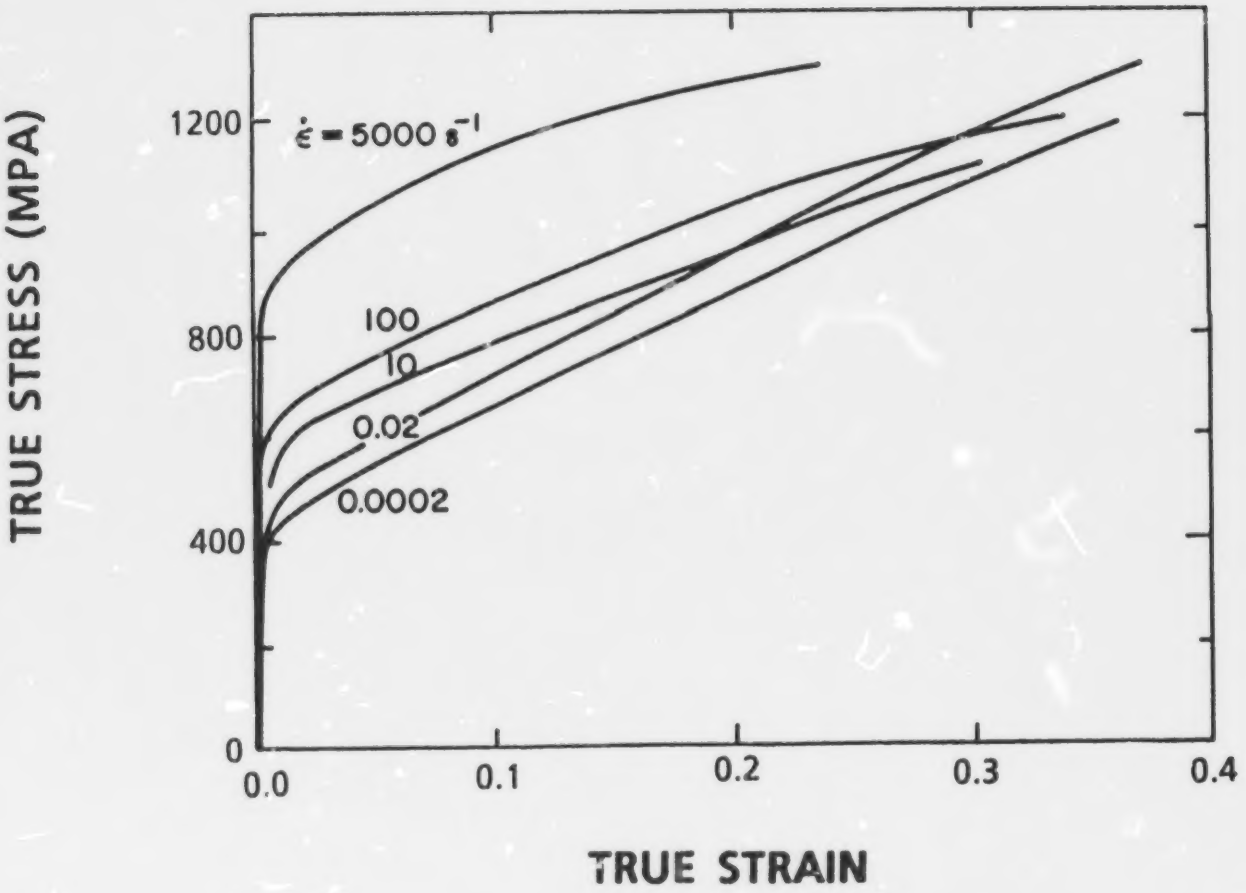

Figure 9: Stress-strain curves for Nitronic 40 stainless steel measured over a wide range of strain rates. After P.S. Follansbee[6].

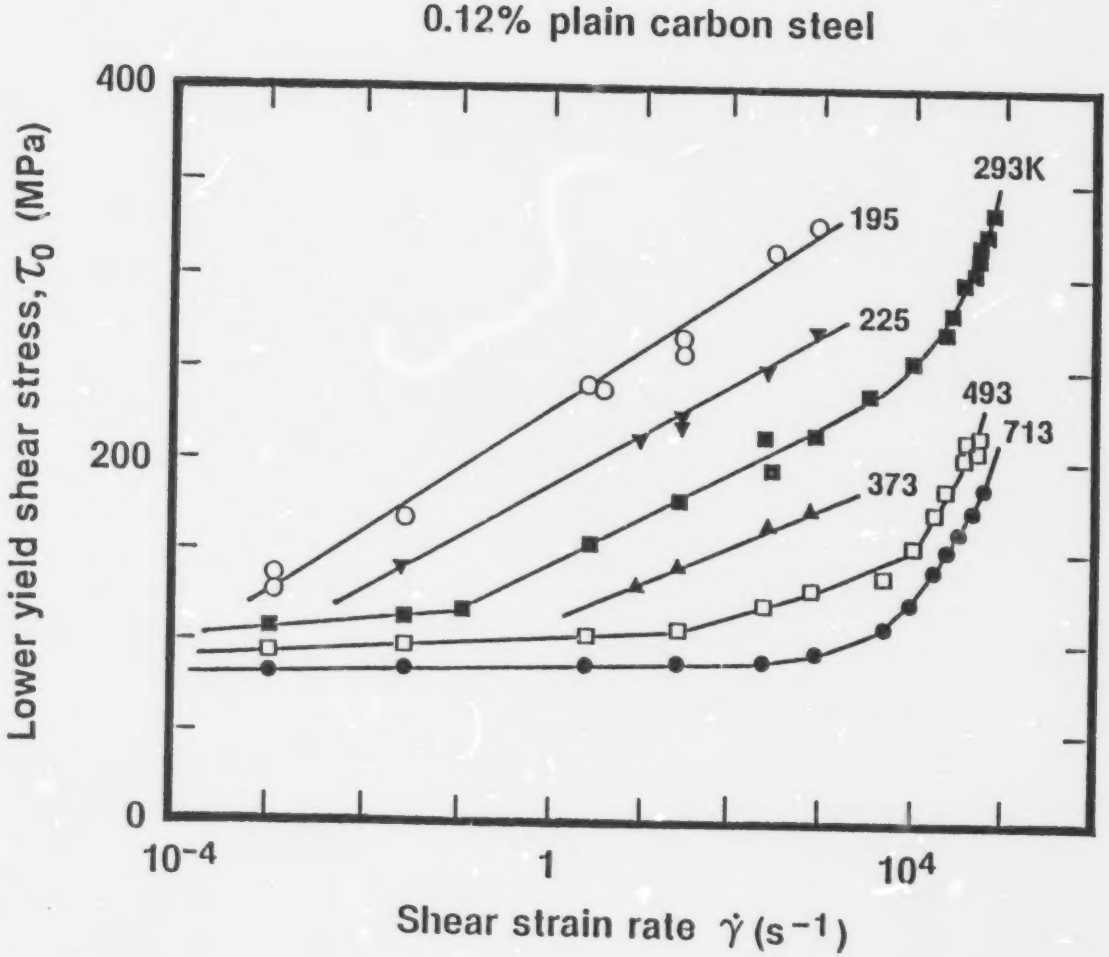

Figure 10: Experimental results of Campbell and Ferguson[7] showing the effects of strain rate and temperature on the lower yield shear stress of a 0.12% C steel.

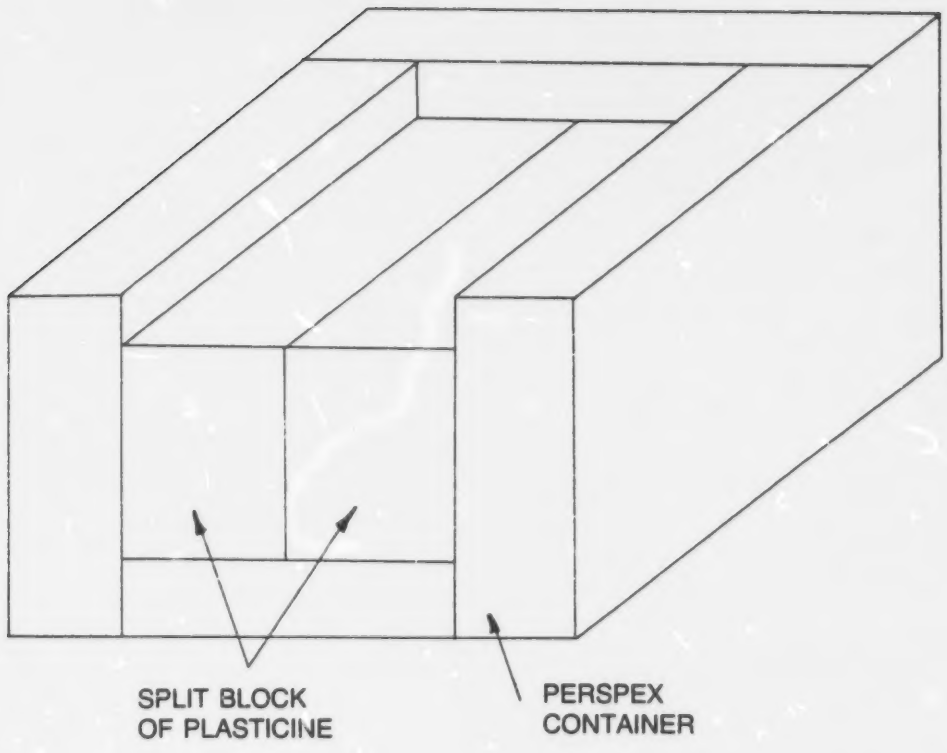

Figure 11: Orthogonal machining test using plasticine as a model material - An experimental arrangement.

Figure 12: Experiment to illustrate that splitting the block has no influence on the mode of chip formation.

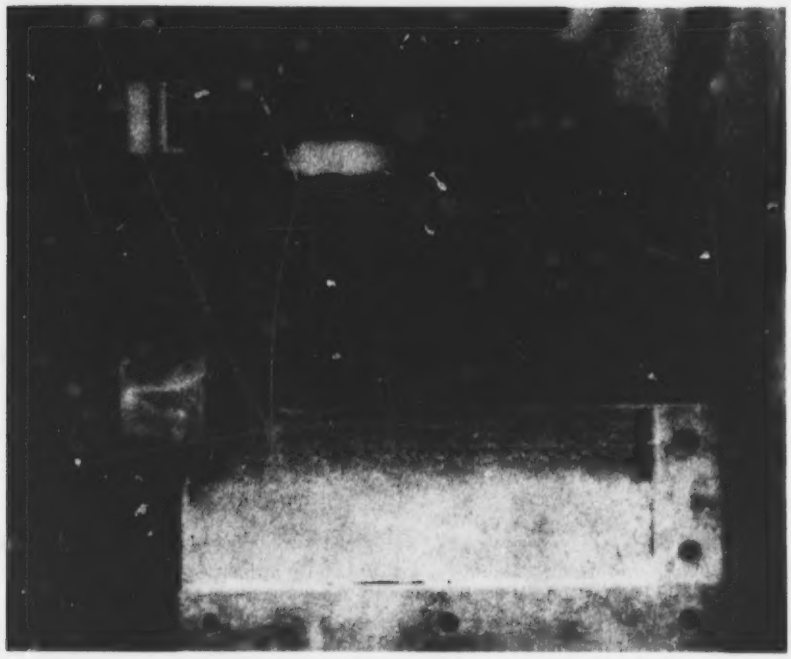

(a)

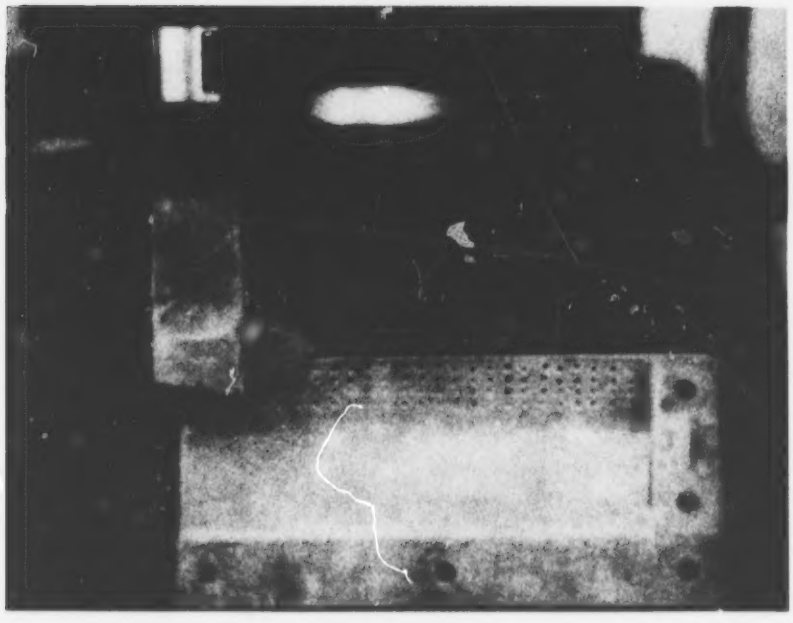

(b)

Figure 13: Photographs to illustrate the development of a (a and b) serrated chip in the perforated block of plasticine.

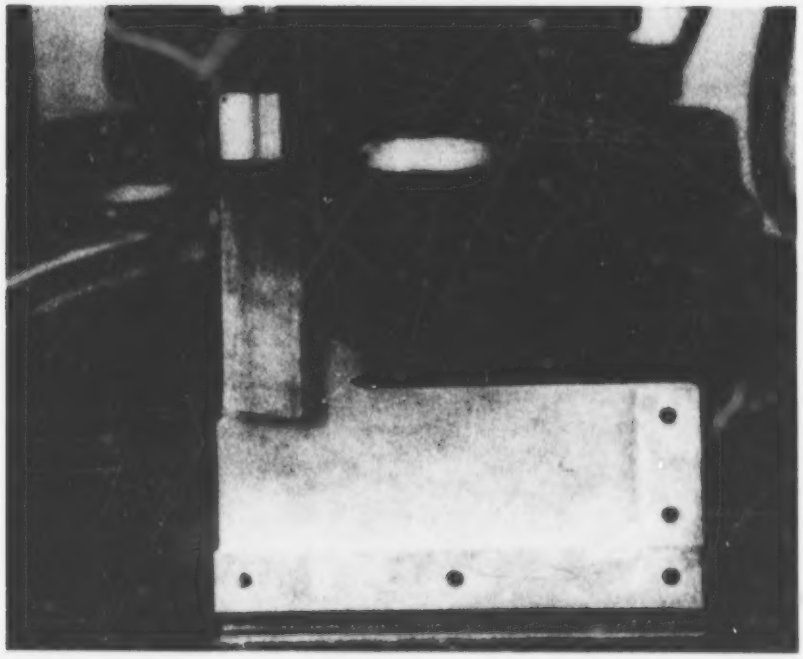

(a)

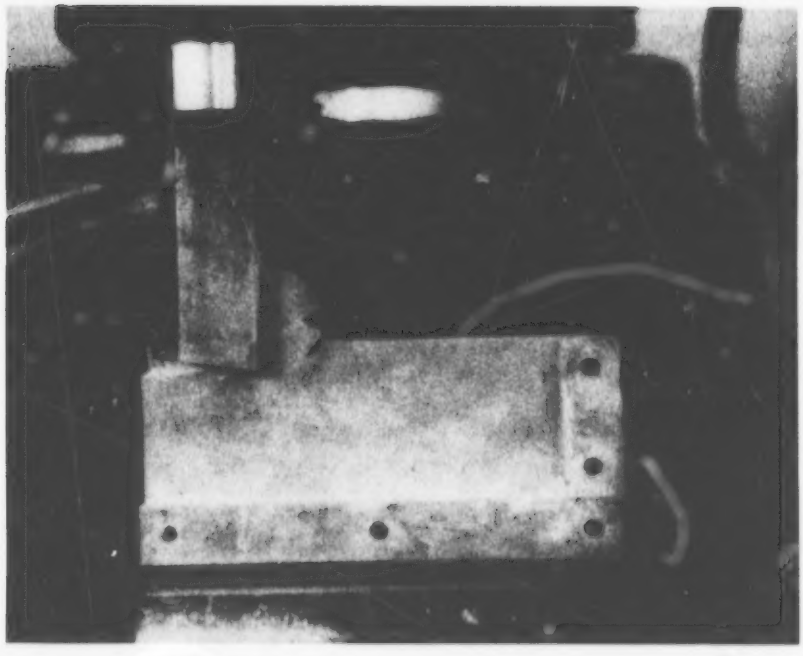

(b)

Figure 14: (a and b) Experimental evidence to show how the presence of heterogeneities influence chip formation.

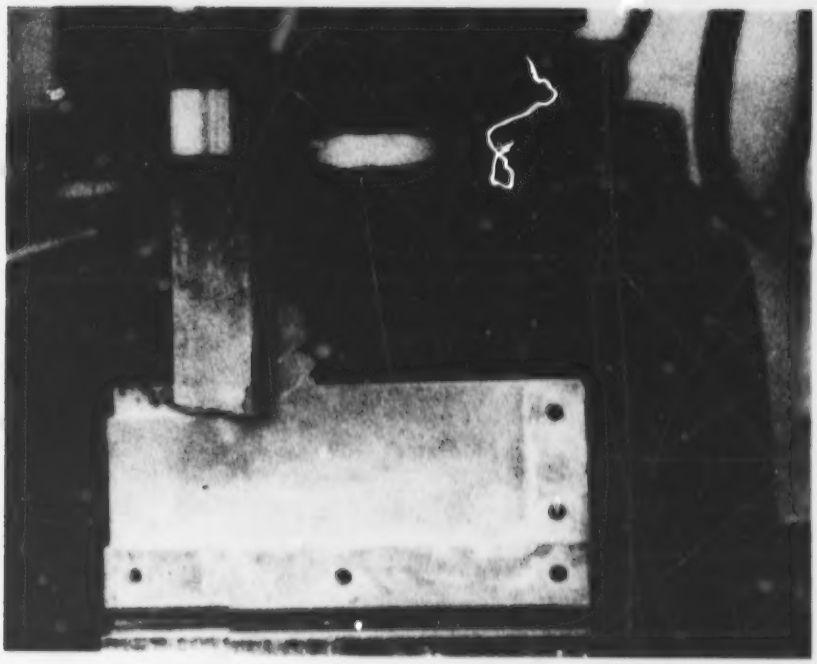

(c)

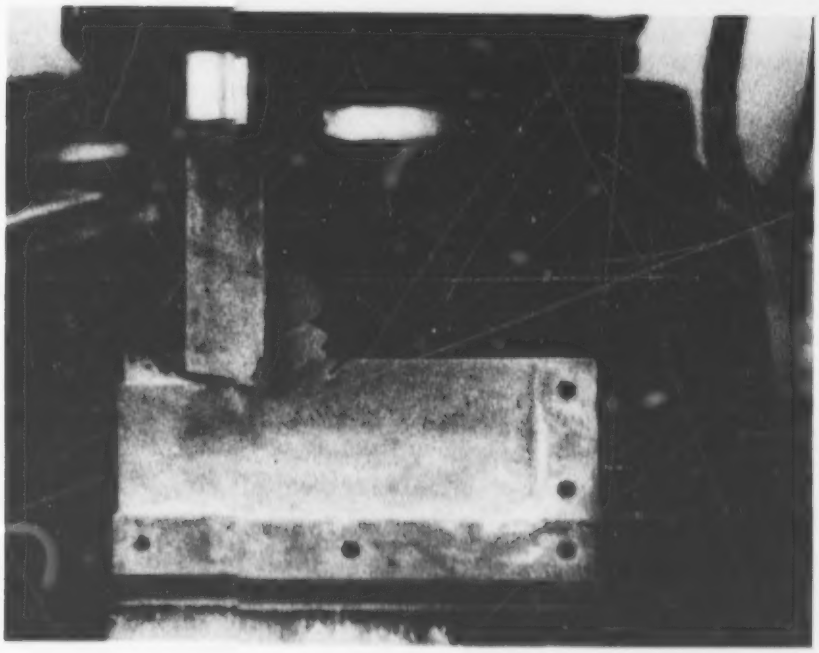

(d)

Figure 14: (c and d) Experimental evidence to show how the presence of heterogeneities influence chip formation.

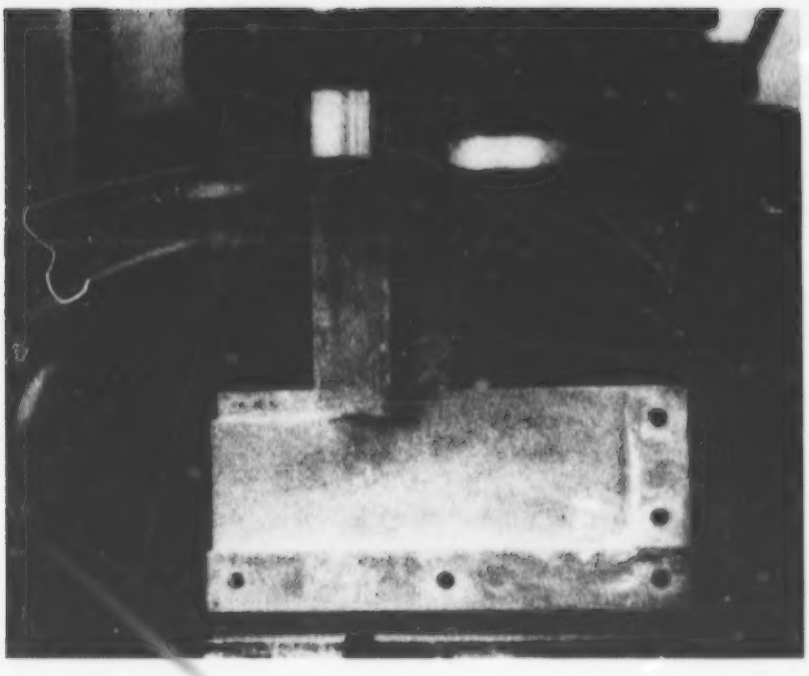

(e)

Figure 14: Experimental evidence to show how the presence of heterogeneities influence chip formation.
(e)

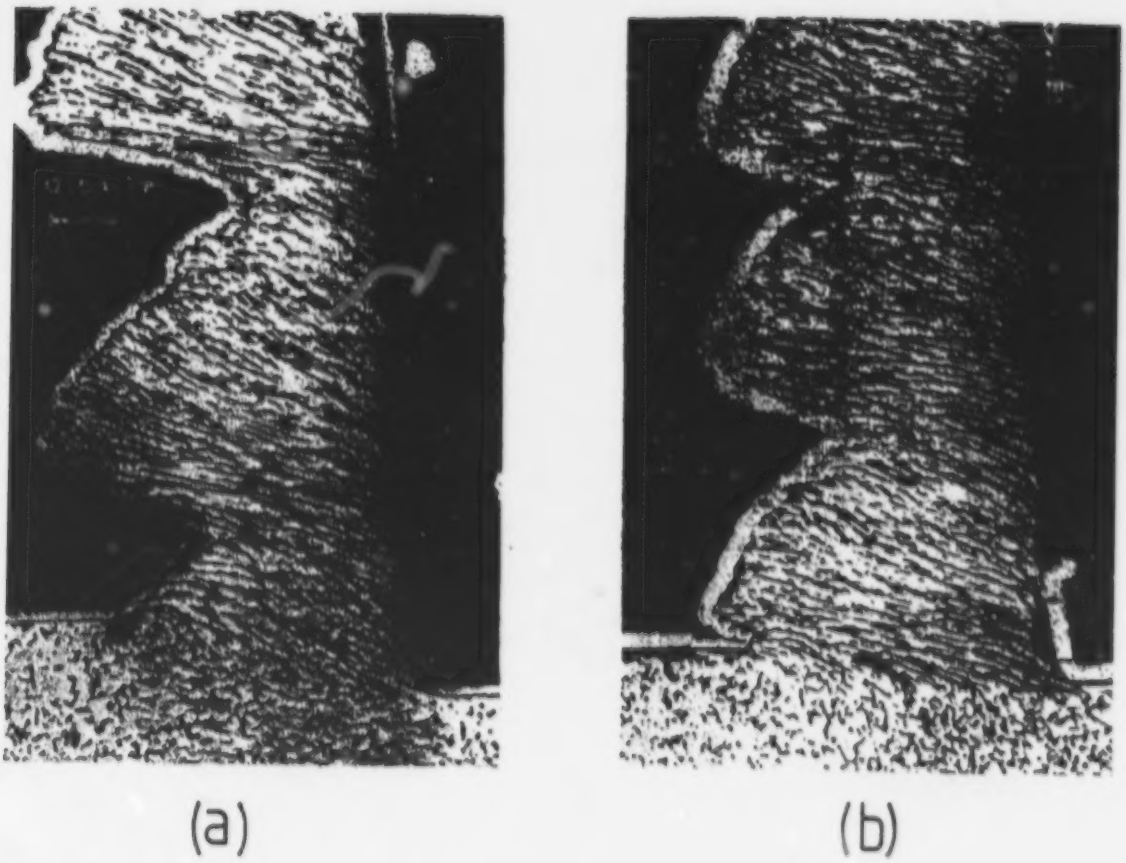

Figure 15: Micrograph of a serrated chip, reproduced from Ref.17. (a) Plastic deformation zone is moving forwards. (b) Plastic deformation zone is just returning backwards.

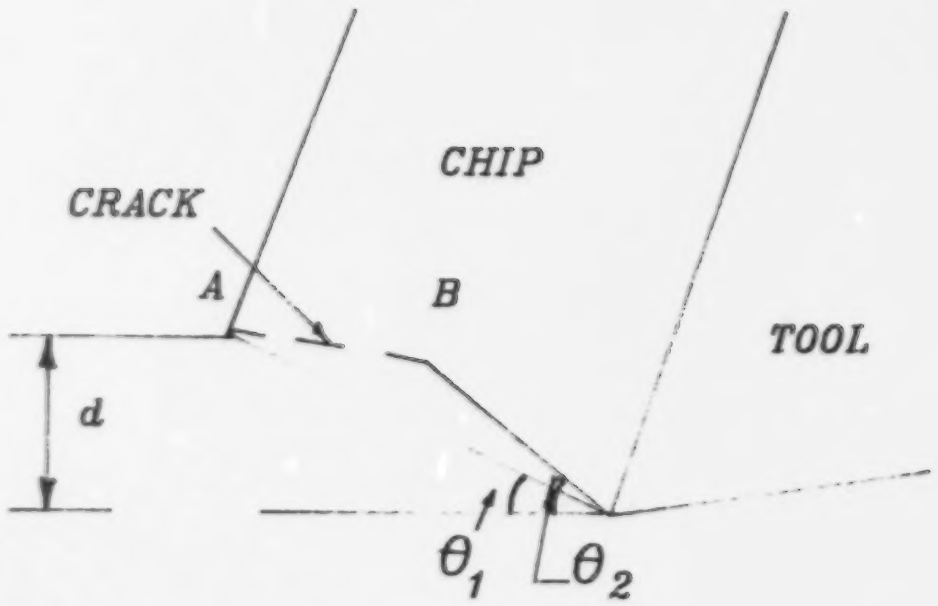

Figure 16: A model for discontinuous chip formation based on a single shear plane hypothesis.

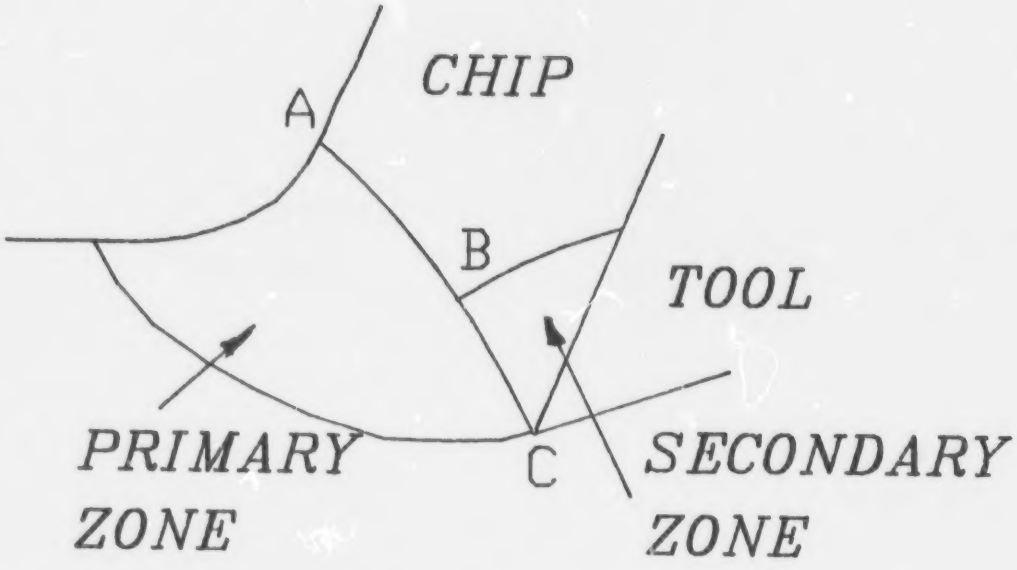

Figure 17: Sketch to depict the general shape of the plastic deformation zones in metal cutting.

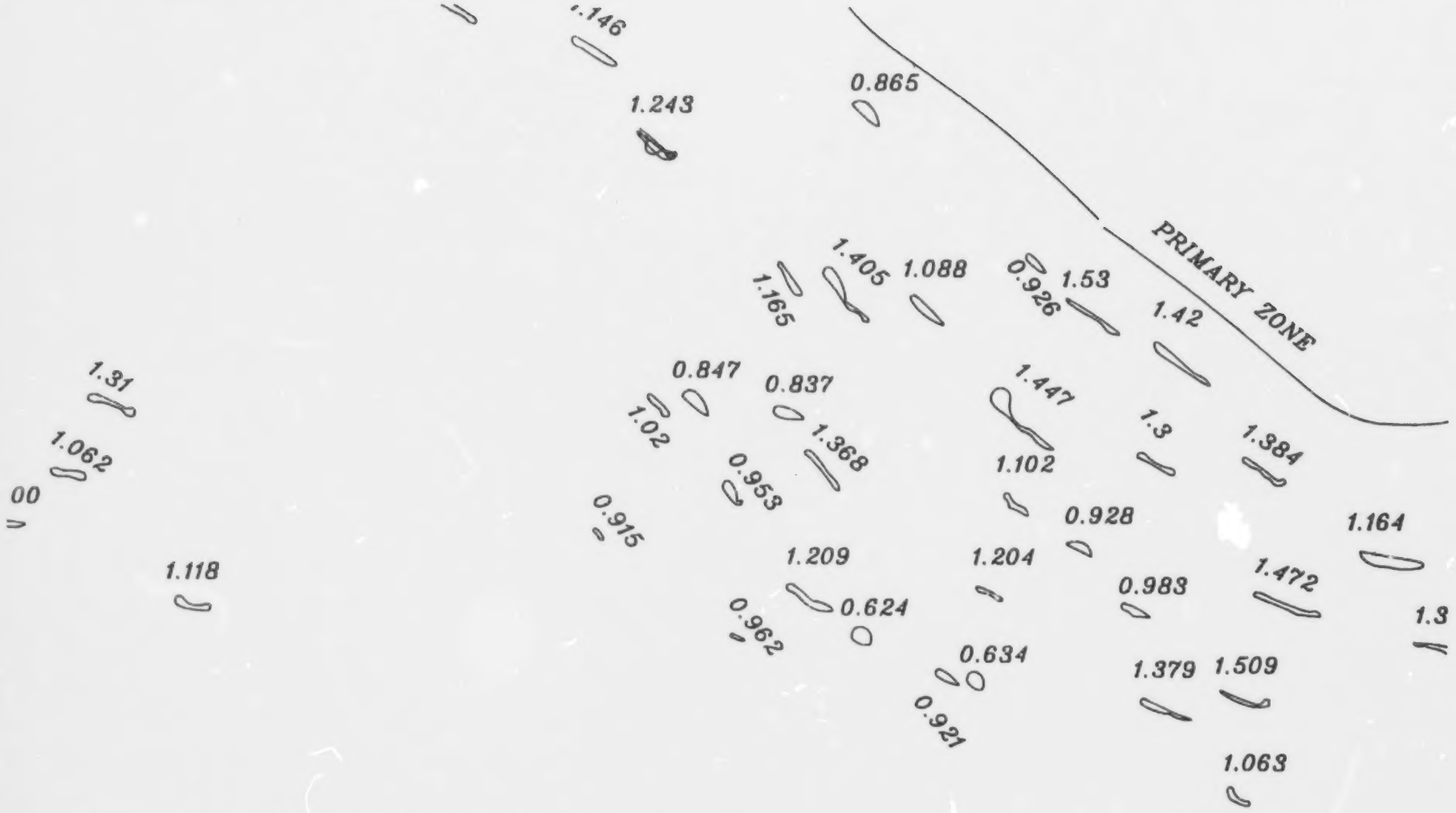

Figure 18: Finite strain measurements made from the plastic deformation of the carbide particles in the primary deformation zone. The values shown correspond to one of the principal directions. Material: AISI 1070 Steel.

SEM X 2500

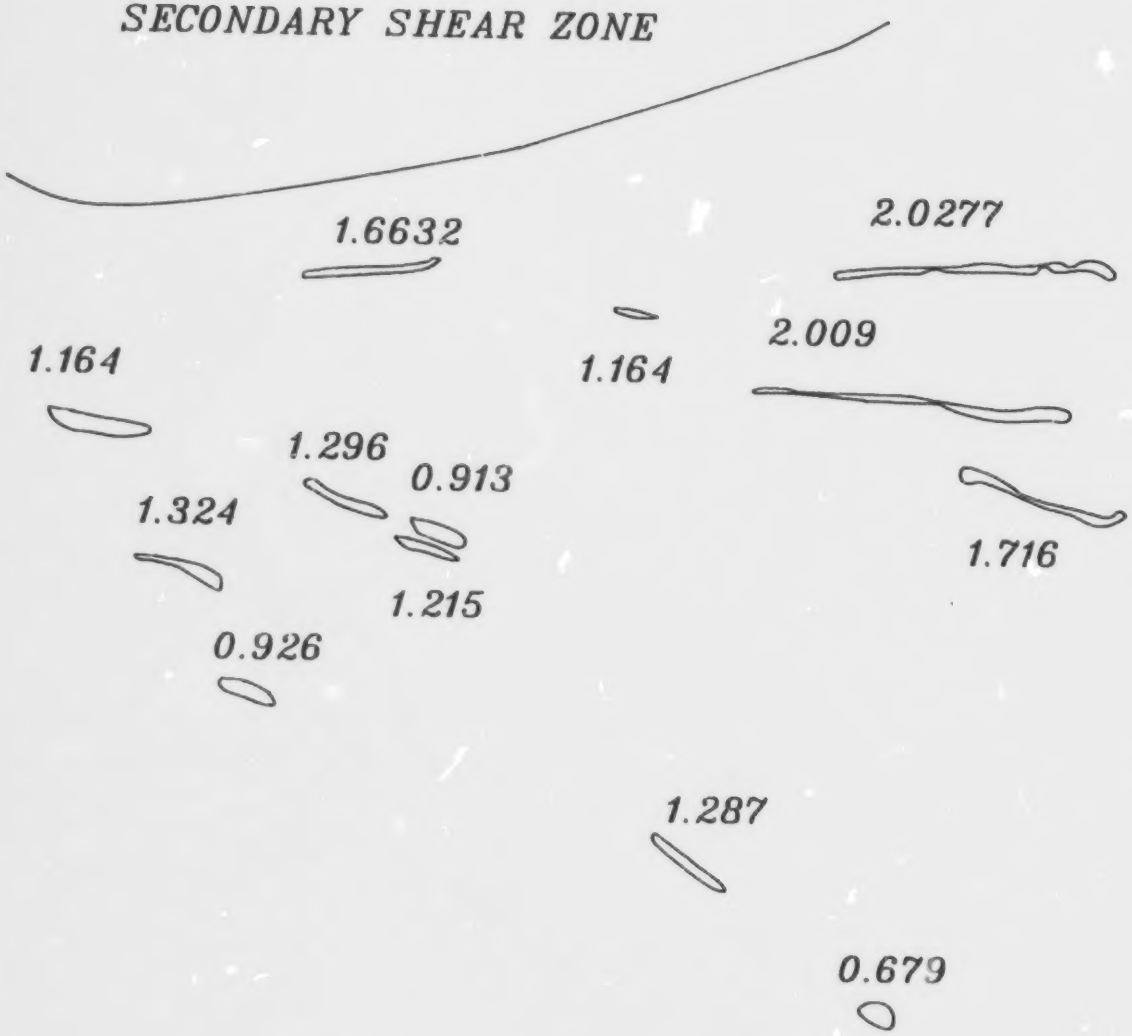

Figure 19: Same as above except that the deformation zone depicted is at the junction of secondary and primary zones.

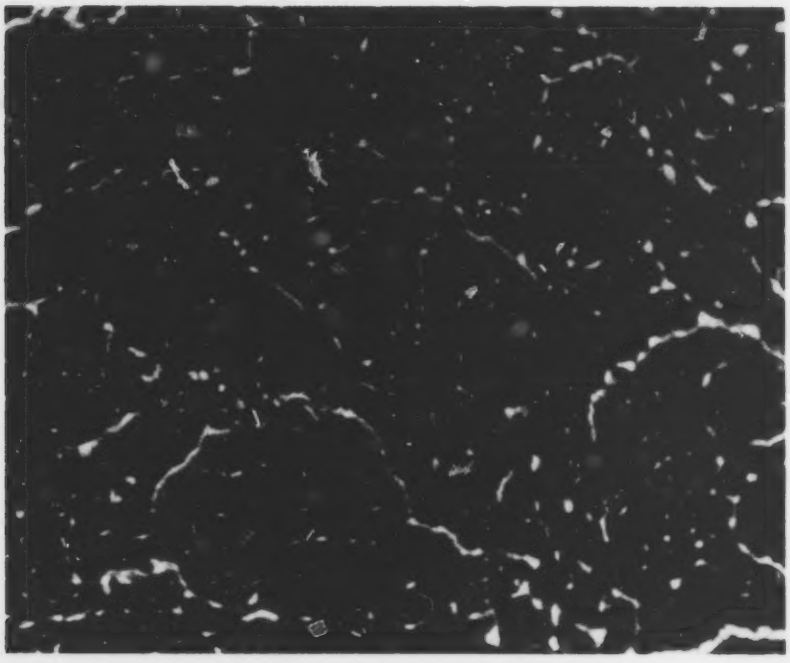

Figure 20: SEM pictures obtained from quick-stop experiments on AISI 4340 steel. Photographs show that the degree of deformation can be ascertained from the shape of the grain boundaries. The grain structures depicted are at the elastic-plastic boundary. X 2430.

Figure 21: Same as above except that the grain structures are at the junction of the primary and secondary zones.

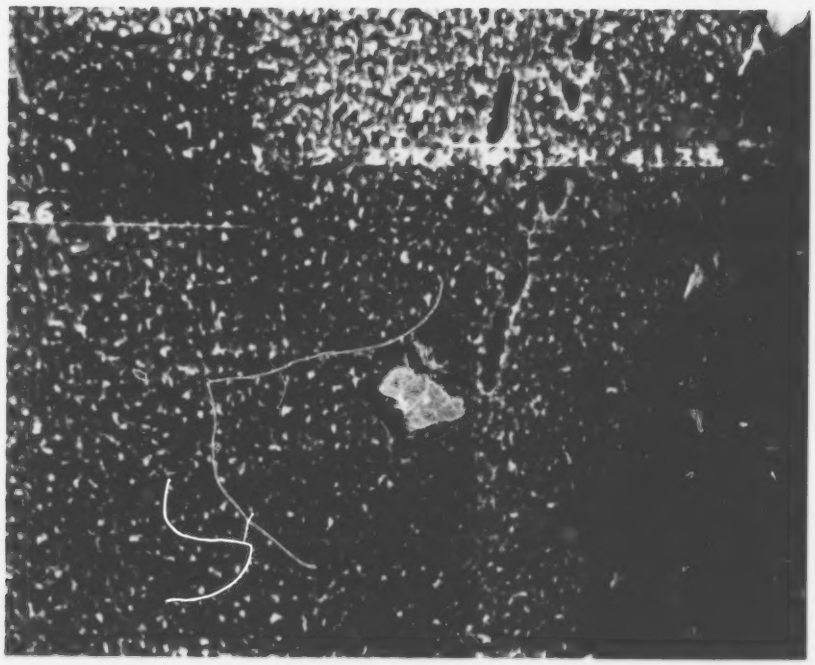

Figure 22: Same as Figures 20 and 21. The deformation of the material is near the rake face of the tool.

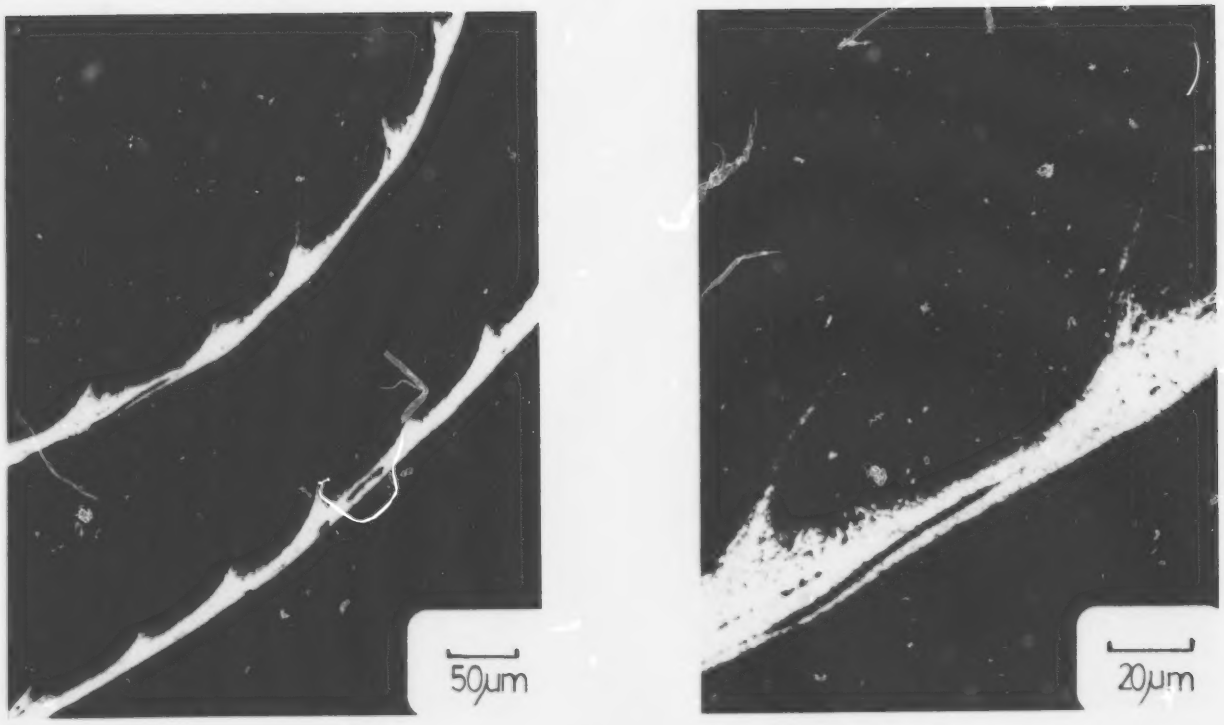

Figure 23: (a) Photomicrographs of discontinuous chips obtained from cutting tests carried out on two AISI 4340 steel specimens hardened to varying degrees. Hardness 52 Rockwell C.

(b)

Figure 23: (b) Photomicrographs of discontinuous chips obtained from cutting tests carried out on two AISI 4340 steel specimens hardened to varying degrees. Hardness 47 Rockwell C.

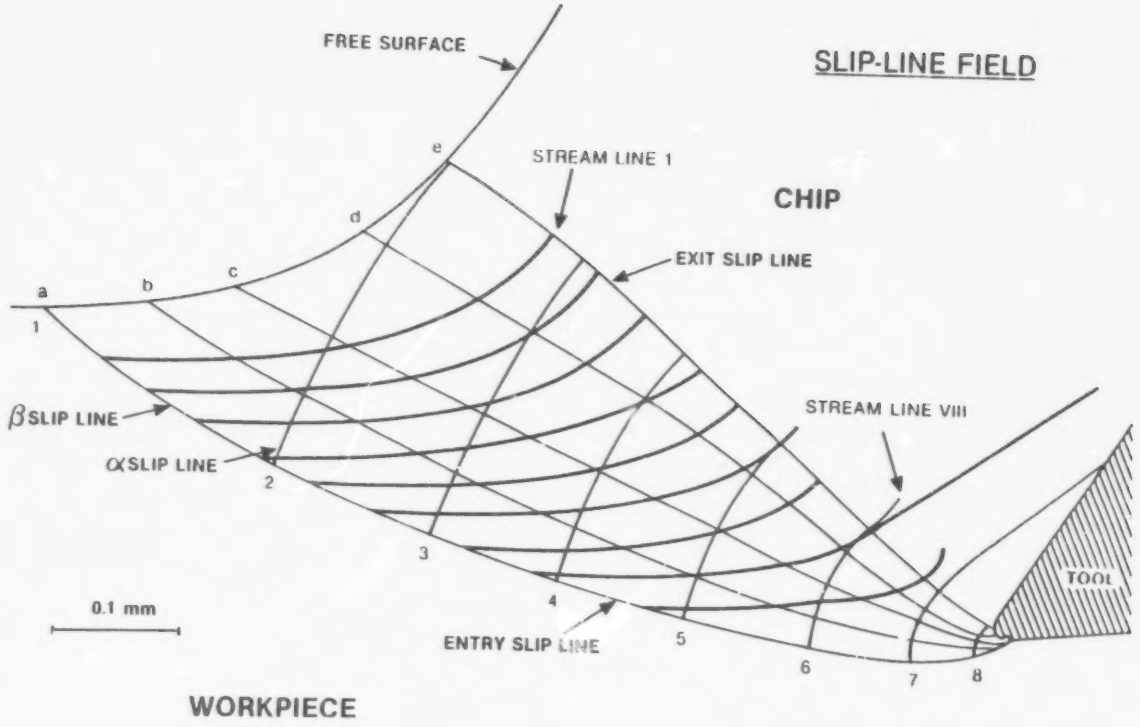

Figure 24: A slip-line field proposed by Roth and Oxley [4].

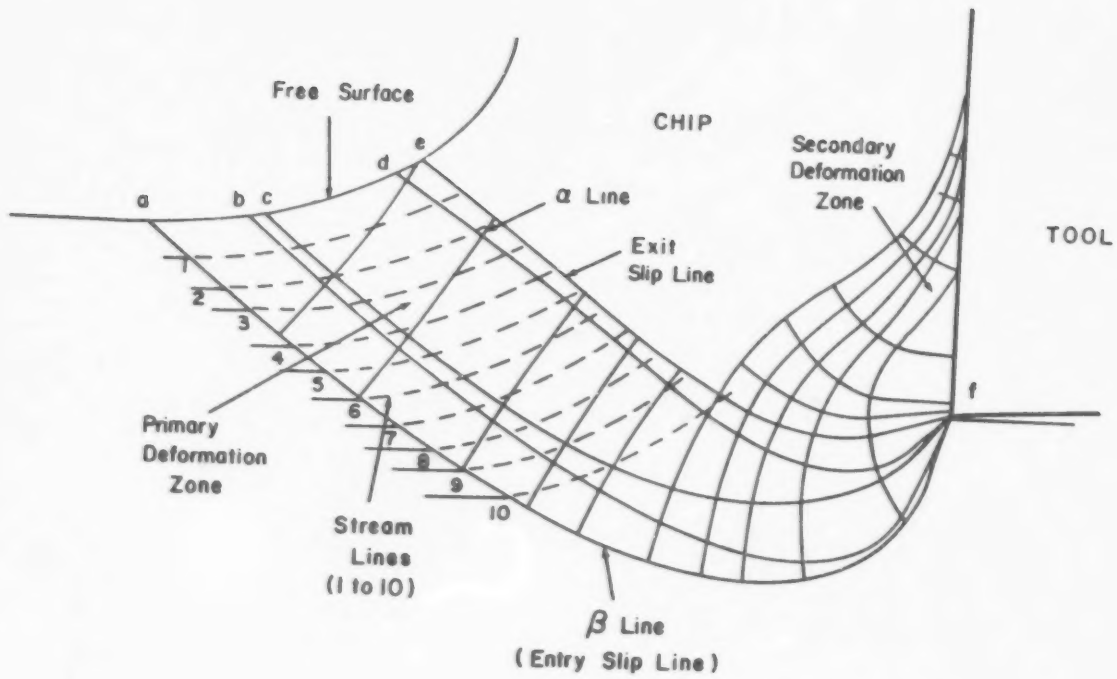

Figure 25: A slip-line field due to Sowerby and Chandrasekaran [25].

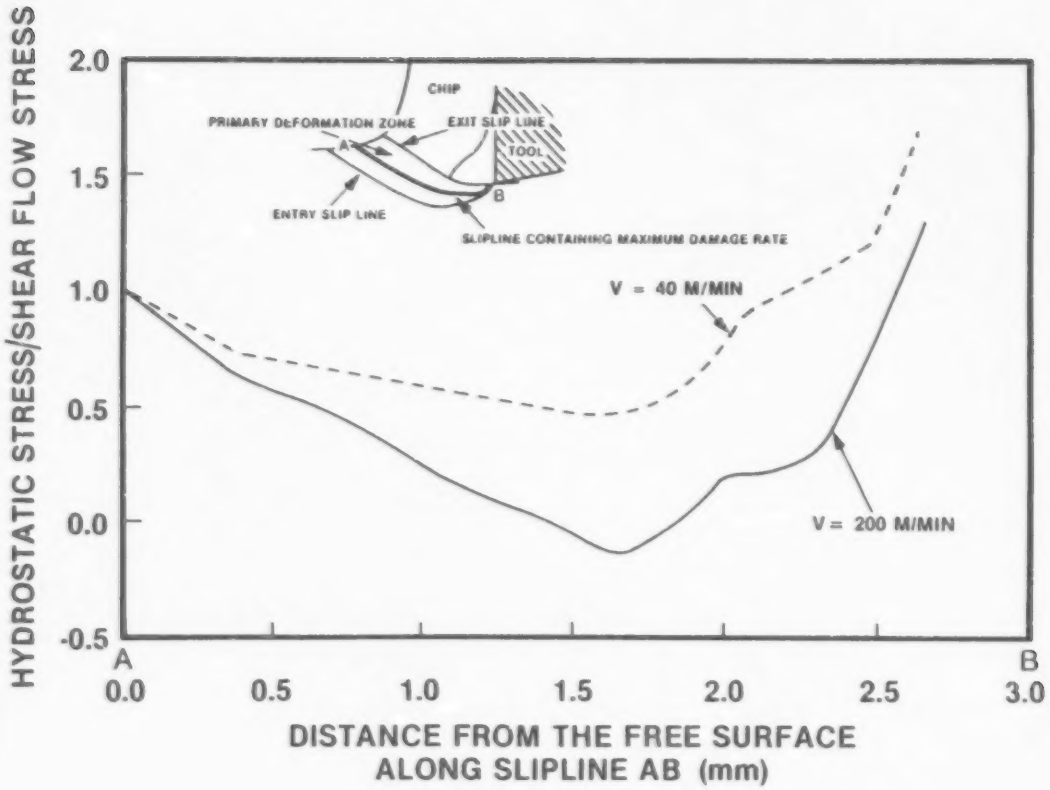

Figure 26: Variation on the hydrostatic stress/shear flow stress ratio vs. distance from the free surface of the chip towards the tool.

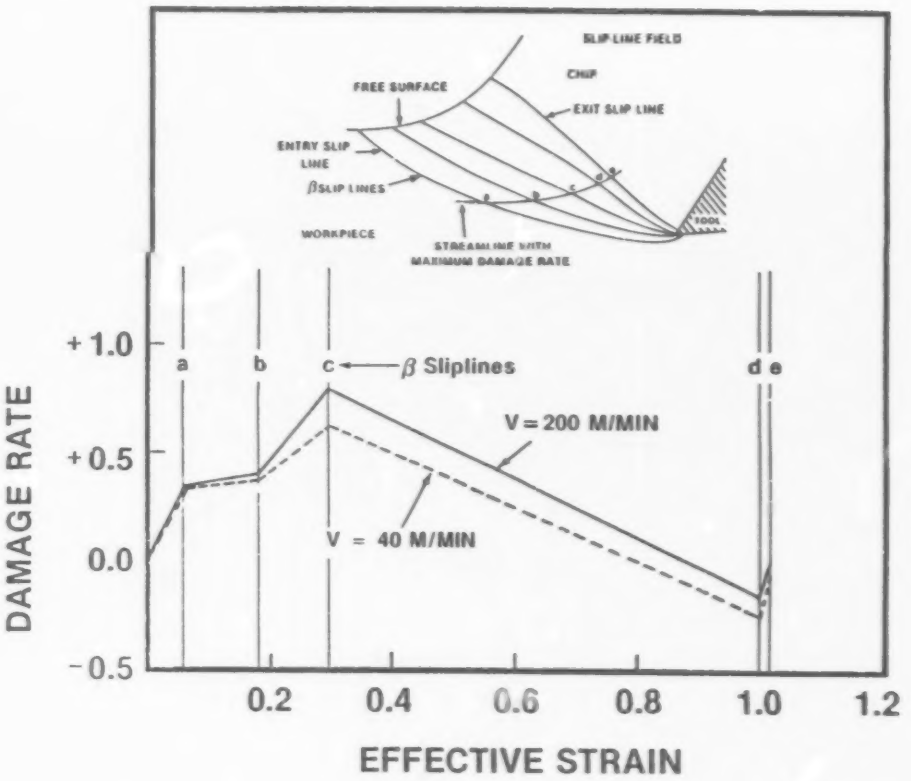

Figure 27: Streamline with "Maximum Damage Rate".

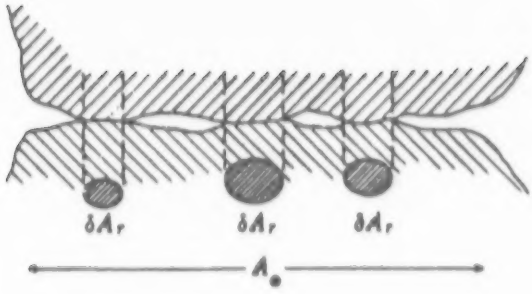

(a)

Figure 28: (a) Schematic representation of the contact between two rough surfaces. In the figure, Ar and Ao represent contact area of the junction and the total area of contact respectively.

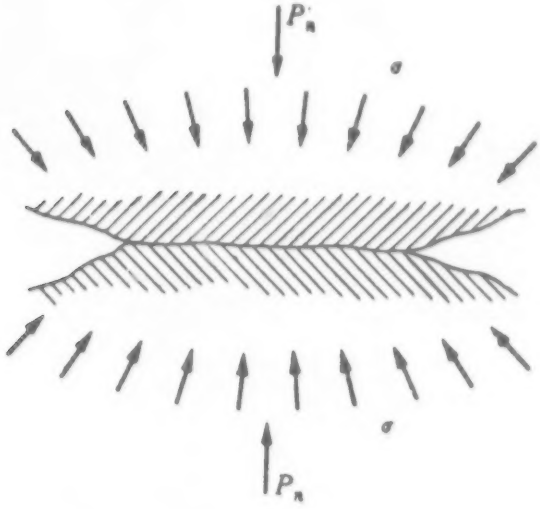

(b)

Figure 28: (b) Shows the close-up view of a junction.

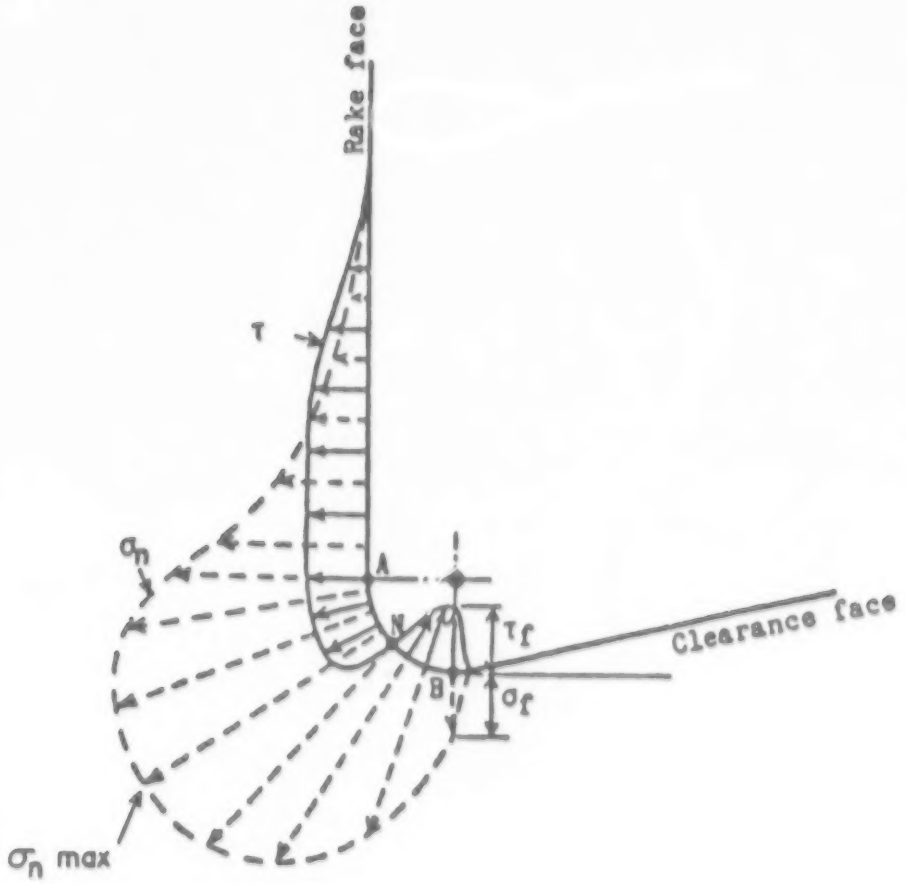

Figure 29: Stress distributions on the tool face in the vicinity of the cutting edge.

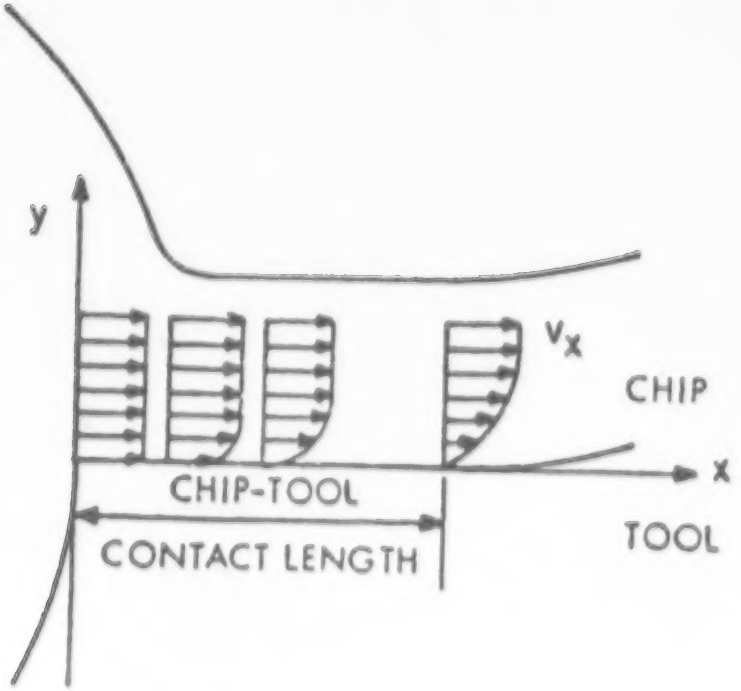

Figure 30: Schematic illustration of the chip flow geometry.

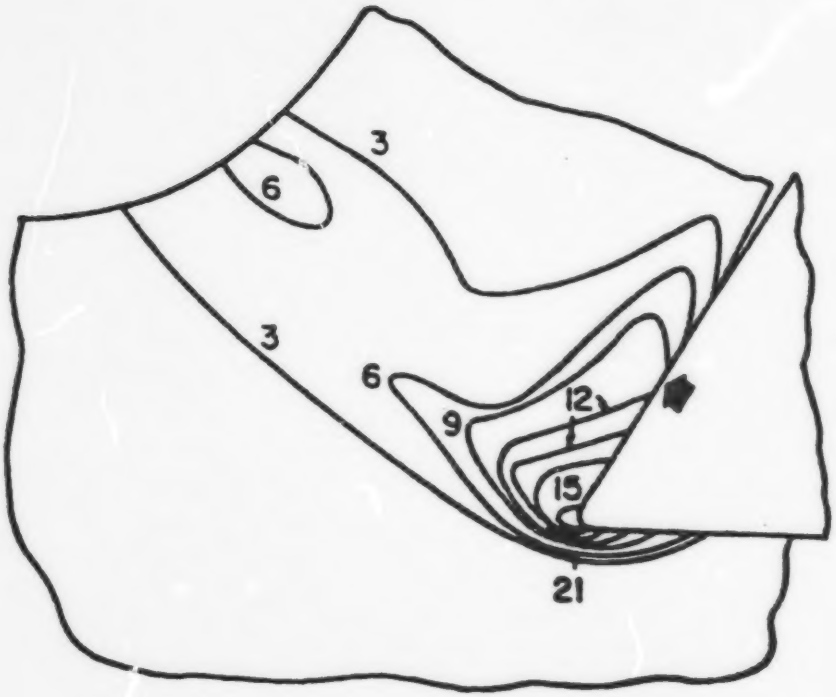

Figure 31: Temperature contours within the chip.

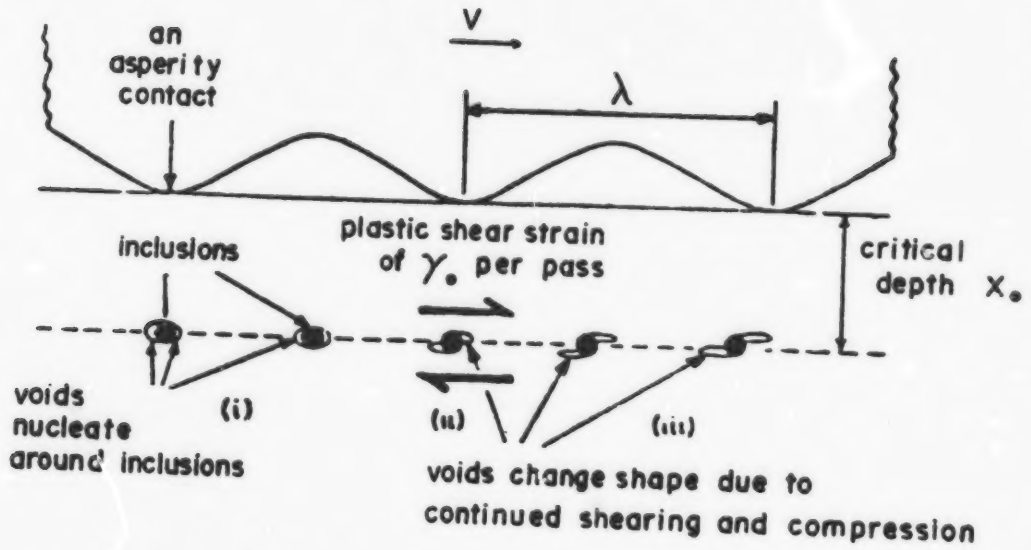

Figure 32: An idealised plasticity-dominated (delamination) wear model. Voids nucleate around the inclusions at a critical depth Xo under the influence of plastic shear strain (i): the continuous shearing action and compression cause the shape of the voids to change. (ii) and (iii); while the voids grow.

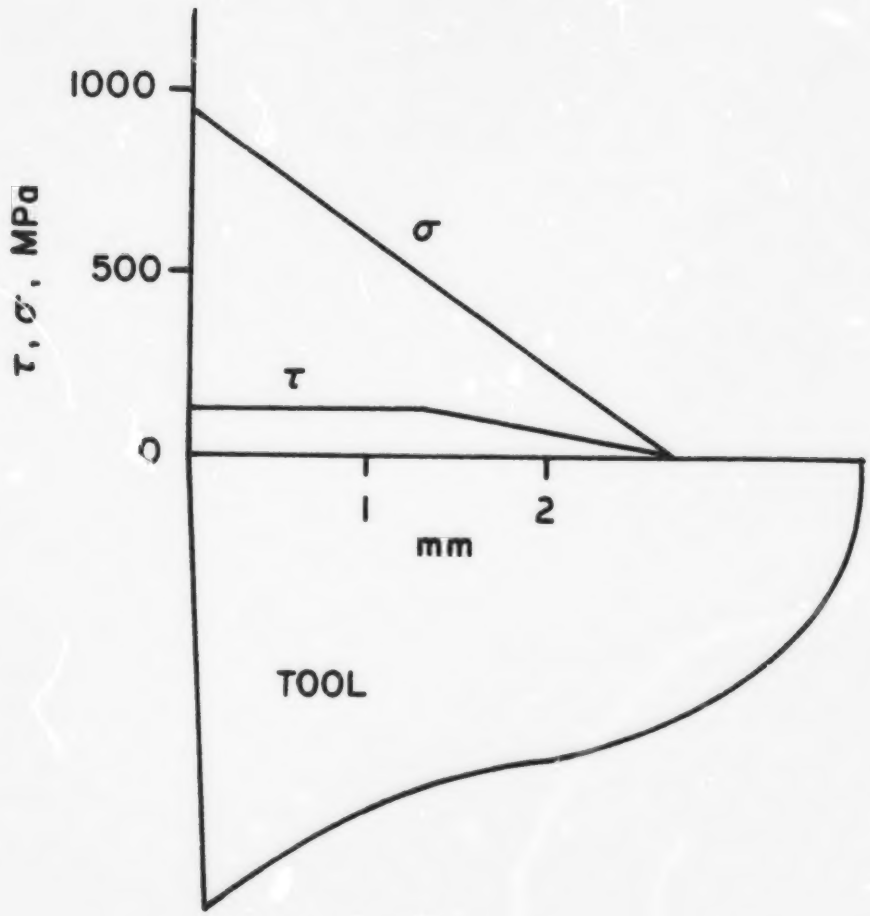

Figure 33: Stress distribution on the tool face(shown to scale) for a feed rate of 2.54 mm/rev.

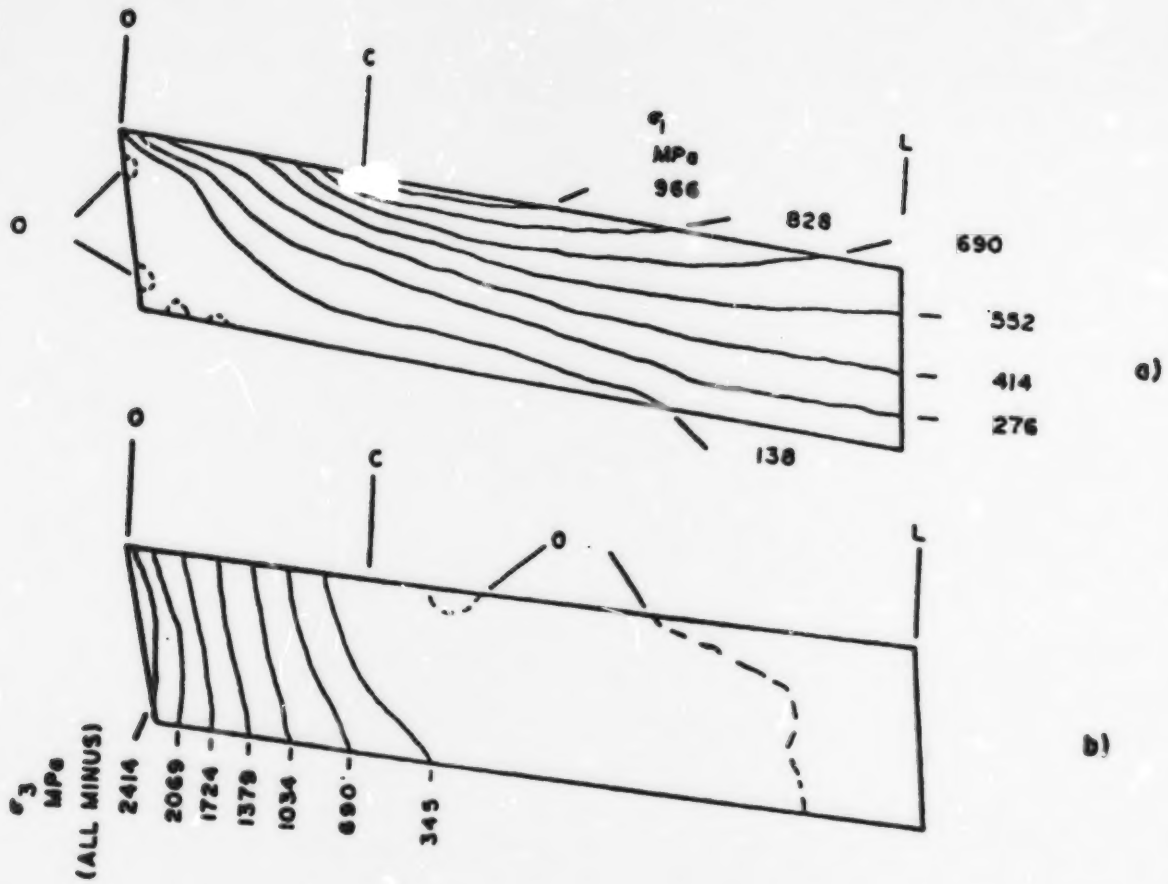

Figure 34: Principal stresses (a) 1 and (b) 3 in a tool loaded elastically. OC is the tool-chip contact length.

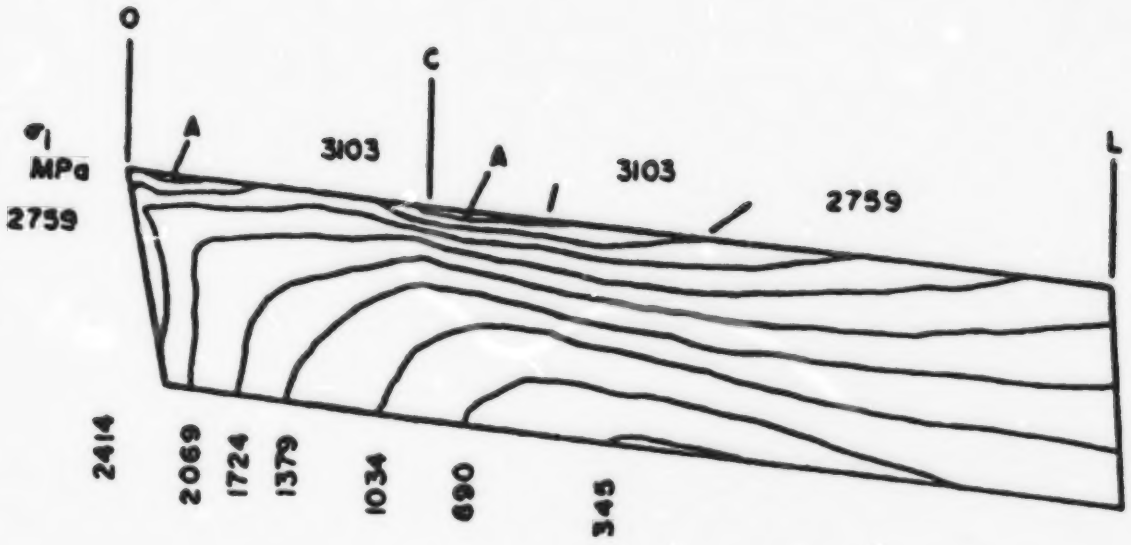

Figure 35: Intensified tensile stress (σ_1) distribution.

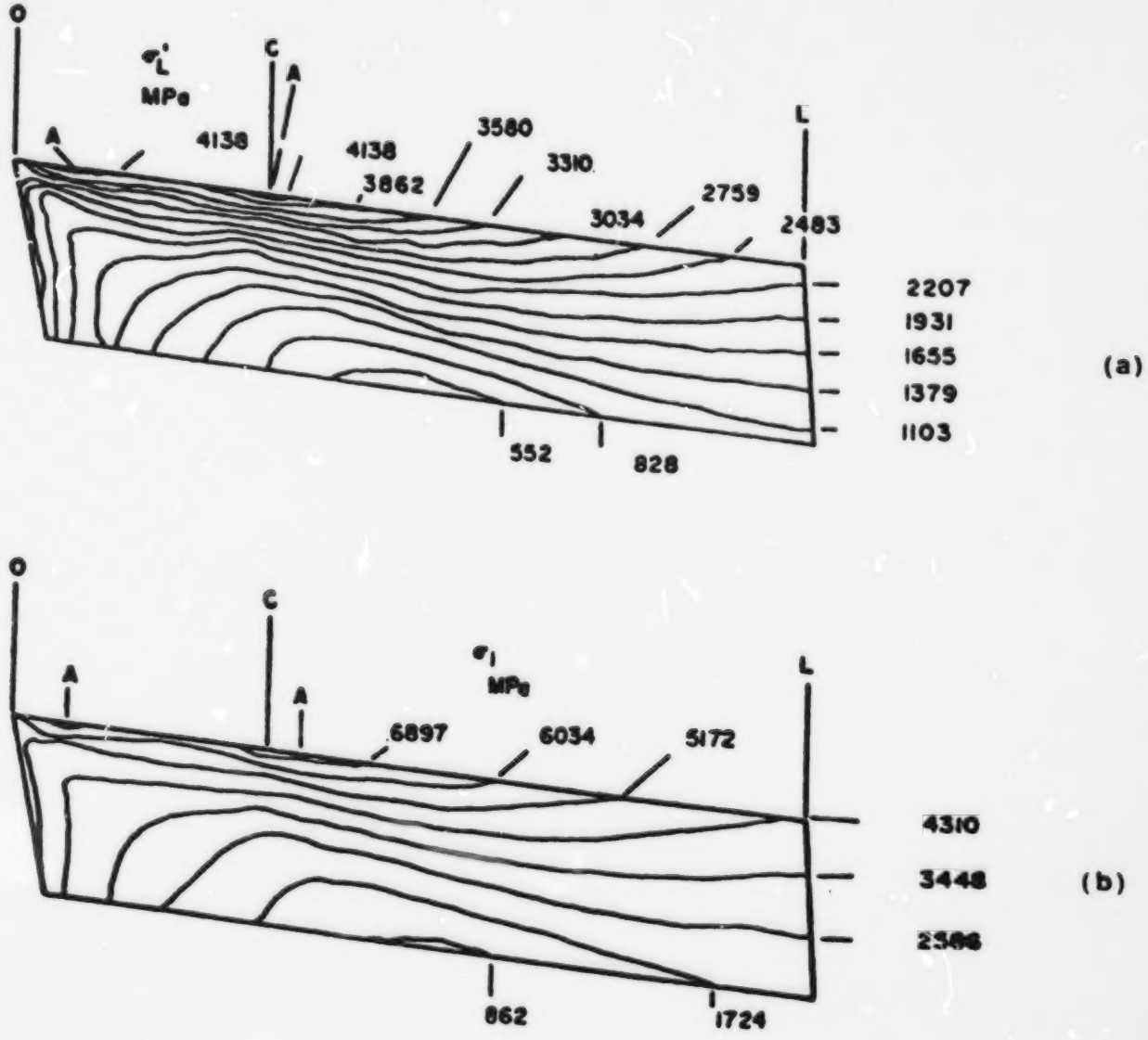

Figure 36: Intensified tensile stress (σ_1') distribution as in Fig. 8, except that for (a) FQ=0 and for (b) FP is twice as large.

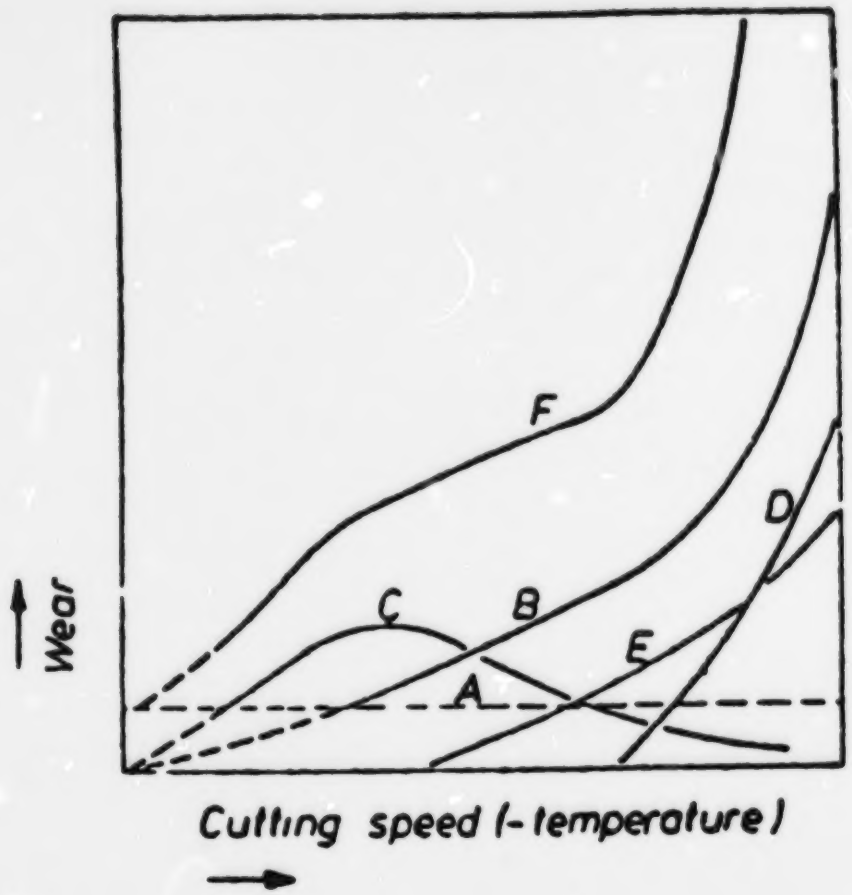

Figure 37: Four principal areas of wear (regions A to D) are identified schematically in the diagram of a worn coated tool.

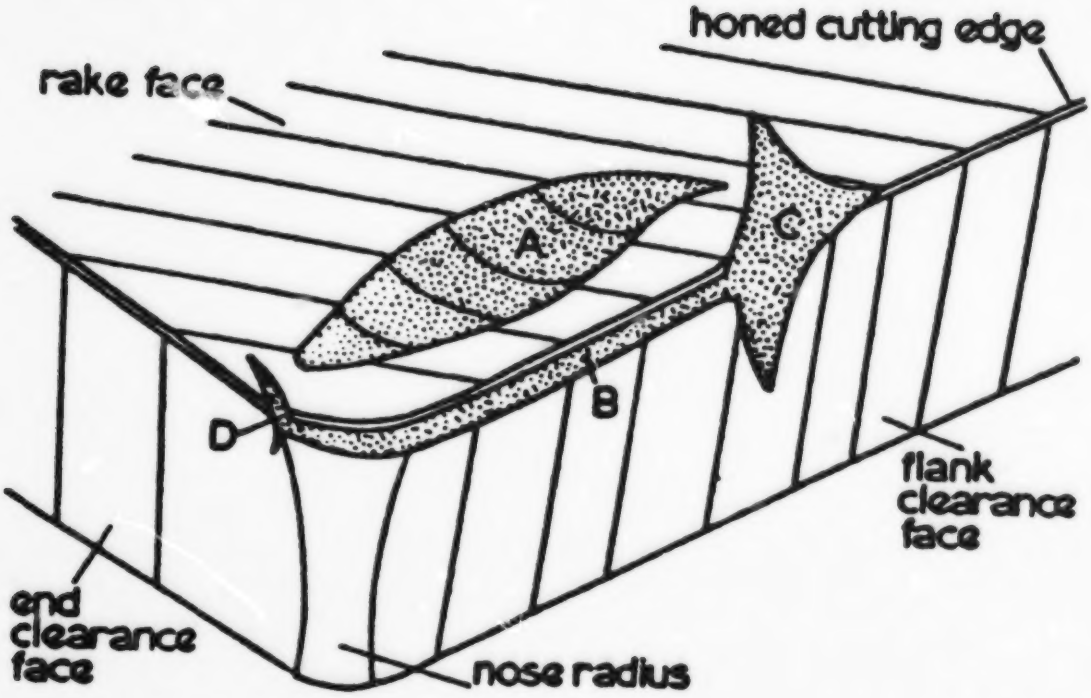

Figure 38: Development of flank wear on coated tools.

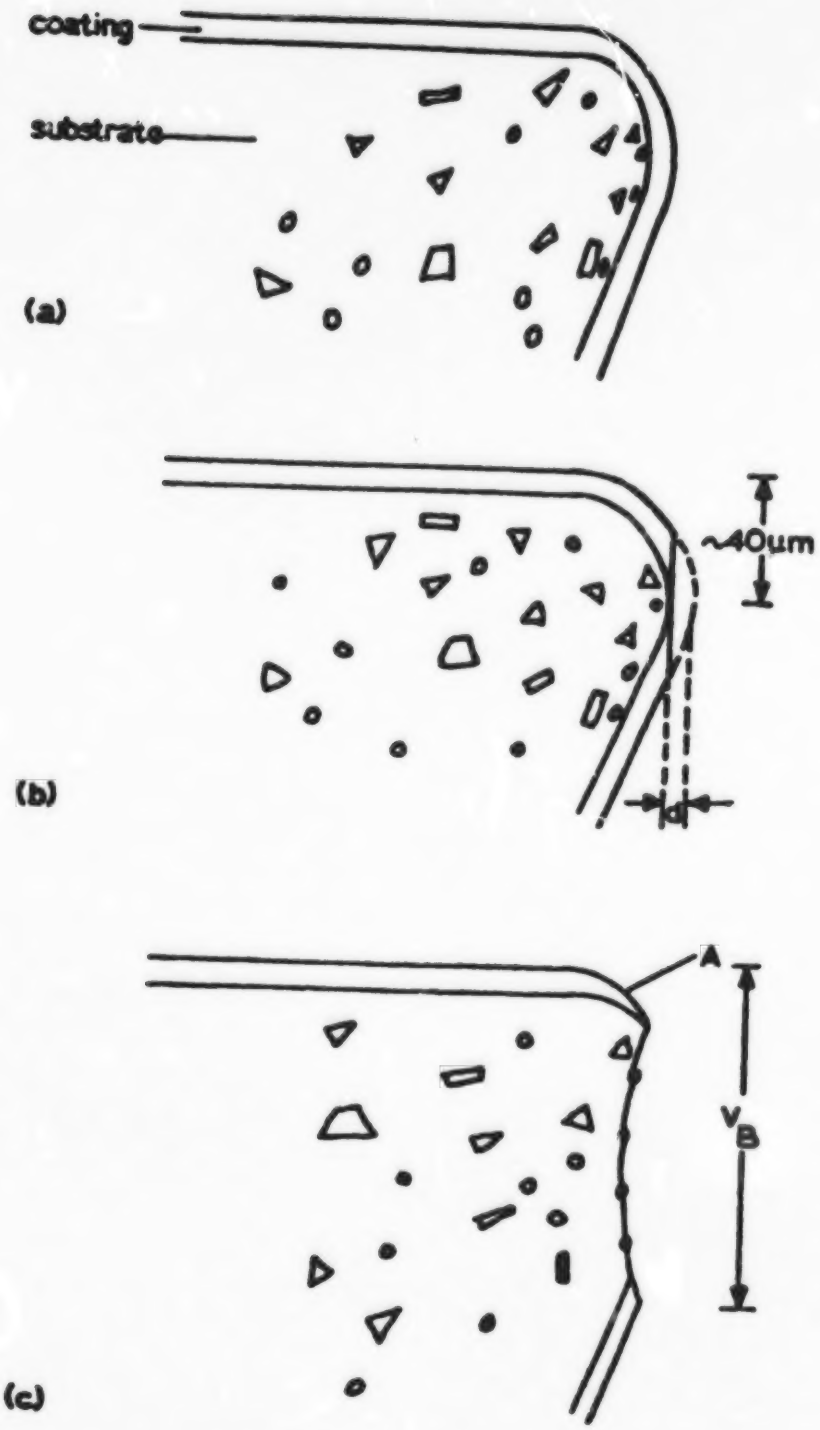

Figure 39: Development of rake-face wear on coated tools (a,b,c successive stages of wear).

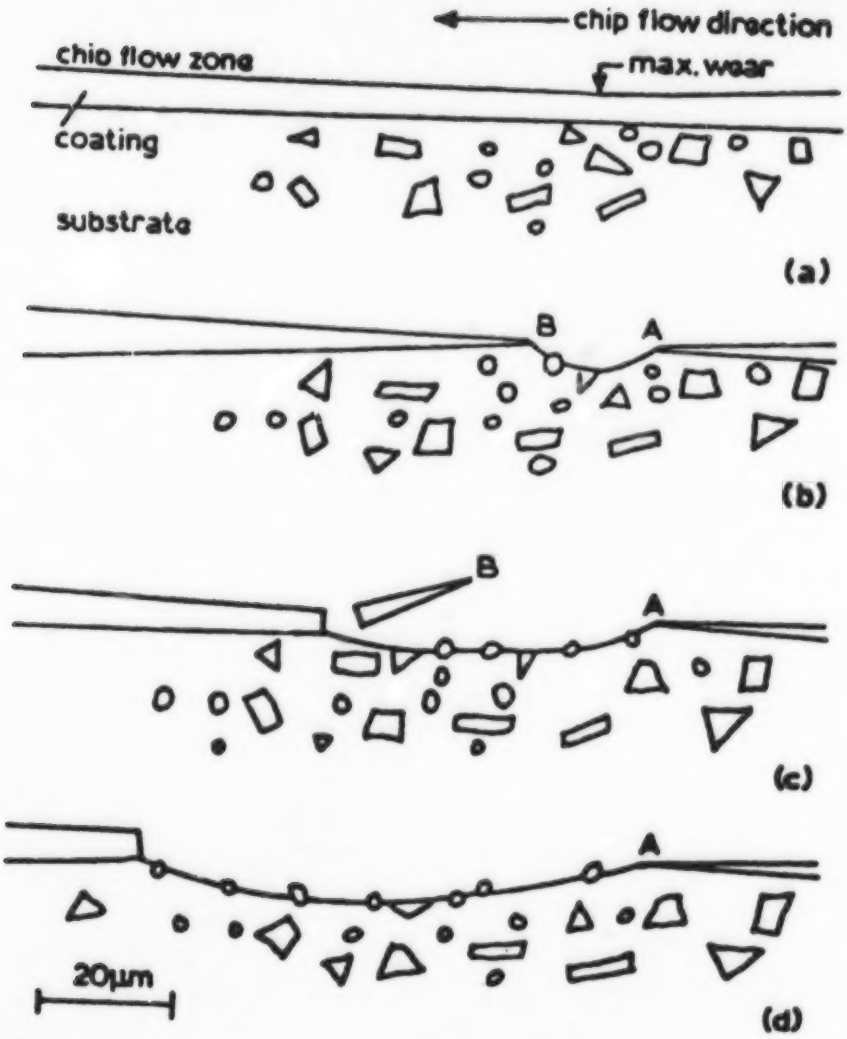

Figure 40: Schematic representation of wear as a function of cutting speed, see Ref. [38]. Initial edge wear, abrasion wear, tear-off due to galling, diffusion wear and scale wear are represented by curves A to E. F shows the general wear characteristics.

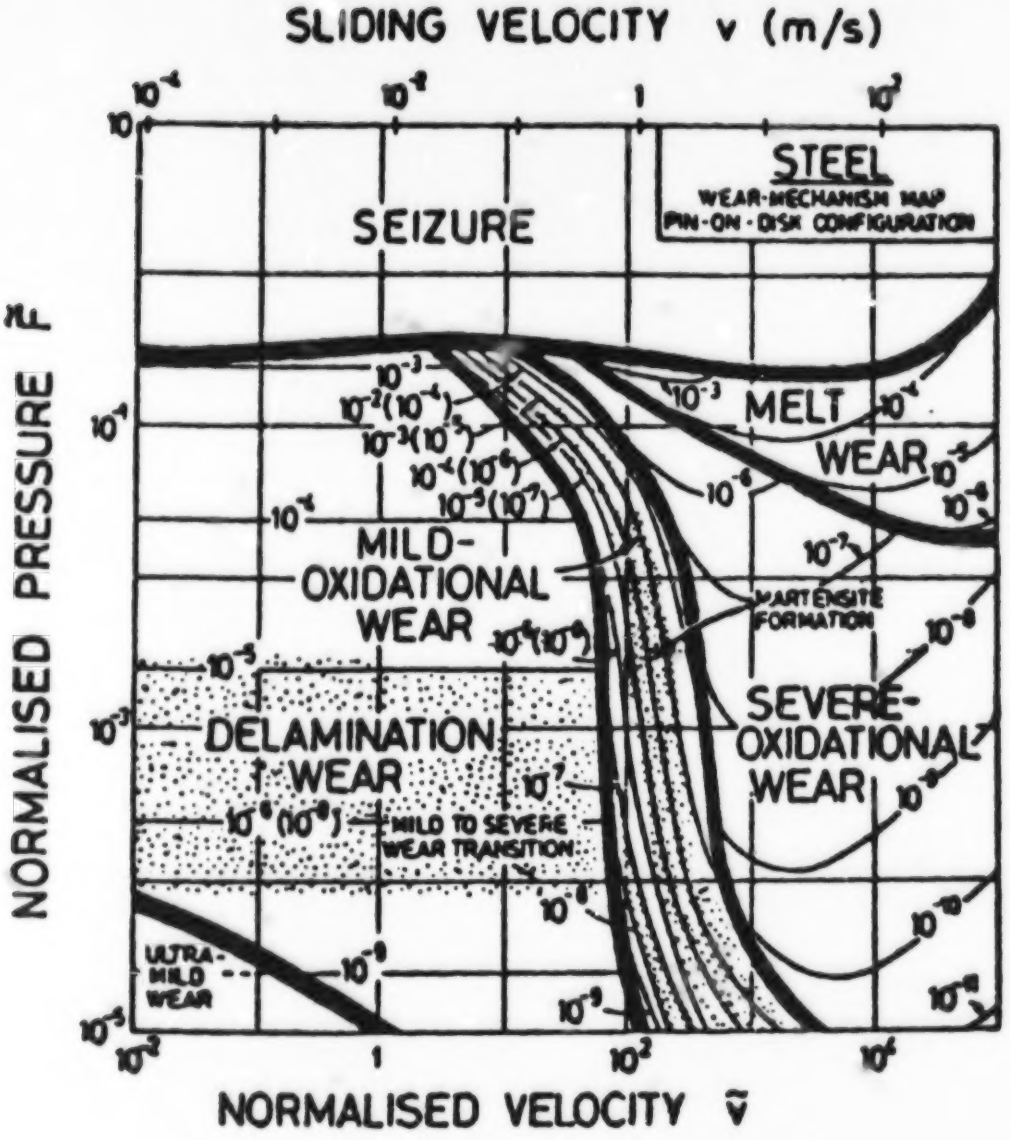

Figure 41: The wear-mechanism map. Normalised variables have been used.

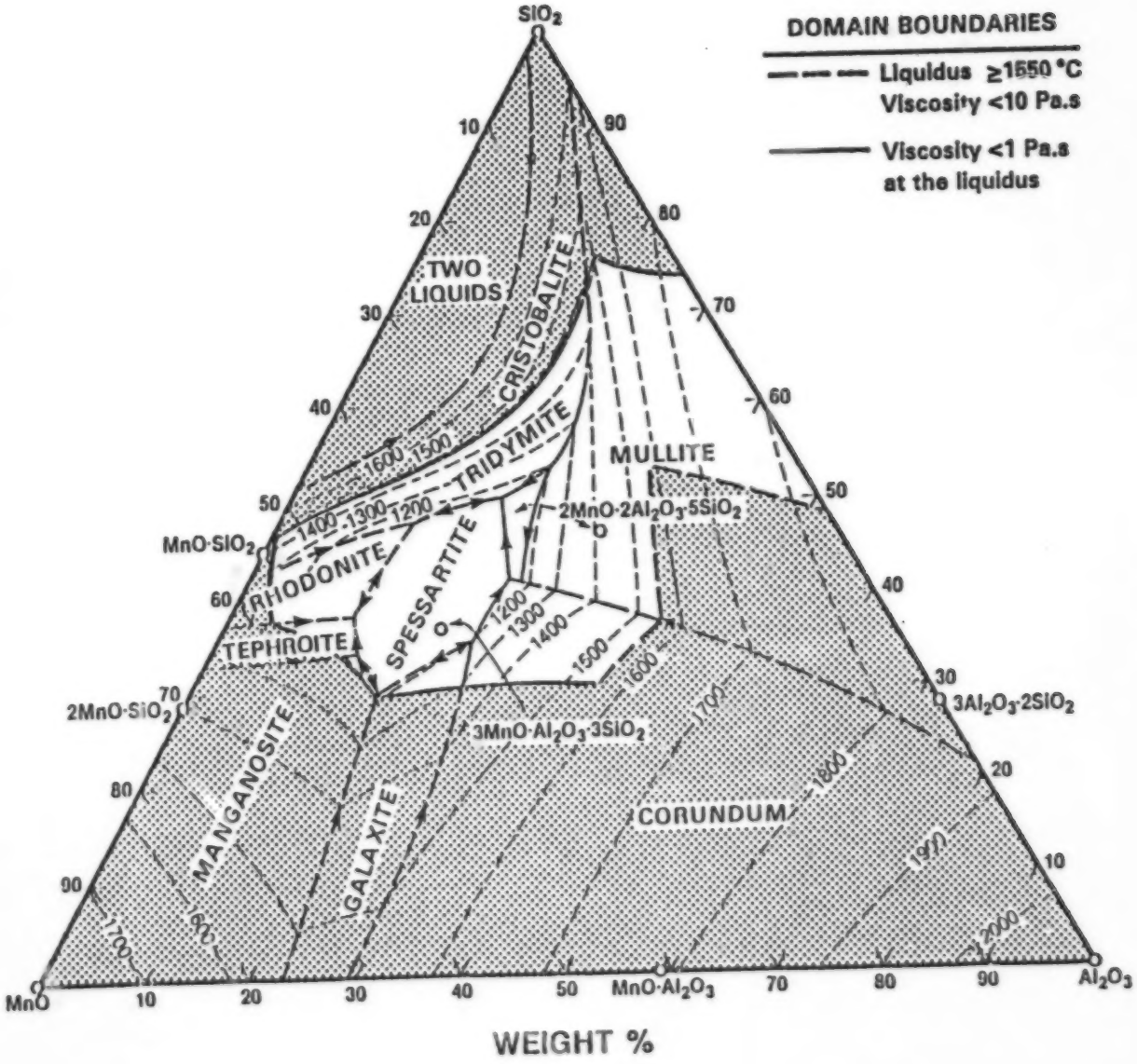

Figure 42: The MnO-SiO2-Al2O3 phase diagram giving the composition domains of "deformable" silicate inclusions[40].

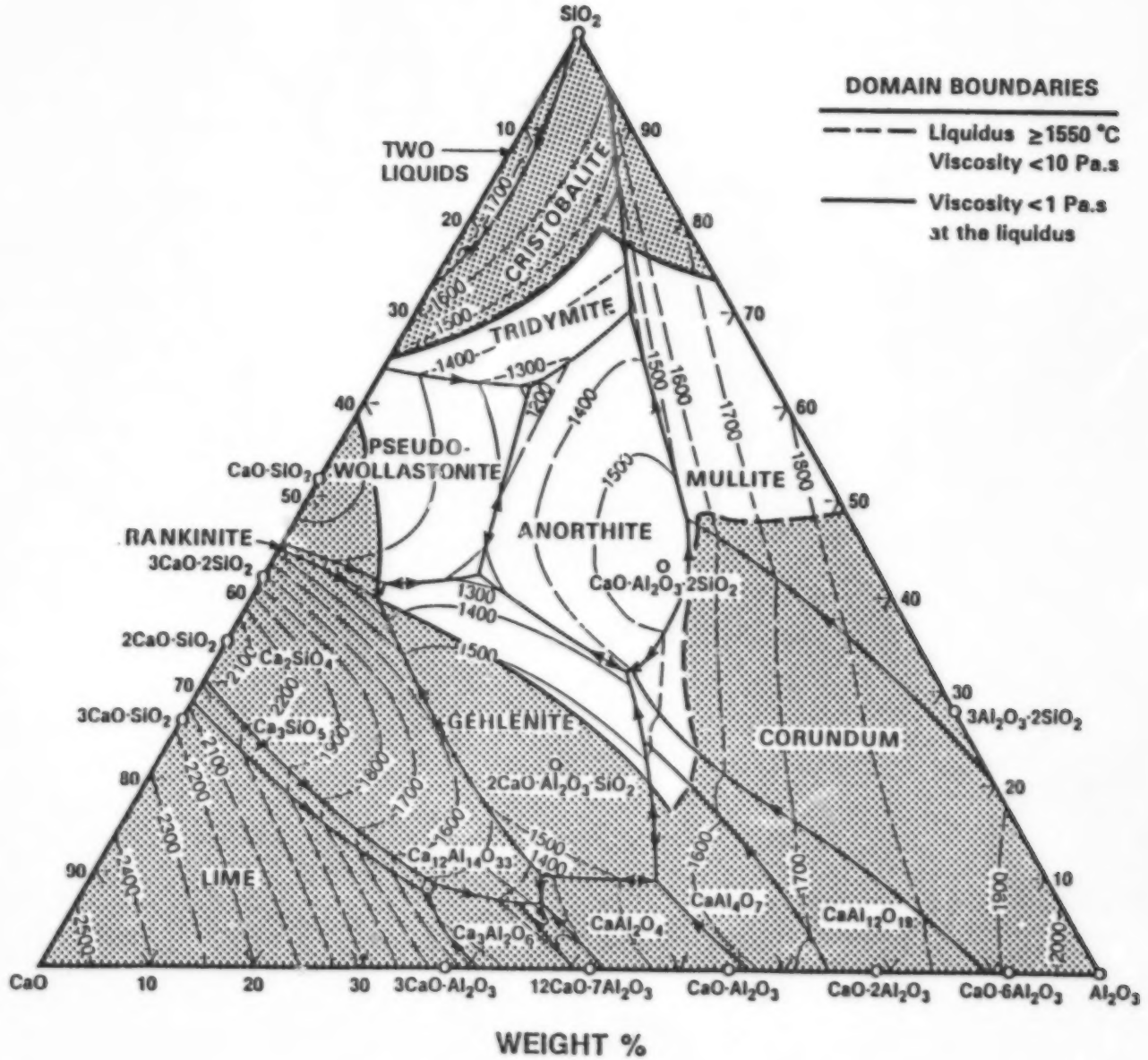

Figure 43: The CaO-Al2O3-Al2O3 phase diagram giving the composition domains of "deformable" silicate inclusions[40].

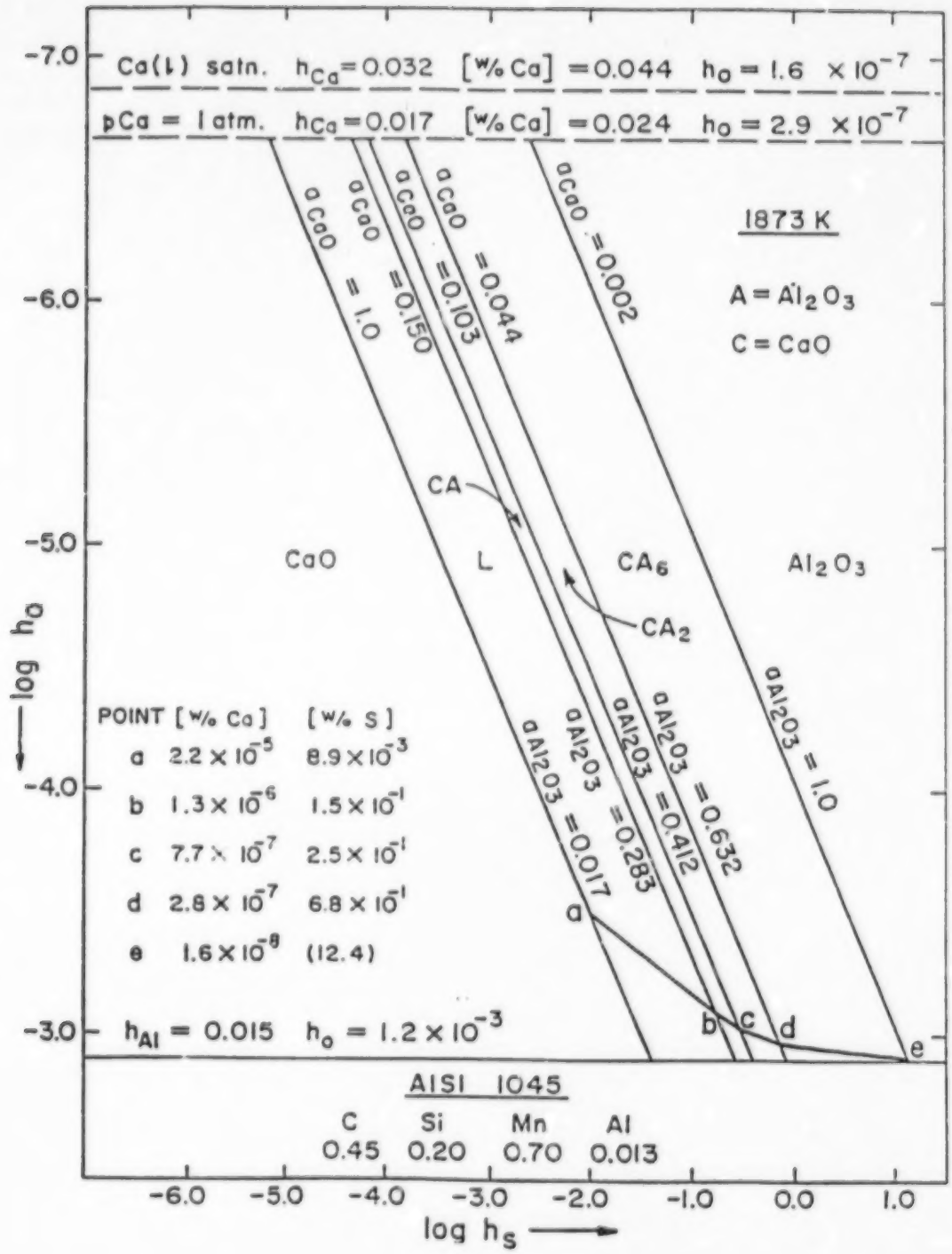

Figure 44: The Ca-Al-O-S phase stability diagram for an AISI 1045 steel at 1873 K. (h_{Al} =0.015)

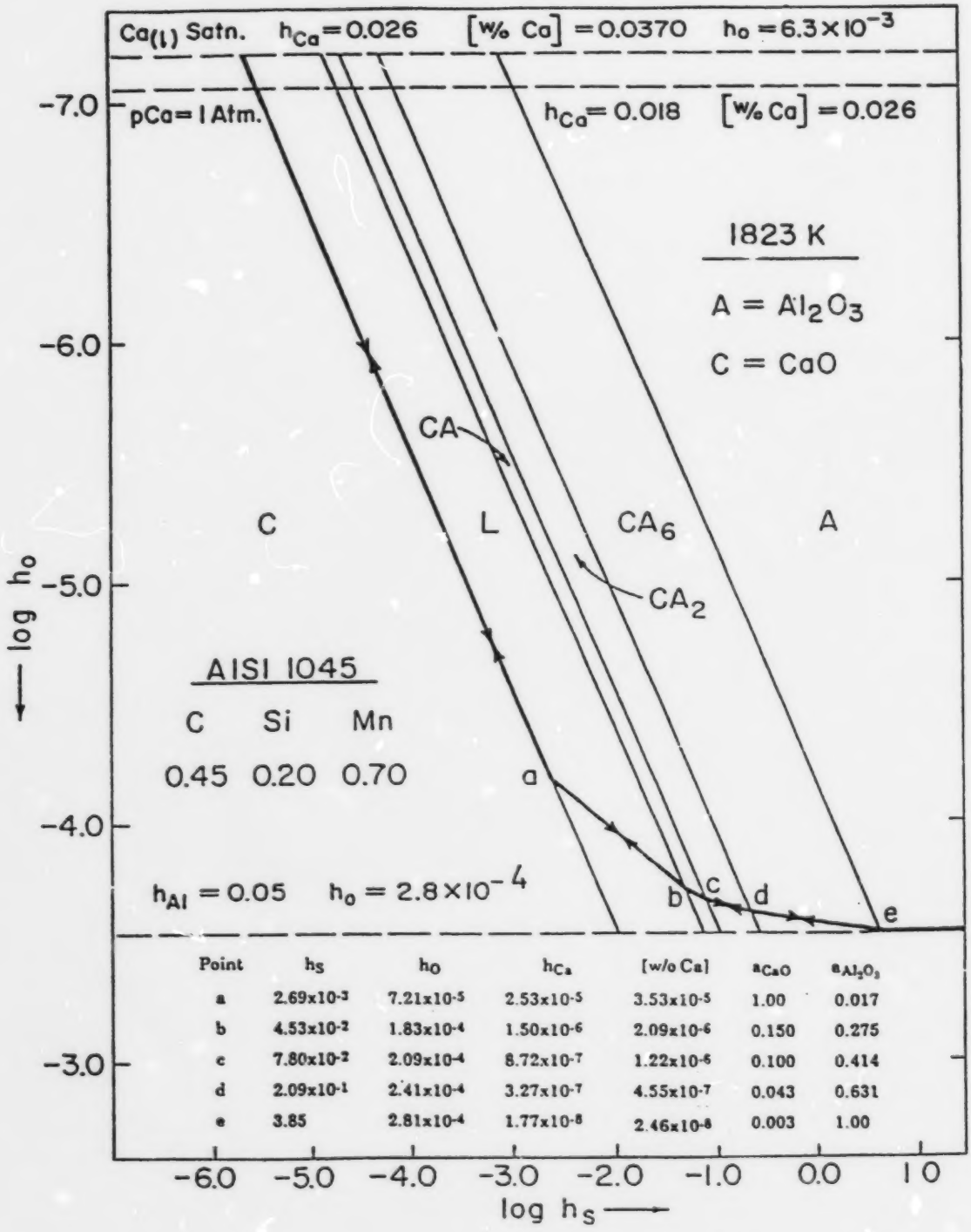

Point	h_S	h_O	h_{Ca}	[w/o Ca]	a_{CaO}	$a_{Al_2O_3}$
a	2.69x10^{-3}	7.21x10^{-5}	2.53x10^{-5}	3.53x10^{-5}	1.00	0.017
b	4.53x10^{-2}	1.83x10^{-4}	1.50x10^{-6}	2.09x10^{-6}	0.150	0.275
c	7.80x10^{-2}	2.09x10^{-4}	8.72x10^{-7}	1.22x10^{-6}	0.100	0.414
d	2.09x10^{-1}	2.41x10^{-4}	3.27x10^{-7}	4.55x10^{-7}	0.043	0.631
e	3.85	2.81x10^{-4}	1.77x10^{-8}	2.46x10^{-8}	0.003	1.00

Figure 45: The Ca-Al-O-S phase stability diagram for an AISI 1045 steel at 1823 K (h_{Al} =0.05).

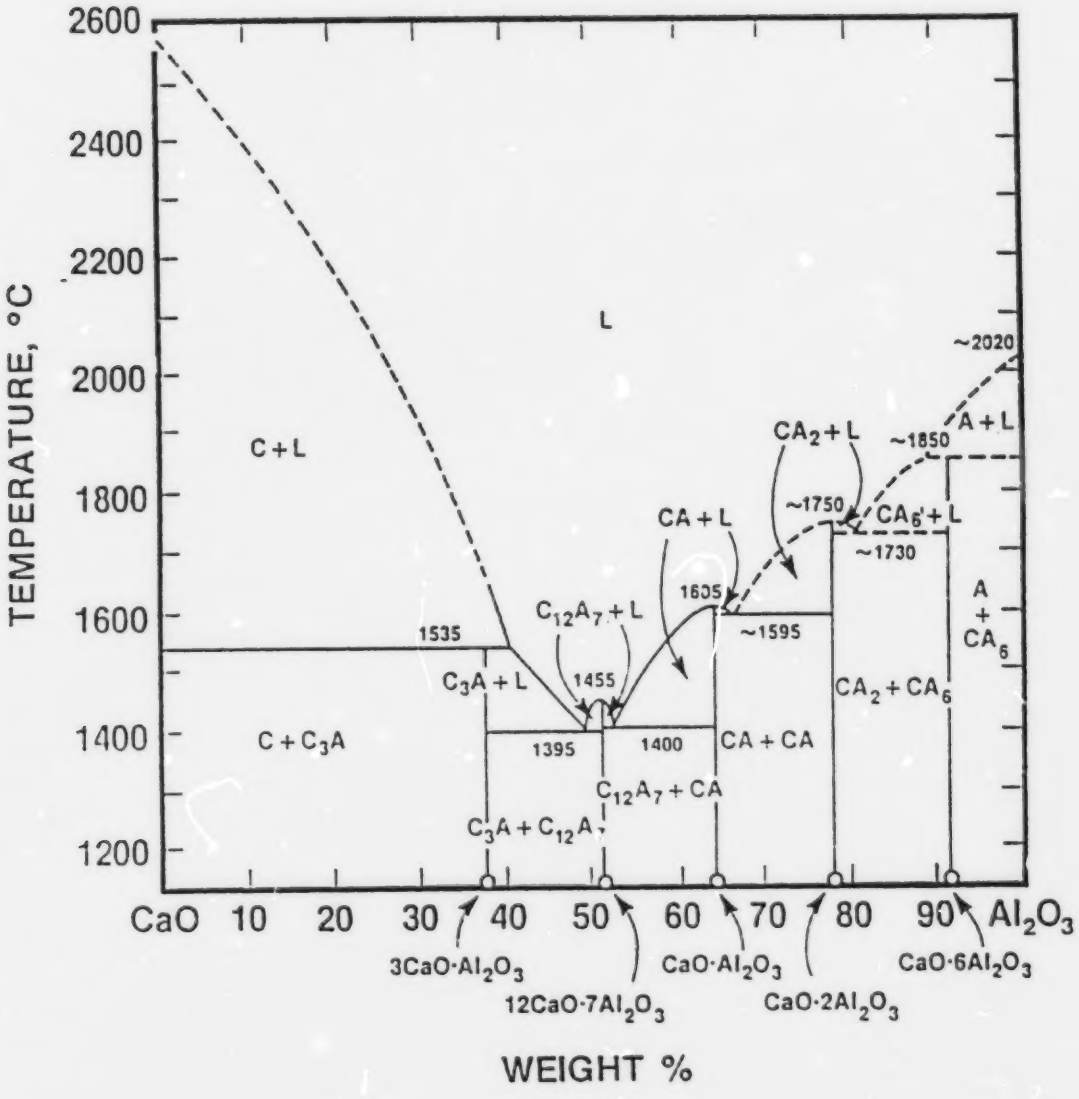

Figure 46: The CaO-Al2O3 system.

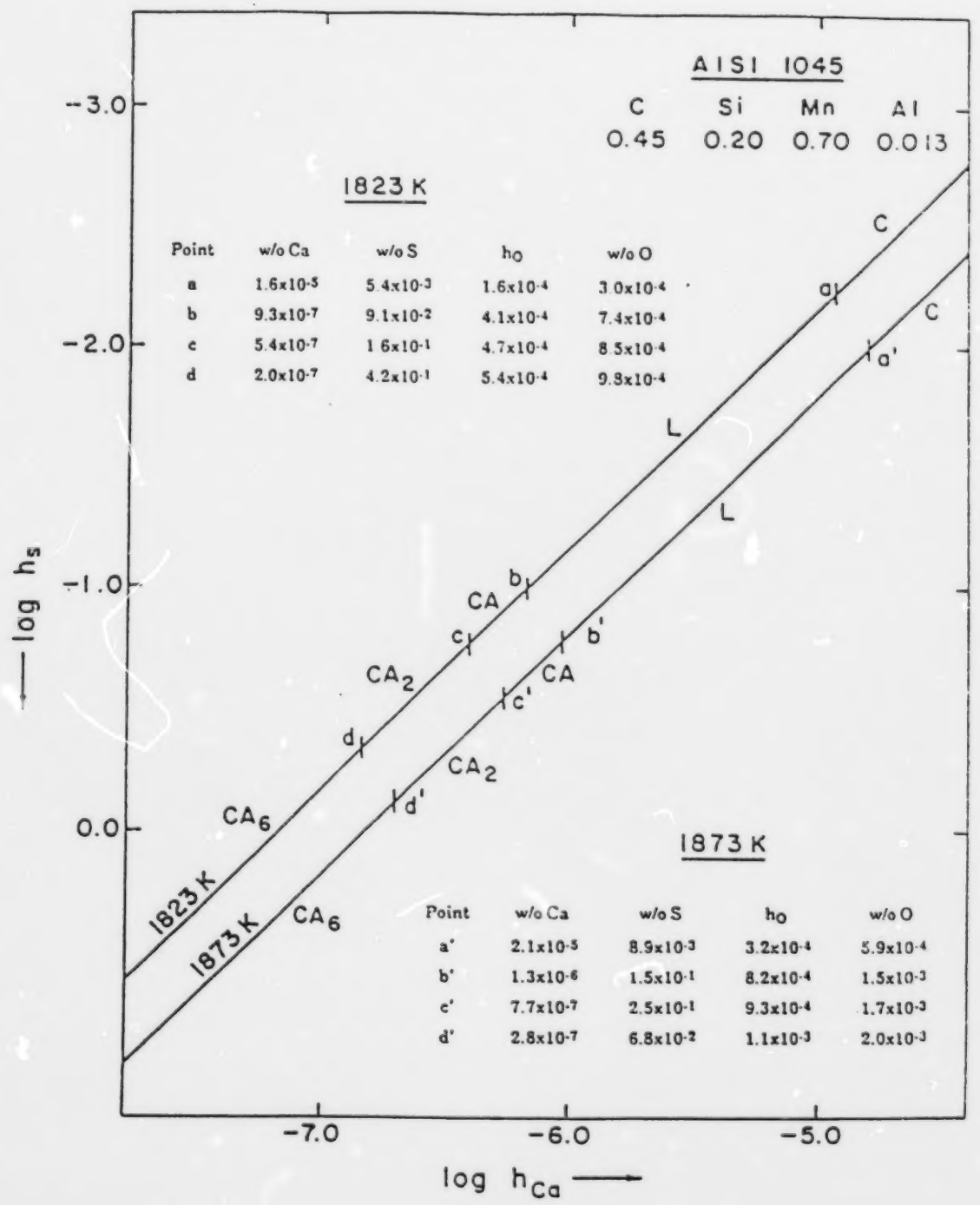

Figure 47: The conditions for coexistencies in the CaO-Al_2O_3 system at 1823 K and 1873 K for which log h_{Ca} is plotted as a function of log h_S.

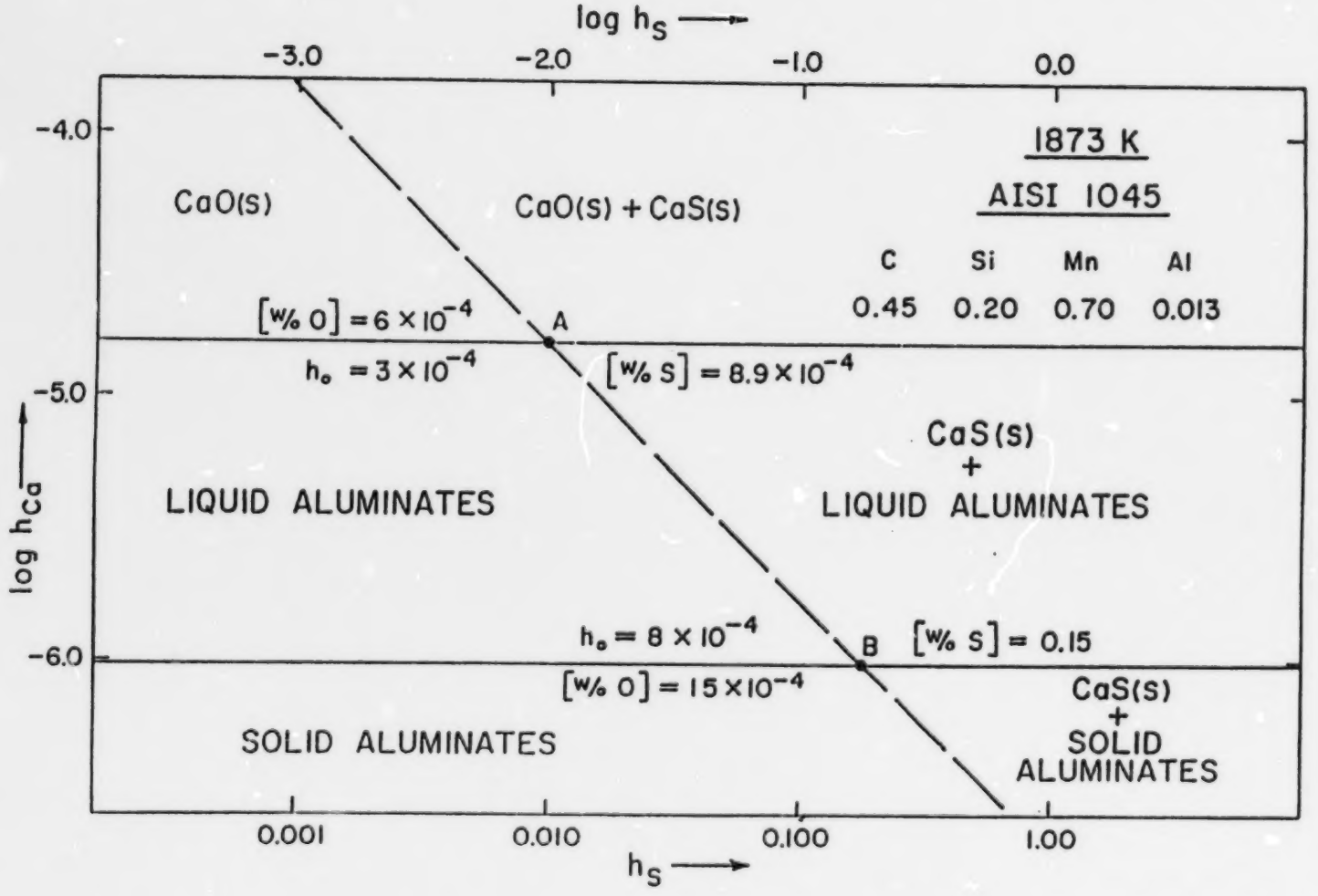

Figure 48: The conditions necessary for the prevention of nozzling clogging for an AISI 1045 steel at 1873 K.

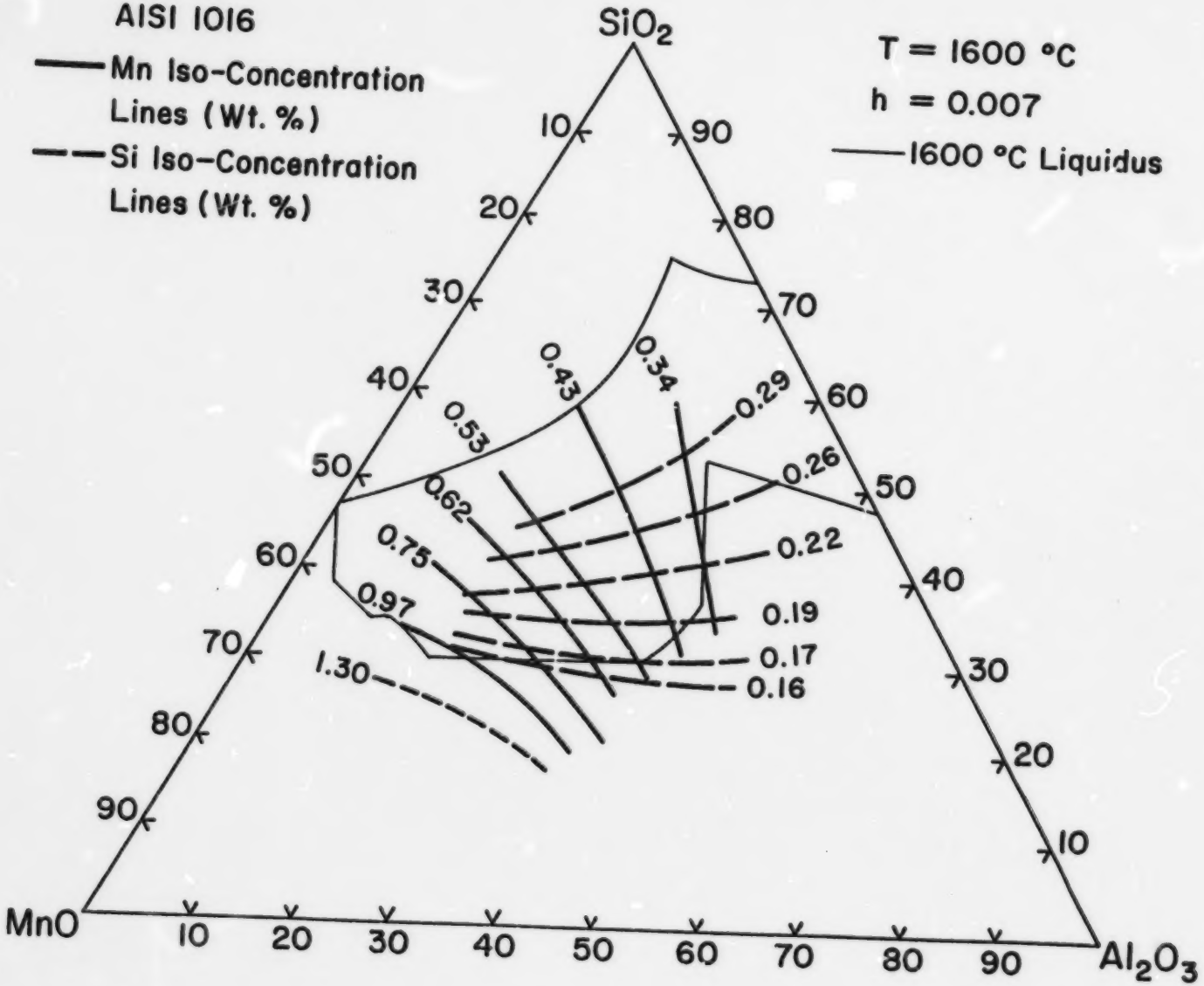

Figure 49: Iso-weight percent curves for silicon and manganese as a function of inclusion composition on the MnO-SiO_2-Al_2O_3 system for an AISI 1016 steel at 1600 C with h_o =0.0070.

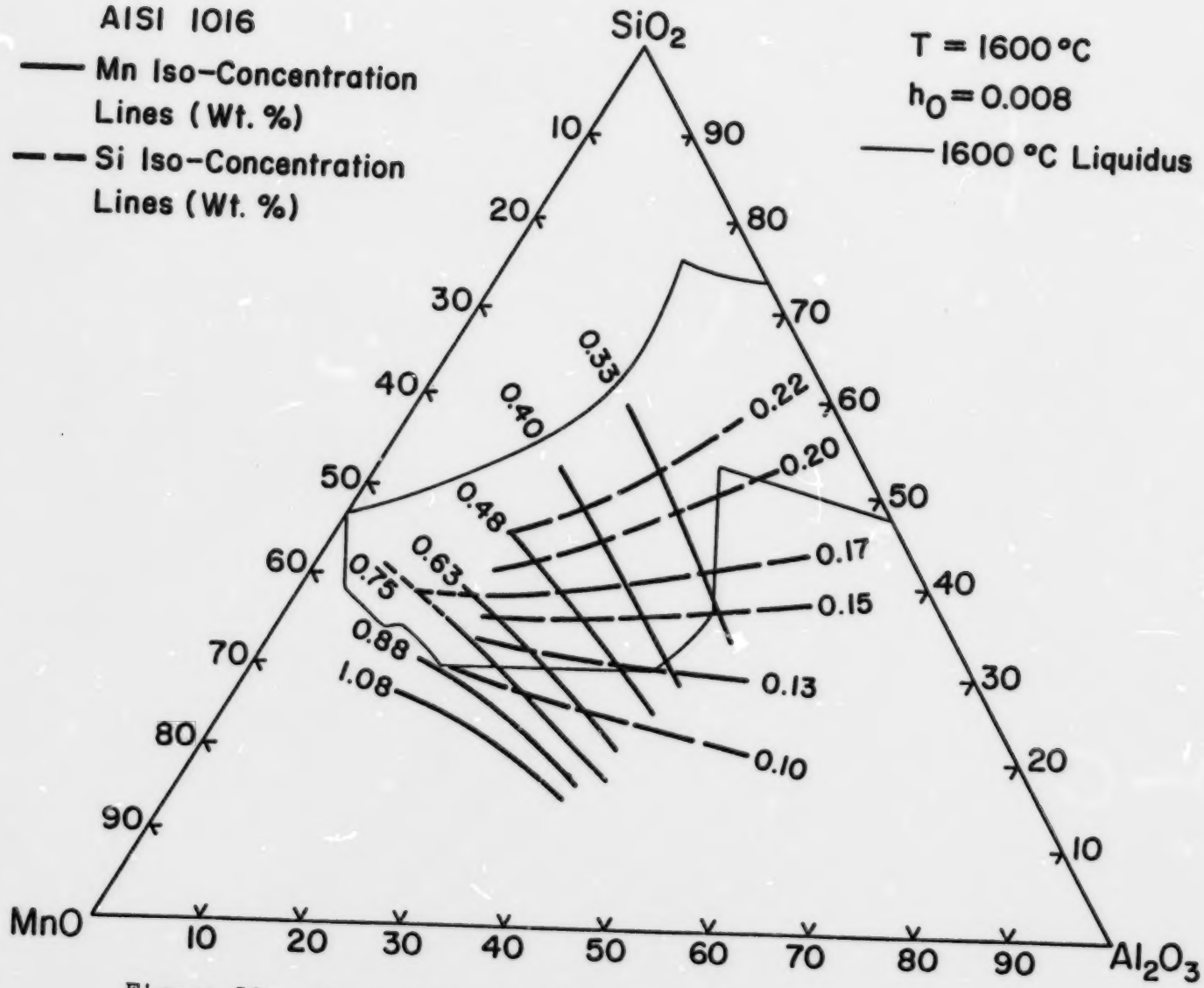

Figure 50: Iso-weight percent curves for silicon and manganese as a function of inclusion composition on the $MnO-SiO_2-Al_2O_3$ system for an AISI 1016 steel at 1600 C with h_o = 0.0080.

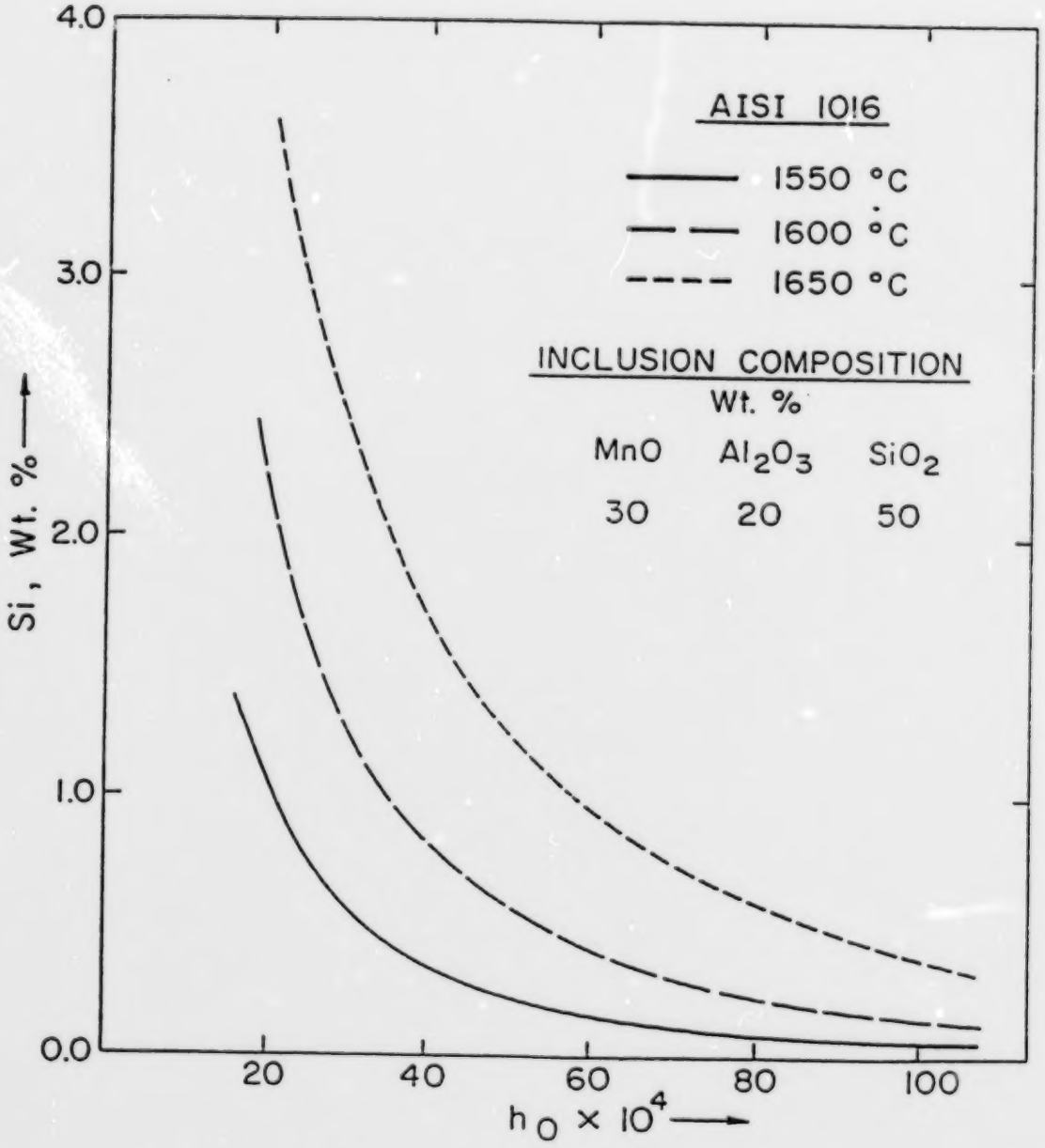

Figure 51: The effect of soluble oxygen (h_o) and temperature on the silicon content of steel in equilibrium with an inclusion containing 30% MnO, 20% Al_2O_3 and 50% SiO_2 by weight.

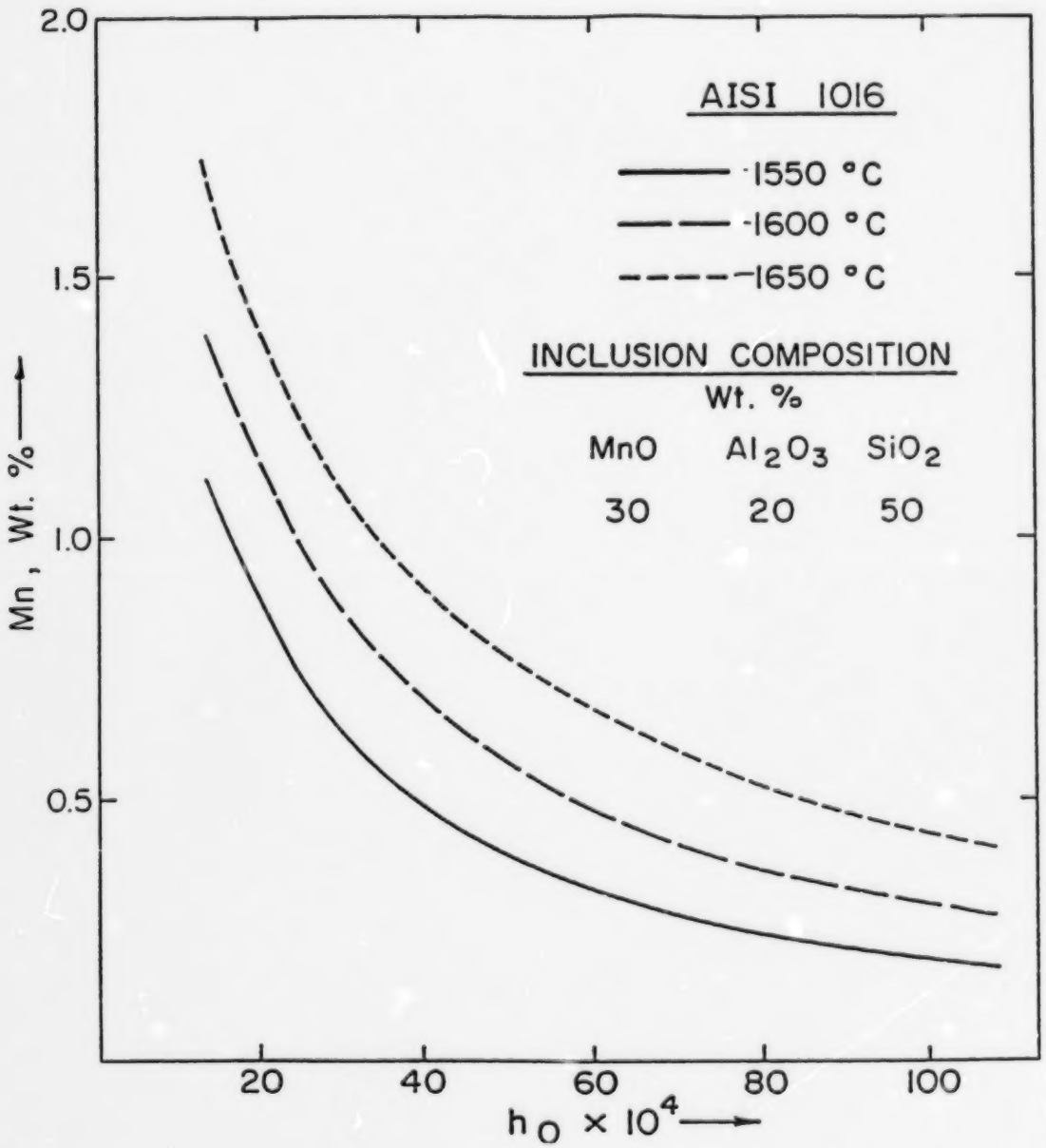

Figure 52: The effect of oxygen and temperature on the manganese content of steel in equilibrium with a inclusion containing 30%MnO, 20%Al_2O_3 and 50%SiO_2 by weight.

APPENDIX I

STEEL/SLAG EQUILIBRIUM MODEL BY JIANG

```
C VARIABLES
C HO: OXYGEN HENRIAN ACTIVITY LEVEL IN STEEL
C HSI:SILICON HENRIAN ACTIVITY LEVEL IN STEEL
C HAL:ALUMINUM HENRIAN ACTIVITY LEVEL IN STEEL
C HMN:MANGANESE HENRIAN ACTIVITY LEVEL IN STEEL
C ---------------------------------------------
C PSIO2:WEIGHT PERCENT OF SIO2 IN SLAG
C PAL2O3:WEIGHT PERCENT OF AL2O3 IN SLAG
C PMNO:WEIGHT PERCENT OF MNO IN SLAG
C ------------------------------------
C ASIO2:RAOULTIAN ACTIVITY OF SIO2 IN SLAG
C AAL2O3:RAOULTIAN  ACTIVITY OF AL2O3 IN SLAG
C AMNO:RAOULTIAN  ACTIVITY OF MNO IN SLAG
C ---------------------------------------
C WWSI:REAL WEIGHT PERCENT OF SI IN STEEL
C WWAL:REAL WEIGHT PERCENT OF AL IN STEEL
C WWMN:REAL WEIGHT PERCENT OF MN IN STEEL
C ---------------------------------------
C (K,I,J)    K:DIFFERENT SLAG COMPOSITION
C            I:DIFFERENT OXYGEN LEVEL
C            J:DIFFERENT TEMPERATURE
C ---------------------------------------
C T:TEMPERATURE
C -------------
C EJI:ELEMENT INTERACTION COEFFICIENT (J TO I)
C --------------------------------------------
C ER:ERROR LIMITATION FOR ITERATION TO OBTAIN THE REAL ELEMENT
C    WEIGHT PERCENT IN THE STEEL
C
C    ER(1):SI  ER(2):MN  ER(3):AL  ER(4):O
C ------------------------------------------------
     DIMENSION      HO(10),PSIO2(25),PAL2O3(25),
     *          ASIO2(25,5),HAL(25,10,5),HSI(25,10,5),
     *          EJI(7,5),WWAL(25,10,5),WWSI(25,10,5),
     *          ER(4),WWO(25,10,5),
     *          AAL2O3(25,5)
        COMMON/A1/     T(5),EK1(5),EK2(5),
     *                 EK3(5),NSI(25,10,5),NMN(25,10,5),
     *
PMNO(25),AMNO(25,5),HMN(25,10,5),WWMN(25,10,5)
        COMMON/A2/     AREFA(25,3,5),PCTP(25,3)
     LEC=4
     IMP=5
     OPEN(UNIT =LEC,FILE ='BB2',STATUS='OLD')
        OPEN(UNIT =IMP,FILE ='LST1',STATUS='NEW')
     WRITE(IMP,*)'PROGRAM   START'

WRITE(IMP,*)'@@@@@@@@@@@@@@@@@@@@@@@@@@@@@@@@@@@@@@@@@@@@@@@@@@@@@@@@@@@'
     CALL  ACTCAL(M,NTEMP,KM,T,IMP)
```

```
      WRITE (IMP,323) KM
  323     FORMAT (6X,'KM=',I3)

WRITE(IMP,*)'~~~~~~~~~~~~~~~~~~~~~~~~~~~~~~~~~~~~~~~~~~~~~~~~~~~~~~~~~~~~'
      DO  110  J=1,NTEMP
      DO  112  K=1,KM
      DO  113  I=1,M
  113     WRITE (IMP,222)  K,K,I,PCTP(K,I),K,I,J,AREFA(K,I,J)
  222     FORMAT
(6X,'KM=',I3,4X,'PCTP(',I2,',',I1,')=',F6.2,'%',4X,
     *                    'AREFA(',I2,',',I1,',',I1,')=',F8.6)
  112
WRITE(IMP,*)'------------------------------------------------------
     *
------------------------------------------------------------------'
  110
WRITE(IMP,*)'~~~~~~~~~~~~~~~~~~~~~~~~~~~~~~~~~~~~~~~~~~~~~~~~~~~~~~~~~~~~~'
      REWIND LEC
C     ---------------------------------
C     ACTIVITIES  IN  THE  STEEL
C-------------------------------------
      READ (LEC,100) K1,LL,HO0,DOXY
  100     FORMAT (3X,I3,3X,I3,3X,F10.5,3X,F8.5)
      WRITE(IMP,*)'    M:NUMBER  OF  OXYGEN  LEVEL'
      WRITE(IMP,*)'    LL:MAX. ITERATION  NUMBER '
         WRITE(IMP,*)'    HO0:THE  LOWEST  OXYGEN  LEVEL'
      WRITE(IMP,*)'    DOXY:OXYGEN  STEP  LENGTH'
      WRITE(IMP,*)'-------------------------------------'
      WRITE(IMP,200) K1,LL,HO0,DOXY
  200   FORMAT ('***',3X,'N=',I2,3X,'LL=',I2,3X,'HO0=',F8.5,3X,
     *           'DOXY=',F8.5)
      DO 10  K=1,KM
         PSIO2(K)=0
         PAL2O3(K)=0
         PMNO(K)=0
      PSIO2(K)=PCTP(K,1)
      PAL2O3(K)=PCTP(K,2)
      PMNO(K)=PCTP(K,3)
      DO 10  J=1,NTEMP
         ASIO2(K,J)=0
         AAL2O3(K,J)=0
         AMNO(K,J)=0
      ASIO2(K,J)=AREFA(K,1,J)
      AAL2O3(K,J)=AREFA(K,2,J)
      AMNO(K,J)=AREFA(K,3,J)
   10   CONTINUE

WRITE(IMP,*)'================================================='
      WRITE(IMP,*)'EQUILIBRIUM      CONSTANT      AT      DIFFERENT
TEMPERATURES'
      WRITE(IMP,*)'    EK1:KSIO2    EK2:KAL2O3    EK3:KMNO'
```

```
WRITE(IMP,*)'================================================='
      DO 20  J=1,NTEMP
         EK1(J)=0
         EK2(J)=0
         EK3(J)=0
      EK1(J)=EXP(71472/T(J)-27.63)
      EK2(J)=EXP(141158/T(J)-46.90)
      EK3(J)=EXP(34511/T(J)-14.92)
      WRITE(IMP,5) J,EK1(J),J,EK2(J),J,EK3(J)
    5
FORMAT(6X,'******','EK1(',I1,')=',E10.3,'******','EK2(',I1,')=',
     *
E10.3/6X,'******','EK3(',I1,')=',E10.3,'*******')
      DO 20  K=1,KM
      DO 30  I=1,K1
         HO(I)=0
         HSI(K,I,J)=0
         HAL(K,I,J)=0
         HMN(K,I,J)=0
         HO(I)=HO0+(I-1)*DOXY
      HSI(K,I,J)=ASIO2(K,J)/HO(I)/HO(I)/EK1(J)
      HAL(K,I,J)=SQRT(AAL2O3(K,J)/HO(I)/HO(I)/HO(I)/EK2(J))
   30    HMN(K,I,J)=AMNO(K,J)/HO(I)/EK3(J)
   20    CONTINUE

WRITE(IMP,*)'_________________________________________________'
         WRITE(IMP,*)'================================='
         WRITE(IMP,*)'INDICES ARE PRINT CHOICE INDICES'
         WRITE(IMP,*)'================================='
      READ (LEC,*) IND1,IND2,IND3
      WRITE (IMP,333) IND1,IND2,IND3
  333    FORMAT ('------','INDEX1=',I1,'------','INDEX2=',I1,
     *  '-------','INDEX3=',I1)
      GO  TO (12,16) IND1
   12    WRITE  (IMP,300)
  300    FORMAT (/1X,'  T(J) ',1X,'KM','     HO ',5X,' SIO2% ',4X,
     *           '       HSI    ',6X,
     *           '  AL2O3%',6X,'  HAL    ')
      DO 50  J=1,NTEMP
      DO 50  K=1,KM
      DO 49  I=1,K1
   49     WRITE                                          (IMP,400)
T(J),K,HO(I),PSIO2(K),HSI(K,I,J),PAL2O3(K),
     *                        HAL(K,I,J)
  400    FORMAT (/1X,F6.0,1X,I2,3X,F7.5,3X,F6.1,4X,F12.4,7X,F6.1,
     *          4X,F10.6)
   50
WRITE(IMP,*)'-------------------------------------------------
     *
-------------------------------------------------------'
         WRITE(IMP,444)
  444    FORMAT(/2X,'T(J) ',' KM ',4X,'HO ',11X,
```

```
     *       'MNO%    ',1X,'  HMN   ')
          DO  60  J=1,NTEMP
          DO  60  K=1,KM
          DO  59  I=1,K1
   59     WRITE(IMP,555)T(J),K,HO(I),PMNO(K),
     *    HMN(K,I,J)
  555     FORMAT(/1X,F6.0,1X,I2,3X,F7.5,7X,F6.2,
     *           4X,F6.2)
   60
WRITE(IMP,*)'-----------------------------------------------
     *
-------------------------------------------------------'
C
C         ---------------------------------
C         CONCENTRATIONS  IN  THE  STEEL
C         ---------------------------------
C
   16       DO  111  J=1,7
       READ (LEC,*)  EJI(J,1),EJI(J,2),EJI(J,3),EJI(J,4),EJI(J,5)
  111 CONTINUE
          DO  234  J=1,7
  234     WRITE(IMP,208)J,EJI(J,1),J,EJI(J,2),J,EJI(J,3)
  208     FORMAT('---','EJI(',I1,',',')=',F6.3,2X,'EJI(',I1,',',
     *           '2)=',F6.3,2X,'EJI(',I1,',',')=',F6.3)

WRITE(IMP,*)'-----------------------------------------------'
          DO  235  J=1,7
  235     WRITE(IMP,505)J,EJI(J,4),J,EJI(J,5)
  505
FORMAT('---','EJI(',I1,',',')=',F7.3,2X,'EJI(',I1,',',')=',
     *           F8.4)

WRITE(IMP,*)'***********************************************'
       DO  108  I=1,4
       READ (LEC,*) ER(I)
  108       WRITE (IMP,118)  I,ER(I)
  118       FORMAT (2X,'**','ER(',I2,')=',F10.8)

WRITE(IMP,*)'-----------------------------------------------'
          WRITE(IMP,*)'======================================='
          WRITE(IMP,*)'CWC,CWP,CWS ARE REAL CARBON,PHOSPHORUS'
          WRITE(IMP,*)'AND SULPHUR CONTENTS IN THE STEEL'
          WRITE(IMP,*)'======================================='
       READ (LEC,*)  CWC,CWP,CWS
       WRITE  (IMP,510)  CWC,CWP,CWS
  510     FORMAT (4X,'CWC=',F6.4,3X,
     *           'CWP=',F6.4,3X,'CWS=',F6.4)
          WRITE(IMP,*)'==================================='
          WRITE(IMP,*)'CSI,CMN ARE TARGET ELEMENT CONTENT'
          WRITE(IMP,*)'     FOR SI AND MN'
          WRITE(IMP,*)'ESI,EMN ARE LIMITING ERROR '
          WRITE(IMP,*)'     FOR SI,MN SELECTION '
```

```
      WRITE(IMP,*)'==================================='
      READ (LEC,*) CSI,CMN,ESI,EMN
      WRITE (IMP,515) CSI,CMN,ESI,EMN
  515 FORMAT ('*******',4X,'CSI=',F5.3,3X,'CMN=',F5.3,3X,
     *        'ESI=',F5.3,3X,'EMN=',F5.3)

WRITE(IMP,*)'*****************************************************'
C     -----------------
C        ITERATION
C     -----------------
C
      DO  77  J=1,NTEMP
      DO  66  K=1,KM
C
C  1)   ---------------------------------------
C        ITERATION  TO  CALCULATE  SI%  IN  STEEL
C        ---------------------------------------
C
      DO  900  I=1,K1
         X1=HSI(K,I,J)
         WWSI(K,I,J)=0
         NSI(K,I,J)=0
      DO  800  L=1,LL
      X2=EXP(ALOG(HSI(K,I,J))-2.303*(EJI(1,3)*HAL(K,I,J)
     *     +EJI(2,3)*CWC+EJI(3,3)*X1+EJI(4,3)*HO(I)
     *     +EJI(5,3)*HMN(K,I,J)+EJI(6,3)*CWP+EJI(7,3)*CWS))
      IF (ABS(X1-X2) .LE. ER(1))  GO TO  1000
      X1=X2
  800     CONTINUE
 1000   WWSI(K,I,J)=X2
      WRITE (IMP,512) I,HO(I),L,K,I,J,X2
  512 FORMAT ('*****',2X,'HO(',I2,')=',F7.5,2X,'L=',I2,3X,
     *        'W%SI(',I2,',',I2,',',I1,')=',F10.6)
      IF (ABS(X2-CSI) .LE. ESI )  GO TO 1001
      GO TO 900
 1001     WRITE(IMP,*)'#######    CSI  FOUND    ########'
      NSI(K,I,J)=I
  900 CONTINUE

WRITE(IMP,*)'-----------------------------------------------'
C
C  2)   ---------------------------------------
C        ITERATION  TO  CALCULATE  MN%  IN  STEEL
C        ---------------------------------------
C
      GO TO (32,33) IND2
   32    DO 910  I=1,K1
         WWMN(K,I,J)=0
         NMN(K,I,J)=0
      X1=HMN(K,I,J)
      DO 810  L=1,LL
      X2=EXP(ALOG(HMN(K,I,J))-2.303*(EJI(1,5)*HAL(K,I,J)
```

```
     *  +EJI(2,5)*CWC+EJI(3,5)*WWSI(K,I,J)+EJI(4,5)*HO(I)
     *  +EJI(5,5)*X1+EJI(6,5)*CWP+EJI(7,5)*CWS))
      IF (ABS(X1-X2)  .LE. ER(2))   GO  TO   1010
         X1=X2
  810    CONTINUE
 1010   WWMN(K,I,J)=X2
      WRITE (IMP,312)  I,HO(I),L,K,I,J,X2
  312    FORMAT
('*****',2X,'HO(',I2,')=',F7.5,2X,'L=',I2,3X,'W%MN(',I2,
     *          ',',I2,',',I1,')=',F10.6)
      IF  (ABS(X2-CMN)  .LE. EMN)  GO TO 1110
      GO TO 910
 1110   WRITE(IMP,*)'######    CMN  FOUND   ######'
      NMN(K,I,J)=I
  910   CONTINUE
      WRITE(IMP,*)'-----------------------------------------------'

C
C  3)   ---------------------------------------
C       ITERATION  TO  CALCULATE  AL%  IN  STEEL
C     ---------------------------------------------
   33     DO 950  I=1,K1
         WWAL(K,I,J)=0
      X1=HAL(K,I,J)
      DO 850  L=1,LL
      X2=EXP(ALOG(HAL(K,I,J))-2.303*(EJI(1,1)*X1+EJI(2,1)*CWC
     *  +EJI(3,1)*WWSI(K,I,J)+EJI(4,1)*HO(I)+EJI(5,1)*WWMN(K,I,J)

     *  +EJI(6,1)*CWP+EJI(7,1)*CWS))
      IF (ABS(X1-X2)  .LE.  ER(3))   GO  TO  1050
      X1=X2
  850   CONTINUE
 1050   WWAL(K,I,J)=X2
         WRITE (IMP,612)  I,HO(I),L,K,I,J,X2
  612   FORMAT ('*****',2X,'HO(',I2,')=',F7.5,2X,
     *          'L=',I2,3X,'W%AL(',I2,',',I2,',',I1,')=',F12.8)
  950   CONTINUE
      WRITE(IMP,*)'-----------------------------------------------'

C
C  4)   ---------------------------------
C     ITERATION  FOR  O%  IN  STEEL
C     -------------------------------
C
      DO  960  I=1,K1
         WWO(K,I,J)=0
      X1=HO(I)
      DO  860  L=1,LL
      X2=EXP(ALOG(HO(I))-2.303*(EJI(1,4)*WWAL(K,I,J)+EJI(2,4)*CWC
     *  +EJI(3,4)*WWSI(K,I,J)+EJI(4,4)*X1+EJI(5,4)*WWMN(K,I,J)
     *  +EJI(6,4)*CWP+EJI(7,4)*CWS))
      IF (ABS(X1-X2)  .LE. ER(4))   GO TO 1060
```

```
      X1=X2
  860      CONTINUE
 1060    WWO(K,I,J)=X2
      WRITE (IMP,712)  I,HO(I),L,K,I,J,X2
  712      FORMAT ('@@@@@',2X,'HO(',I2,')=',F7.5,2X,'L=',I2,3X,
     *             'W%O(',I2,',',I2,',',I1,') =',F12.8)
  960    CONTINUE
      WRITE(IMP,*) '-------------------------------------------'

WRITE(IMP,*)'-----------------------------------------------------'
      DO  3000  I=1,K1
         GO  TO(178,2000) IND3
  178    IF  (NSI(K,I,J).NE.NMN(K,I,J))  GO TO 3000
 2000      WRITE                                              (IMP,812)
K,I,HO(I),K,I,J,HSI(K,I,J),K,I,J,HMN(K,I,J)
  812
FORMAT(I2,7X,'HO(',I2,')=',F8.5,3X,'HSI(',I2,',',I2,',',
     *      I1,')=', F8.3,3X,'HMN(',I2,',',I2,',',I1,')=',F8.3)

WRITE(IMP,*)'-----------------------------------------------------
---
     *  ----------------------------------------'
         WRITE(IMP,183)  K,I,J,WWO(K,I,J),
     *                   K,I,J,WWSI(K,I,J),K,I,J,WWMN(K,I,J)
  183    FORMAT( 3X,'WWO(',I2,',',I2,',',I1,')=',
     *       F8.5,2X,'WWSI(',I2,',',I2,',',I1,')=',F8.3,2X,
     *       'WWMN(',I2,',',I2,',',I1,')=',F8.3)

WRITE(IMP,*)'-----------------------------------------------------
---
     *  ----------------------------------------'
         WRITE(IMP,803) K,I,HO(I),K,I,J,HAL(K,I,J)
  803    FORMAT(2X,'K=',I2,3X,'HO(',I2,')=',F8.5,3X,
     *       'HAL(',I2,',',I2,',',
     *       I1,')=',F8.6)

WRITE(IMP,*)'-----------------------------------------------------
---
     *  ----------------------------------------'
         WRITE(IMP,184) K,I,J,WWAL(K,I,J)
  184    FORMAT(26X,'WWAL(',I2,',',I2,',',I1,')=',F8.6/)

WRITE(IMP,*)'-------------------------------------------------'
         WRITE(IMP,813)K,J,T(J),K,PSIO2(K),K,PAL2O3(K),
     *                   K,PMNO(K)
  813
FORMAT(/6X,'KM=',I2,6X,'T(',I1,')=',F5.0/6X,'PSIO2(',I2,')=',
     *   F6.2,'%',6X,'PAL2O3(',I2,')=',F6.2,'%'/7X,
     &          'PMNO(',I2,')=',F6.2,'%')

WRITE(IMP,*)'^^^^^^^^^^^^^^^^^^^^^^^^^^^^^^^^^^^^^^^^^^^^^^^^^^^^'
 3000      CONTINUE
```

```
   66     CONTINUE
WRITE(IMP,*)'^^^^^^^^^^^^^^^^^^^^^^^^^^^^^^^^^^^^^^^^^^^^^^^^^^^^^^^^^^^^^^^^'
   77   CONTINUE
      STOP
      END
C     END  A3
CC
CC
CC
C
C **********************
C INPUT DESCRIPTION
C **********************
C
C A)
C TITRE:TITLE
C
C B)
C IEDI:PRINTING INDEX (0:SIMPLE PRINTING 1:FULL PRINTING)
C IVP:SLAG COMPOSITION INDEX(0:MOLAR FRACTION 1:wt%)
C M:NUMBER OF SLAG CONSTITUENTS
C INDEX:CALCULATION INDEX
C       1:R(I,J),GM,GE
C       2:R(I,J),GM,GE,HM,SE
C       3:R(I,J),GM,GE,ACT(I)
C       4:R(I,J),GM,GE,HM,SE,ACT(I)
C
C C)
C FOR M COMPONENTS FORMED M(U)O(V) ARRANGED IN INCREASING
C         RATIO U/V
C U(I):STOICHIOMETRIC NUMBER OF OXIDE(FOR METAL)
C V(I):STOICHIOMETRIC NUMBER OF OXIDE(FOR OXYGEN)
C PM(I):MOLAR MASS OF COMPONENT
C DHREF(I):ENTHALPY DIFFERENCE IN REFERENCE
C DSREF(I):ENTROPY DIFFERENCE IN REFERENCE
C
C D)
C W(1,I,J),W(2,I,J) FORMATION ENERGY(I=1,...,M-1)
C E(1,I,J),E(2,I,J) INTERACTION ENERGY(J=I+1,...,M)
C
C E)
C NCS:NUMBER OF STOICHIOMETRIC COMPOUNDS FOR WHICH ONE WANTS
C      TO CALCULATE THE ACTIVITY
C ACSIM:THE MINIMUM VALUE OF THE COMPOUND ACTIVITY FOR PRINTING
C        (IF ACT(I)<ACSIM NO PRINTING)
C
C F)
C CST(J):NAME OF THE COMPOUND
C  ICS(J,I):STOICHIOMETRIC   NUMBER  OF  EACH  COMPONENT  OF  THE
COMPOUND
C DHC(J):COMPOUND ENTHALPY DIFFERENCE IN REFERENCE
```

```
C DSC(J):COMPOUND ENTROPY DIFFERENCE IN REFERENCE
C
C G)
C NCSS:NUMBER OF IDEAL SOLID SOLUTIONS
C H)
C
C CCSS(J):NAME OF SOLID SOLUTION
C ICSS(J,1):INDEX OF TWO EXTREME NUMBERS(THE LARGEST)
C ICSS(J,2):INDEX OF TWO EXTREME NUMBERS(THE SMALLEST)
C
C I)
C J0:INDEX FOR FIXING SOME VALUES OF COMPOUND ACTIVITY
C    0:DO NOT USE THE POSIBILITY
C    OTHER DIGIT:ALREADY USED
C ACONT0:COMPOUND ACTIVITY
C I0:INDEX OF A COMPONENT WHOSE COMPOSITION CAN BE MODIFIED
C    TO SATISFY THE VALUE OF THE ACTIVITY GOT BEFOR
C ITERM:MAXIMUM NUMBER OF ITERATION
C PREC:CALCULATION PRECISION
C I00:COMPONENT INDEX WHICH WILL BE USED EVENTUALLY TO
C     CALCULATE A SIMPLIFIED COMPOSITION OF SLAG
C
C J)
C NTEMP:NUMBER OF TEMPERATURES TO BE STUDIED
C TEMP0:PRIMARY TEMPERATURE VALUE(KELVIN)
C DTEMP:TEMPERATURE INCREMENT
C
C K)
C (M-1)CARDS DEALING WITH A SLAG COMPOSITION
C NCF(I):INDEX CONCERNED WITH COMPONENTS
C NX(I):NUMBER OF DIFFERENT VALUES FOR THE COMPONENT
C X0(I):INITIAL VALUE (IN MOLAR FRACTION OR WEIGHT PERCENT)
C DX(I):STEP LENGTH OF COMPOSITION CALULATION(IN MOLAR
C       FRACTION OR WEIGHT PERCENT)
C ***************************************************************
      SUBROUTINE ACTCAL(M,NTEMP,KM,T,IMP)
      DIMENSION
TITRE(10),U(3),V(3),W(2,3,3),E(2,3,3),X(3),XX(25,3),
     *        X0(3),DX(3),R(3,3),ACT(3),NCF(3),CEREF(3,5),PCT(3),
     *      ACTA(25,3,5),T(5),NX(3),PM(3),
     *      KMM(3),CONST(3,2),DHREF(3),DSREF(3),CST(4),ICS(4,3),
     *
ACS0(22,5),ACS(4,5),DHC(4),DSC(4),CCSS(2),ICSS(2,2),
     *      ACSI(4),AREF(3,5),CSTI(4)
        COMMON/A2/ AREFA(25,3,5),PCTP(25,3)
      LOGICAL SNV,SOK
      LEC=3
         WRITE(IMP,*)'START  OF ACTCAL'
         OPEN(UNIT = LEC,FILE = 'JJ1MN')
      READ  (LEC,100)  (TITRE(I),I=1,10)
  100     FORMAT (10(A5/))
```

```
      WRITE (IMP,200)  (TITRE(I),I=1,10)
  200     FORMAT ( '1',10(A5/1X)/41('*')/)
      READ  (LEC,105) IEDI,IVP,M,INDEX
  105   FORMAT (I1,10X,I1,10X,I1,10X,I1)
      WRITE (IMP,17)  IEDI,IVP,M,INDEX
   17   FORMAT (4X,I1,10X,I1,10X,I1,10X,I1)
        IF  (M-1) 50,50,6
    6   WRITE (IMP,213)
  213     FORMAT  (2X,'CONSTITUENTS:')
      NCSIM=10-M
      DO 3 I=1,M
      READ                                                    (LEC,101)
CONST(I,1),CONST(I,2),U(I),V(I),PM(I),DHREF(I),
     *          DSREF(I)
  101   FORMAT (A4,7X,A4,7X,F2.0,3X,F2.0,3X,F5.1,3X,F8.1,3X,F5.2)

      WRITE (IMP,444) I,U(I),I,V(I),I,PM(I)
  444
FORMAT(4X,'U(',I1,')=',F3.1,4X,'V(',I1,')=',F3.1,4X,'PM(',
     *       I1,')=',F6.2)
    3     WRITE                                               (IMP,214)
I,CONST(I,1),CONST(I,2),DHREF(I),DSREF(I)
  214     FORMAT(5X,'(',I1,')  ',2(A4,2X),'  DHREF=',F8.1,
     *             '(CAL)    DSREF=',F5.2,'  ( U.E.)')
        DO 909  K=1,2
        DO 909  I=1,M
        DO 909  J=1,M
        W(K,I,J)=0
        E(K,I,J)=0
  909   CONTINUE
      DO 2 I=1,M-1
      DO 2 J=I+1,M
    2     READ (LEC,*) W(1,I,J),W(2,I,J),E(1,I,J),E(2,I,J)
      READ (LEC,*) NCS,ACSIM
      IF   (NCS) 40,40,41
   41     WRITE (IMP,215)
  215     FORMAT (2X,'COMPOSES:')
      DO 42 J=1,NCS
      READ (LEC,102) CST(J)
  102   FORMAT(A6)
        READ(LEC,*)(ICS(J,I),I=1,M),DHC(J),DSC(J)
   42     WRITE (IMP,216) J,CST(J),DHC(J),DSC(J)
  216     FORMAT (4X,'(',I2,')  ',A6,'   DHF=',F9.0,
     *         '  (CAL)  DSF= ',F7.2,' (U.E.)')
   40     READ (LEC,*) NCSS
     IF (NCSS) 49,49,47
   47     WRITE (IMP,220)
  220     FORMAT (2X,'SOLUTIONS SOLIDES:')
      DO 48 J=1,NCSS
      READ (LEC,103)  CCSS(J),ICSS(J,1),ICSS(J,2)
  103     FORMAT (1A4,2I2)
      I1=ICSS(J,1)
```

```
      I2=ICSS(J,2)
   48      WRITE (IMP,221)  J,CCSS(J),CST(I1),CST(I2)
  221      FORMAT  (4X,'(',I2,')    ',1A5,':',2X,1A5,'/',1A5)
   49      READ (LEC,*)  J0,ACONT0,I0,ITERM,PREC,I00
      WRITE (IMP,217)
  217      FORMAT   (2X,'PARAMETERS      ENERGETIQUES   DU  MODELE
(CAL):')
      DO 1  I=1,M-1
      DO 1  J=I+1,M
    1    WRITE  (IMP,201) I,J,W(1,I,J),I,J,W(2,I,J),
     *                        I,J,E(1,I,J),I,J,E(2,I,J)
  201      FORMAT (2X,'  W(1,',I1,',',I1,')=',F10.2,4X,
     *          'W(2,',I1,',',I1,')=',F10.2,4X/2X,
     *          '  E(1,',I1,',',I1,')=',F10.2,4X,
     *          'E(2,',I1,',',I1,')=',F10.2)
           READ (LEC,*) NTEMP,TEMP0,DTEMP
      WRITE (IMP,133) NTEMP,TEMP0,DTEMP
  133      FORMAT
(2X,'NTEMP=',I2,4X,'******',4X,'TEMP0=',F6.1,4X,'******',
     *          4X,'DTEMP=',F5.1,'******')
      DO 5  I=1,M
    5      NX(I)=1
      DO 4  I=1,M-1
      READ (LEC,*)  NCF(I),NX(I),X0(I),DX(I)
    4      WRITE (IMP,22) I,NCF(I),I,NX(I),I,X0(I),I,DX(I)
   22
FORMAT(4X,'NCF(',I1,')=',I2,4X,'NX(',I1,')=',I2,4X,'X0(',
     *        I1,')=',F4.1,4X,'DX(',I1,')=',F4.1)
      DO 7   I=1,M
      DO 8   J=1,M-1
      K=NCF(J)
      IF (I-K) 8,7,8
    8      CONTINUE
      NCC=I
    7      CONTINUE
      DO 10  ITEMP=1,NTEMP
         T(ITEMP)=0
      T(ITEMP)=TEMP0+(ITEMP-1)*DTEMP
         TT=T(ITEMP)
      DO 43  I=1,M
   43
CEREF(I,ITEMP)=EXP((DHREF(I)-T(ITEMP)*DSREF(I))/1.987/T(ITEMP))
      DO 44  I=1,NCS
   44
ACS0(I,ITEMP)=EXP(-(DHC(I)-T(ITEMP)*DSC(I))/1.987/T(ITEMP))
      WRITE(IMP,*)'*******************************************'
      WRITE (IMP,202)  ITEMP,T(ITEMP)
  202      FORMAT   (4X,'ITEMP=',I1,'          TEMPERATURE=',F6.0,'
KELVIN'/
     *             1X,60('*'))
      IF (IEDI  .EQ.0) GO TO 24
      GO  TO  19
```

```
 24    DO  26  I=1,M
       WRITE (IMP,211)  I,I
211      FORMAT  (/2X,3X,'%',I1,16X,'  ACT(',I1,')')

 26    CONTINUE
   WRITE(IMP,*)'     ACTIVITIES OF COMPOUNDS'
 19      NX(M)=1
   KMM(M)=1
   DO 93 I=M-1,1,-1
 93    KMM(I)=KMM(I+1)*NX(I+1)
   KM=KMM(1)*NX(1)
   WRITE (IMP,303) KM
303    FORMAT (4X,'KM=',I3)
   DO 10  KC=1,KM
   DO 113 I=1,M
   PCT(I)=0
   PCTP(KC,I)=PCT(I)
   AREF(I,ITEMP)=0
      AREFA(KC,I,ITEMP)=AREF(I,ITEMP)
113      CONTINUE
   KCC=KC-1
      IF  (IVP)  10,80,90
 80      DO  81 I=1,M-1
   II=INT(KCC/KMM(I))
   K=NCF(I)
   X(K)=X0(I)+II*DX(I)
 81      KCC=KCC-II*KMM(I)
   GO  TO  11
 90      PCT(NCC)=100.
   DO 91  I=1,M-1
   II=INT(KCC/KMM(I))
   K=NCF(I)
   PCT(K)=X0(I)+II*DX(I)
   PCT(NCC)=PCT(NCC)-PCT(K)
 91      KCC=KCC-II*KMM(I)
   S=0.
   DO  92  I=1,M
 92      S=S+PCT(I)/PM(I)
   DO 906 I=1,M
906      X(I)=PCT(I)/PM(I)/S
 11      ITER=0
 70    X(NCC)=1.0
   DO  12  I=1,M-1
   K=NCF(I)
 12      X(NCC)=X(NCC)-X(K)
   XX(KC,NCC)=X(NCC)
      WRITE (IMP,305) KC,NCC,XX(KC,NCC)
305    FORMAT (2X,'X(KC,NCC)=X(',I2,',',I2,')=',F6.4)
   DO 13  I=1,M
      ACT(I)=0
      ACTA(KC,I,ITEMP)=0
   IF  (X(I)) 10,13,13
```

```
   13     CONTINUE
      CALL
CTHMKF(M,U,V,W,E,TT,X,INDEX,.001,SNV,SOK,R,GM,GE,HM,SE,ACT,
     *       IMP)
      IF (SNV)  WRITE (IMP,203)
  203     FORMAT (/2X,'SNV')
          DO 333 I=1,M
      ACTA(KC,I,ITEMP)=ACT(I)
  333 CONTINUE
      IF  (SNV)  GO TO 10
      IF  ((J0-1)*(J0-NCS)) 60,60,15
   60     IF  (ITER-ITERM)  64,64,15
   64     IF  (X(I0)*X(I00))  15,15,65
   65     ACS(J0,ITEMP)=ACS0(J0,ITEMP)
      DO  61  I=1,M
      IF (ICS(J0,I))  63,61,62
   63     IF (ACT(I)*CEREF(I,ITEMP))  15,15,62
   62     ACS(J0,ITEMP)=ACS(J0,ITEMP)*(ACT(I)*CEREF(I,ITEMP))
     *                **ICS(J0,I)
   61     CONTINUE
      IF  (ABS(ACS(J0,ITEMP)/ACONTO-1) .LT. PREC) GO TO 15
      WRITE(IMP,*)'  ???   SOK   ???'

X(I0)=X(I0)*(1+(ACONTO/ACS(J0,ITEMP))**(1/U(I0)/ICS(J0,I0)))/2
      ITER=ITER+1
      GO TO 70
   15     WRITE(IMP,*)'PREC IS OK!!!'
      IF  (IEDI  .EQ. 0) GO TO  16
      IF  (SOK)  WRITE (IMP,204)
  204     FORMAT  (/2X,'SOK!!!!')
      WRITE  (IMP,205)  GM,GE
  205     FORMAT  (3X,'GM  =',F8.0,'  CAL/MOLE       GE =',F8.0,'
CAL/MOLE')
      GO TO  (10,25,30,25),INDEX
   25     WRITE  (IMP,206)  HM,SE
  206     FORMAT (3X,'HM =',F8.0,' CAL/MOLE          SE =',F8.3,'
CAL/MOLE/K')
      GO TO  (10,10,30,30),INDEX
   30     WRITE  (IMP,207) KC,ITEMP,KC,ITEMP,ITEMP
  207     FORMAT (3X,'(I)   X(I)   %(I)',
     *
5X,'ALIQ(',I2,',I,',I1,')',5X,'AREF(',I2,',I,',I1,
     *          ')',5X,'T(',I1,')','(C)')
   16   S=0.
      DO  32  I=1,M
   32     S=S+.01*X(I)*PM(I)
      DO  31  I=1,M
      PCT(I)=X(I)*PM(I)/S
      PCTP(KC,I)=PCT(I)
      AREF(I,ITEMP)=ACT(I)*CEREF(I,ITEMP)
   31   CONTINUE
        DO 73 I=1,M
```

```
 73      AREFA(KC,I,ITEMP)=AREF(I,ITEMP)
         DO 74 I=1,M
       IF (AREF(I,ITEMP) .GE. 1)  AREF(I,ITEMP)=1
 74      IF (IEDI .EQ. 1)  WRITE (IMP,208) I,X(I),PCT(I),
       *    ACT(I),AREF(I,ITEMP),T(ITEMP)-273.
208      FORMAT  (I5,F8.3,1X,F6.2,6X,F10.6,6X,F10.6,6X,F7.0)
         WRITE(IMP,*)'^^^
```

```
      ACSI(NCSI)=ACSS
   96     CONTINUE
   88     IF  (NCSI  .GT. 0)  GO TO 89
      NCSI=1
      ACSI(1)=0.
   89     NCSIO=MINO(NCSI,NCSIM)
      WRITE(IMP,*)  (PCT(I),I=1,M),(ACT(I)*CEREF(I,ITEMP),I=1,M),
     *          (ACSI(I),I=1,NCSIO),
     *       (CSTI(I),I=1,NCSIO)
        IF (ACSI(I) .GT.0)  WRITE(IMP,*)
     * (ACSI(I),I=NCSIM+1,NCSIM+NCSIO),
     * (CSTI(I),I=NCSIM+1,NCSIM+NCSIO)
      NCSIO=MINO((NCSI-NCSIM),NCSIM)
      IF  (NCSIO  .GT. 0)  WRITE (IMP,*)
     *       (ACSI(I),I=NCSIM+1,NCSIM+NCSIO),
     *       (CSTI(I),I=NCSIM+1,NCSIM+NCSIO)
      NCSIO=MINO((NCSI-2*NCSIM),NCSIM)
      IF  (NCSIO  .GT. 0)  WRITE (IMP,*)
     *       (ACSI(I),I=2*NCSIM+1,2*NCSIM+NCSIO),
     *       (CSTI(I),I=2*NCSIM+1,2*NCSIM+NCSIO)
      IF  (JO  .GT. 0)  WRITE  (IMP,218) RX
  218     FORMAT  (2X,'RX =',F6.3)
      WRITE (IMP,230)  GM,GE,HM,SE
  230     FORMAT  (2X,'GM=',F8.0,'   GE=',F8.0,'   HM=',F8.0,
     *          '   SE=',F8.3)
   10     CONTINUE
      WRITE(IMP,*)'         END   OF    ACTCAL          '
      WRITE(IMP,*)'^^^^^^^^^^^^^^^^^^^^^^^^^^^^^^^^^^^^^^^^^^^^^^^^^^^^^^^^^^^^'
   50     RETURN
      END
C     END  ACTCAL
C
C
C
C
C
C
C ************************************
C M:NUMBER OF OXIDES
C U(I) AND V(I):STOICHIOMETRIC INDEX ACCORDING TO METAL
C       ELEMENT VALENCES
C W(2,I,J):FORMATION ENERGY OF CELLS I-O-J(KCAL)
C E(2,I,J):INTERACTION ENERGY OF CELLS I-O-J AND I-O-I(KCAL)
C T:TEMPERATURE(KELVIN)
C X(I):MOLAR FRACTION OF OXIDES
C INDEX:FOR CALCULATION TYPE
C PREC:CALCULATION PRECISION
C SNV:LOGICAL VARIABLE
C SOK:LOGICAL VARIABLE
C R(I,J):CELL FRACTION I-O-J AT POINT X
C GM:MIXING FREE ENTHALPY AT POINT X
C GE:EXCESS FREE ENTHALPY AT POINT X
```

```
C HM:MIXING ENTHALPY(CALCULATED IF INDEX=2,4)
C SE:EXCESS ENTROPY (CALCULATED IF INDEX=2,4)
C ACT(I):COMPONENT ACTIVITIES(CALCULATED IF INDEX=3,4)
C ***************************************************
      SUBROUTINE                                                CTHMKF
(M,U,V,W,E,TT,X,INDEX,PREC,SNV,SOK,R,GM,
     *                        GE,HM,SE,ACT,IMP)
      DIMENSION
U(3),V(3),W(2,3,3),E(2,3,3),X(3),R(3,3),ACT(3),
     *
UR(3),VR(3),WR(2,3,3),ER(2,3,3),XR(3),RR(3,3),IR(3),
     *            XM(3),XP(3),RM(3,3),RP(3,3),DG(3)
      LOGICAL     SNV,SOK,SOKP
     WRITE(IMP,*)'START  OF  CTHMKF'
C
C       INITIALISATION
C       A)
        SNV=.FALSE.
        SOK=.TRUE.
        GM=0.0
        GE=0.0
        HM=0.0
        SE=0.0
        DO  1   I=1,M
        ACT(I)=0.0
        DO  1   J=1,M
    1   R(I,J)=0.0
C
C       B)   INDEXATION
C
        MR=0
        DO  5  I=1,M
        IF  (X(I)-.00001)  5,5,6
    6   MR=MR+1
        IR(MR)=I
    5   CONTINUE
C
C       C)  STOP  CALCULATION  FOR  SINGLE  CONSTITUENT
C
        IF  (MR-1)  11,10,14
   10   I=IR(MR)
        ACT(I)=1.0
        R(I,I)=V(I)*X(I)
   11   RETURN
C
C       D) INITIALISATION  OF REDUCED  SYSTEM  VARIABLES
C
   14   DO  15  I=1,MR
        DO  15  J=1,MR
        DO  15  IO=1,2
        WR(IO,I,J)=0.0
   15   ER(IO,I,J)=0.0
```

```
      DO  16  I=1,MR
      K=IR(I)
      UR(I)=U(K)
      VR(I)=V(K)
      XR(I)=X(K)
      DO 18  J=1,MR
      L=IR(J)
      DO  18  IO=1,2
      WR(IO,I,J)=W(IO,K,L)
   18 ER(IO,I,J)=E(IO,K,L)
   16 CONTINUE
C
C     CALCULATION  OF  THERMODYNAMIC  MAGNITUDES
C
C     A)  CELL  FRACTIONS  AT  POINT T,XR
C
      CALL  RIJ  (MR,UR,VR,WR,ER,TT,XR,1,PREC,SNV,SOK,RR,IMP)
      IF   (SNV)  RETURN
      DO   20  I=1,MR
      K=IR(I)
      DO   20  J=I,MR
      L=IR(J)
      R(K,L)=RR(I,J)
   20 R(L,K)=R(K,L)
C
C     B)-  CALCULATION  OF  EXCESS MIXING FREE ENTHALPY
C
      CALL  GFROH (MR,UR,VR,WR,ER,TT,XR,RR,GM,GE,IMP)
      GO TO  (11,25,30,25),INDEX
C
C      D)-  CALCULATION   OF  MIXNG  ENTHALPY  AND  EXCESS
      ENTROPY
C
   25 TM=TT-10
      TP=TT+10
      DO  26  I=1,MR
      DO  26  J=1,MR
      RM(I,J)=RR(I,J)
   26 RP(I,J)=RR(I,J)
      CALL  RIJ  (MR,UR,VR,WR,ER,TM,XR,2,PREC,SNV,SOKP,RM,IMP)
      IF  (SNV)  RETURN
      SOK=SOK  .AND.  SOKP
      CALL  RIJ  (MR,UR,VR,WR,ER,TP,XR,2,PREC,SNV,SOKP,RP,IMP)
      IF  (SNV)  RETURN
      SOK=SOK  .AND.  SOKP
      CALL  GFROH  (MR,UR,VR,WR,ER,TM,XR,RM,GMM,GEM,IMP)
      CALL  GFROH  (MR,UR,VR,WR,ER,TP,XR,RP,GMP,GEP,IMP)
      SE=(GEM-GEP)/20
      HM=GE+TT*SE
      GO  TO  (11,11,30,30)  INDEX
C
C     E)-  CALCULATION  OF  ACTIVITY  OF  COMPONENT
```

```
C
   30    DO  31  ID=2,MR
         Z=AMIN1(.01,XR(1),(1-XR(1)),XR(ID),(1-XR(ID)))/10
         DO  32  I=1,MR
         XM(I)=XR(I)
   32    XP(I)=XR(I)
         XM(ID)=XM(ID)-Z
         XM(1)=XM(1)+Z
         XP(ID)=XP(ID)+Z
         XP(1)=XP(1)-Z
         CALL  RIJ  (MR,UR,VR,WR,ER,TT,XM,2,PREC,SNV,SOKP,RM,IMP)
         IF  (SNV)  RETURN
         SOK=SOK  .AND.  SOKP
         CALL  RIJ  (MR,UR,VR,WR,ER,TT,XP,2,PREC,SNV,SOKP,RP,IMP)
         IF  (SNV)  RETURN
         SOK=SOK  .AND.  SOKP
         CALL  GFROH  (MR,UR,VR,WR,ER,TT,XM,RM,GMM,GEM,IMP)
         CALL  GFROH  (MR,UR,VR,WR,ER,TT,XP,RP,GMP,GEP,IMP)
         DG(ID)=(GMM-GMP)/(XM(ID)-XP(ID))
   31    CONTINUE
         K=IR(1)
         ACT(K)=GM
         DO  42  I=2,MR
         L=IR(I)
   42    ACT(K)=ACT(K)-X(L)*DG(I)
         DO  43  I=2,MR
         L=IR(I)
   43    ACT(L)=ACT(K)+DG(I)
         DO  44  I=1,MR
         K=IR(I)
         ACT(K)=EXP(ACT(K)/1.987/TT)
   44    IF  (ACT(K) .GE. 1)  ACT(K)=1
         RETURN
         END
C        END  CTHMKF
C
C
C
C
C
C
      SUBROUTINE  GFROH  (M,U,V,W,E,TT,X,R,GM,GE,IMP)
           DIMENSION
U(3),V(3),W(2,3,3),E(2,3,3),X(3),R(3,3),D0(3),D1(3),
     *              D2(3),RS(3,3)
C
C     I)-  CALCULATION OF  DIVERSE  PARAMETERS
C
         WRITE(IMP,*)'BEGINNING  OF  GFROH'
      DO  50  I=1,M
      D0(I)=0.0
      DO  50  J=I,M
   50    D0(I)=D0(I)+V(J)*X(J)
```

```
      DO  51  I=1,M-1
      D1(I)=D0(I)*ALOG(D0(I)/V(I)/X(I))
   51    D2(I)=D0(I+1)*ALOG(D0(I+1)/V(I)/X(I))
      DO  52  I=1,M
      DO  52  J=1,M
   52    RS(I,J)=V(I)*X(I)*V(J)*X(J)/D0(1)
C
C     II)-  CALCULATION  OF SYSTEM  DEGENERATION
C
C     A)-    CALCULATION    OF    LN(P)    (LOGARITHM    OF  TOTAL
PERMUTATION
C          NUMBER  OF  METALLIC  ATOMS
C
      PLN=0.0
      DO  60  I=1,M-1
   60    PLN=PLN+U(I)*(D1(I)-D2(I))/V(I)
C
C     B)- CALCULATION  OF  LN(U/U*)  (LOGARITHM  OF DISTINCT
C         PERMUTATION  NUMBER  BETWEEN  CELLS
C
      UUSLN=0.0
      DO  65  I=1,M
      DO  65  J=1,M
   65    UUSLN=UUSLN+RS(I,J)*ALOG(RS(I,J))-R(I,J)*ALOG(R(I,J))
C
C     C)- CALCULATION  OF  LOGARITHM  OF  DEGENERECY
C
      GLN=PLN+UUSLN
C     III)-  CALCULATION  OF  TOTAL  SYSTEM  ENERGY
C
C     A)- CELLS  FORMATION  ENERGY
C
      EF=0.0
      DO  70  I=1,M-1
      DO  70  J=I+1,M
   70    EF=EF+2.0*R(I,J)*(W(1,I,J)+X(I)*W(2,I,J))
C
C     B)- CELLS  INTERACTION  ENERGY
C
      EI=0.0
      DO  75 I=1,M-1
      S=0.0
      DO  76 J=I+1,M
   76    S=S+V(J)*X(J)*(E(1,I,J)+X(I)*E(2,I,J))
   75    EI=EI+2.0*R(I,I)*S/D0(1)
C
C     TOTAL  ENERGY
C
      ES=EF+EI
C
C     IV)-  CALCULATION  OF  FREE  ENTHALPY
C
```

```
      GM=ES-1.987*TT*GLN
C
C     V)-  CALCULATION  OF  EXCESS  FREE  ENERGY
C
      GE=GM
      DO  80  I=1,M
   80    GE=GE-1.987*TT*X(I)*ALOG(X(I))
      RETURN
      END
C     END  GFROH
C
C
C
C
C
C ***********************
C   CALCULATION  OF  CELL  FRACTIONS
C***********************
      SUBROUTINE  RIJ  (M,U,V,W,E,TT,X,IND,PREC,SNV,SOK,R,IMP)
      DIMENSION
U(3),V(3),W(2,3,3),E(2,3,3),X(3),R(3,3),P(3,3),Y(3),
     *            PZ(3,3),A(3,3),AI(3,3),B(3),DY(3),D2Y(3),Q(3)
      LOGICAL    SNV,SOK
C
C     INITIALISATION  OF  P  AND  Y  IN  RIJ
C
        WRITE(IMP,*)'BEGINNING  OF  RIJ'
      D=V(M)*X(M)
      P(M,M)=1
      Q(M)=0
      DO 50  I=1,M-1
      D=D+V(I)*X(I)
      P(I,I)=1
      Q(I)=0
      DO  51  J=I+1,M
   51     Q(I)=Q(I)+V(J)*X(J)*(E(1,I,J)+X(I)*E(2,I,J))
   50     CONTINUE
      DO 52  I=1,M-1
      DO 52  J=I+1,M
      P(I,J)=EXP((-W(1,I,J)-X(I)*W(2,I,J)+(Q(I)+Q(J))/D)/1.987/TT)

   52     P(J,I)=P(I,J)
      GO  TO  (1,2),IND
    1   DO  3  I=1,M
    3   Y(I)=V(I)*X(I)/SQRT(D)
      Z=0
      GO  TO  5
    2     DO  4  I=1,M
    4   Y(I)=SQRT(R(I,I))
      GO  TO  20
C*** CALCULATION  OF  Y   BY  DEVELOPMENT  LIMITS
C
```

```
C  1)_  CALCULATION  OF  MATRIX  PZ
C
C
     5   DO  6  I=1,M
         DO  6  J=1,M
     6   PZ(I,J)=P(I,J)**Z
C
C  2)-  CALCULATION  OF  MATRIX  A
C
         DO  7  I=1,M
         A(I,I)=2*Y(I)
         DO  7  J=1,M
         IF  (I-J)  8,7,8
     8   A(I,J)=PZ(I,J)*Y(I)
         A(I,I)=A(I,I)+PZ(I,J)*Y(J)
     7     CONTINUE
C
C  3)-  INVERSION  OF  MATRIX  A
C
         CALL  GAUINV  (M,A,SNV,AI)
         IF  (SNV)  RETURN
C
C  4)-  CALCULATION  OF  DY
C
         DO  10  I=1,M
         B(I)=0
         DO  10  J=1,M
    10   B(I)=B(I)-PZ(I,J)*ALOG(P(I,J))*Y(I)*Y(J)
         DO  11  I=1,M
         DY(I)=0
         DO  11  J=1,M
    11   DY(I)=DY(I)+AI(I,J)*B(J)
C
C
C  5)-  CALCULATION  OF  D2Y
C
         DO  12  I=1,M
         B(I)=0
         DO  12  J=1,M
    12
B(I)=B(I)-PZ(I,J)*(2*DY(I)*DY(J)+2*ALOG(P(I,J))*(Y(I)*DY(J)+
     *        Y(J)*DY(I))+Y(I)*Y(J)*ALOG(P(I,J))**2)
         DO  13  I=1,M
         D2Y(I)=0
         DO  13  J=1,M
    13   D2Y(I)=D2Y(I)+AI(I,J)*B(J)

C
C  6)-  CALCULATION  OF  Z  AND  Y  NEW  VALUE
C
         DZ=0.5
         DO  15  I=1,M
```

```
      IF  (DY(I))  16,17,16
   16   DZ=AMIN1(DZ,ABS(.1*Y(I)/DY(I)))
   17   IF  (D2Y(I))  18,15,18
   18   DZ=AMIN1(DZ,SQRT(ABS(.05*Y(I)/D2Y(I))))
   15   CONTINUE
      DZ=AMAX1(DZ,.01)
      DZ=AMIN1(DZ,(1-Z))
      Z=Z+DZ
      DO  19  I=1,M
   19   Y(I)=Y(I)+DY(I)*DZ+D2Y(I)*DZ*DZ/2
      IF (Z-1)  5,20,20
C
C***      VALUES  IMPROVEMENT  OF  Y  BY  ITERATION
C
   20   NITER=0
C
C  1)-  CALCULATIPON  OF  MATRIX  A
C
   30   DO  21  I=1,M
      A(I,I)=2*Y(I)
      DO  21  J=1,M
      IF (I-J)  22,21,22
   22   A(I,J)=P(I,J)*Y(I)
      A(I,I)=A(I,I)+P(I,J)*Y(J)
   21   CONTINUE
C
C  2)-  INVERSION  OF  MATRIX  A
C
      CALL  GAUINV   (M,A,SNV,AI)
      IF  (SNV)  RETURN
C
C  3)-  CALCULATION  OF  DY
C
      DO  23  I=1,M
      B(I)=V(I)*X(I)
      DO  23  J=1,M
   23   B(I)=B(I)-P(I,J)*Y(I)*Y(J)
      DO  34  I=1,M
      DY(I)=0
      DO  24  J=1,M
   24   DY(I)=DY(I)+AI(I,J)*B(J)
   34     CONTINUE
        SOK=.TRUE.
      DO  25  I=1,M
        IF  (Y(I))  26,25,26
   26   SOK=SOK  .AND.   (ABS(DY(I)/Y(I))  .LT.  PREC)
   25   CONTINUE
      DO  27  I=1,M
   27   Y(I)=Y(I)+DY(I)
      NITER=NITER+1
      IF (SOK) GO  TO  40
      IF (NITER-10)  30,40,40
```

```
C
C*** CALCULATION  OF  CELL  FRACTIONS
   40    DO  41  I=1,M
         DO  42  J=1,M
   42    R(I,J)=P(I,J)*Y(I)*Y(J)
   41       CONTINUE
         RETURN
         END
C        END  RIJ
C
C
C
C
C
C
C*****************
C      INVERSION  OF  MATRIX  BY  GAUSS  METHOD
C*****************
C
C ========================================
C N:MATRIX ORDER
C A:MATRIX TO BE INVERSED
C ASINGL:LOGIC VARIABLE(.TRUE. WHEN A IS ASINGULAR MATRIX)
C U:INVERSE MATRIX OF A
C ============================================================
      SUBROUTINE  GAUINV  (N,A,ASINGL,U)
      DIMENSION  A(3,3),U(3,3),IL(3),JL(3)
      LOGICAL    ASINGL
C  INITIALISATION  OF  U
      DO  1  I=1,N
      DO  1  J=1,N
    1 U(I,J)=A(I,J)
      ASINGL=.FALSE.
      DO  3  L=1,N
      UMAX=0.
      IF  (ASINGL)  GO  TO  3
C  SELECTION  OF  ELEMENT
      DO  4  I=L,N
      DO  4  J=L,N
      IF  (ABS(UMAX)-ABS(U(I,J)))  5,4,4
    5 UMAX=U(I,J)
      IL(L)=I
      JL(L)=J
    4 CONTINUE
C
C  CALCULATION  OF  PARTIAL  DETERMINANT
C
      ASINGL=ABS(UMAX)  .LT.  1.0E-8
      IF  (ASINGL)  GO  TO  3
C
C  DISPLACEMENT  OF  ROWS  AND  COLUMNS
C
```

```
      I=IL(L)
      IF  (I-L)  8,10,8
    8   DO  6  J=1,N
      S=U(L,J)
      U(L,J)=U(I,J)
    6     U(I,J)=-S
   10   J=JL(L)
      IF  (J-L)  12,15,12
   12   DO  11  I=1,N
      S=U(I,L)
      U(I,L)=U(I,J)
   11   U(I,J)=-S
   15   DO  16  I=1,N
      IF  (I-L)  17,16,17
   17   U(I,L)=-U(I,L)/UMAX
   16   CONTINUE
      DO  20  I=1,N
      DO  20  J=1,N
      IF  ((I-L)*(J-L))  21,20,21
   21   U(I,J)=U(I,J)+U(I,L)*U(L,J)
   20   CONTINUE
      DO  25  J=1,N
      IF  (J-L)  26,25,26
   26   U(L,J)=U(L,J)/UMAX
   25   CONTINUE
      U(L,L)=1.0/UMAX
    3   CONTINUE
C
C  STOP  CALCULATION  WHEN  A  IS  SINGULAR
C
      IF  (ASINGL)  RETURN
C
C  ORDERING  OF  INVERSE  MATRIX
C
      DO  30  L1=1,N
      L=N-L1+1
      J=IL(L)
      IF  (J-L)  35,35,32
   32   DO  31  I=1,N
      S=U(I,L)
      U(I,L)=-U(I,J)
   31   U(I,J)=S
   35   I=JL(L)
      IF  (I-L)  30,30,37
   37   DO  36  J=1,N
      S=U(L,J)
      U(L,J)=-U(I,J)
   36   U(I,J)=S
   30   CONTINUE
      RETURN
      END
C     END  GAUINV
```

APPENDIX II

BB2 INPUT DATA

```
   10      15       0.0030     0.0005
1       1      2
 0.045     0.043     0.058      -1.17       0.0
 0.091     0.14      0.180      -0.13      -0.07
 0.056     0.080     0.107      -0.14       0.06
-1.98     -0.0975   -0.250      -0.174     -0.083
-0.003    -0.012     0.033      -0.030     -0.003
 0.0       0.051     0.110       0.070     -0.0035
 0.03      0.046     0.056      -0.133     -0.048
0.0001
0.0001
0.00001
0.00001
0.16   0.020    0.020
0.17   0.70   0.02  0.05
```

APPENDIX III

JJMN INPUT DATA

```
1           1           3           4
SIO1        SIO2        1.    2.     60.0    2280.0     1.14
ALO1        ALO2        2.    3.    102.0   26500.0    11.40
MNO1        MNO2        1.    1.     70.9   12000.0     5.61
  2000.0          0.0          -3000.0          0.0
 -4500.0          0.0          -1000.0       5200.0
 -1200.0          0.0          -3200.0          0.0
 4    0.0001
 2S3A
      2    3    0     3720.      6.30
 1S1M
      1    0    1    -6400.     -0.50
 1S2M
      1    0    2   -14650.     -3.00
 1A1M
      0    1    1   -11430.     -2.80
0
0        0.01       0          15          0.001       0
3      1823.          10.0
1       1        36.0      2.0
2       1        21.0      2.0
```